University of St Andrews

Full metadata for this thesis is available in
St Andrews Research Repository
at:
http://research-repository.st-andrews.ac.uk/

University of St Andrews

Structural Studies of Zeolites by Solid State NMR and Microcrystal X-ray Diffraction

Richard J. Darton

Thesis for PhD Degree

September 2004

Th
E732

I, Richard John Darton hereby certify that this thesis, which is approximately 40,000 words in length, has been written by me, that it is the record of work carried out by me and that it has not been submitted in any previous application for a higher degree.

date .17/11/04. ...   signature of candidate .

I was admitted as a research student in September 2001 and as a candidate for the degree of PhD in September 2002; the higher study for which this is a record was carried out in the University of St Andrews between 2001 and 2004.

date .17/11/04. ...   signature of candidate

I hereby certify that the candidate has fulfilled the conditions of the Resolution and Regulations appropriate for the degree of PhD in the University of St Andrews and that the candidate is qualified to submit this thesis in application for that degree.

date ...17/11/04...   signature of supervisor ...

In submitting this thesis to the University of St Andrews I understand that I am giving permission for it to be made available for use in accordance with the regulations of the University Library for the time being in force, subject to any copyright vested in the work not being affected thereby. I also understand that the title and abstract will be published, and that a copy of the work may be made and supplied to any *bona fide* library or research worker.

date 17/11/04 ...   signature of candidate ..

Abstract

Solid state NMR and microcrystal X-ray diffraction have been used to study the structures of both as-made and calcined zeolites. In particular, the location of the fluoride ions has been investigated in both a SFF and a STF type zeolite using solid state NMR to determine the $^{19}F/^{29}Si$ dipolar coupling. The results of the solid state NMR and microcrystal X-ray diffraction experiments, on the SFF zeolite, have been combined to provide an accurate description of the five-coordinate silicon environment.

Solid state NMR has been shown to be a very powerful technique for studying the local structure of the zeolite ferrierite. Variable temperature experiments have provided an insight in to the mechanism of the displacive phase transition in both the purely siliceous and the aluminosilicate forms of ferrierite. The results have also indicated that the low temperature phase of siliceous ferrierite is probably of lower symmetry than has previously been reported using single crystal X-ray diffraction.

A methodology for determining the structures of fluoride containing zeolites using solid state NMR is also described, along with preliminary results on a ^{15}N isotopically labelled sample of silicalite-1.

Acknowledgements

The following people have provided invaluable help and assistance throughout my PhD:

Professor Russell Morris for his supervision and guidance,

Professor Colin Fyfe, Dr Andrew Lewis and Dr Darren Brouwer for educating me in the ways of solid state NMR and making my time at UBC more enjoyable,

Dr Manfred Buck for his assistance with the non-linear optical measurements,

Dr Gary Lee and Mr Filip Wormald for teaching me solid state NMR and letting me near the spectrometer!

Dr Luis Villaescusa for 'teaching' me the black art of zeolite synthesis!

Finally, a big thank you should go to various members of the School of Chemistry especially Melanja Smith, Robert (Sir Boab) Cathcart, Marjory Parker, Jim Bews and Dr Nigel Botting who provided many opportunities to make 'gold coins' and 'slime' and avoid research!

Table of Contents

Abbreviations and Symbols

a, b, c	crystallographic unit cell dimensions
AlPO	aluminium phosphate
ASD	5-azonia-spiro[4.5]decane
B_0	externally applied static magnetic field
B_{eff}	effective magnetic field
b_{IS}	magnitude of the dipolar coupling between I and S spins
BzDABCO	N-benzyl-1,4-diazabicyclo[2.2.2]octane
BzQ	N-benzylquinuclidinium
C_2DN	ethylene diamine
CCD	charge coupled device
$Cocp_2$	dicyclopentadienylcobalt
CP	Cross Polarization
C_q	quadrupolar coupling constant
CSA	chemical shift anisotropy
d	doublet
D'	effective dipolar coupling
DABCO	1,4-diazabicyclo[2.2.2]octane
DECDMP	N,N-diethyl-2,6-dimethylpiperidinium
DFT	density functional theory
d_{hkl}	spacing between adjacent lattice places
d_{IS}	dipolar coupling between spins I and S (radians per second)
D_{IS}	dipolar coupling between spins I and S (Hz)
DMABO	1,3,3,6,6-pentamethyl-6-azabicyclo[3.2.1]octane
DMASD	dimethylazoniaspiro[4.5]decane
DSC	differential scanning calorimetry
E	applied field strength
EMCDMP	N-ethyl,N-methyl-2,6-dimethylpiperidinium
eQ	quadrupole moment
F	force
FBzQ	4-fluorobenzylquinuclidinium
FD	framework density
FID	free induction decay
F_j	structure factor
f_j	scattering factor
GaPO	gallium phosphate
g_n	powder integral of oscillations in the CP experiment at the +1 spinning sideband
h	Planck's constant
H	Hamiltonian
HAlFER	high aluminium content ferrierite
HF	hydrofluoric acid
hkl	Miller indices
I	complex number
I	unobserved spins
I_0	scaling factor in CP curves
I_{hkl}	intensity of reflection hkl
INADEQUATE	Incredible Natural Abundance Double Quantum Transfer
J	scalar coupling
k	Boltzmann constant

k_I, k_S	rate constant for spin-lock relaxation for the I and S spins
k_{IS}	cross polarization rate constant
KTP	potassium titanyl phosphate
LAlFER	low aluminium content ferrierite sample
m	magnetic quantum number
m	multiplet
M	magnetisation
m, o, p	meta, ortho, para
M_0	initial magnetisation in relaxation time experiments
MAlFER	medium aluminium content ferrierite sample
MAS	magic angle spinning
MeOBzQ	4-methoxybenzylquinuclidinium
mmol	millimoles
mol	moles
MR	membered ring
MTBE	methyl t-butyl ether
M_{xy}	magnetisation in spin echo experiments for measuring T_2
M_z	magnetisation in saturation recovery experiments for measuring T_1
n	spinning sideband number (n = ±1, ±2...)
NLO	non-linear optics
NMR	nuclear magnetic resonance
NOBzQ	4-nitrobenzylquinuclidinium
NTE	negative thermal expansion
P	polarizability
PBU	primary building unit
PerBU	periodic building unit
ppm	parts per million
$PrNH_2$	N-propylamine
Pyr	pyridine
Q_8M_8	cubic octamer $Si_8O_{12}[OSi(CH_3)_3]$
r.f.	radio frequency
R_1	R-factor for XRD refinements
REDOR	Rotational Echo Double Resonance
r_{IS}	distance between nuclei I and S
rpm	revolutions per minute
RUM	rigid unit mode
s	singlet
S	observed spins
S/N	signal to noise ratio
S{I}	S spins observed, I spins unobserved in CP experiments
SBU	secondary building unit
SDA	structure directing agent
SEM	scanning electron microscopy
SHG	second harmonic generation
Si/Al	silicon to aluminium ratio
SiO_4 or $SiO_{4/2}$	tetrahedral silicon species
$S_{isolated}$	contribution to CP signal intensity from isolated spins
$S_{network}$	contribution to CP signal intensity from extended spin network
T	temperature
t	triplet
t	time
T_1	spin-lattice relaxation time constant
$T_{1\rho}$	spin-lattice relaxation time constant in the rotating frame

T_2	spin-spin relaxation time constant
tBTMA	tert-butyltrimethylammonium
TEDOR	Transferred Echo Double Resonance
TEOS	tetraethylorthosilicate
TEM	transmission electron microscopy
TMS	tetramethylsilane
tPABr	tetrapropylammonium bromide
U	isotropic displacement parameter
V	volume
w_{hkl}	weighting value for reflection hkl
wR_2	weighted R-factor
XRD	X-ray diffraction
θ_m	magic angle (54.74°)
γ	magnetogyric ratio
η	asymmetry parameter of the CSA tensor
λ	frequency
τ	delay time
Ω	span of the CSA tensor
χ	dielectric susceptibility
α	Si-O-Si bond angle
α, β, γ	crystallographic unit cell angles
$\varphi_{(hkl)}$	structure factor phase
ω, ω_0	frequency
δ'_{aniso}	effective anisotropy parameter of the CSA tensor
ω_0	Larmor frequency in rads^{-1}
ν_0	Larmor frequency in Hz
μ_0	permittivity of free space
$\delta_{11}, \delta_{22}, \delta_{33}$	principal elements of the chemical shift anisotropy tensor
δ_{aniso}	anisotropy parameter of the CSA tensor
ΔE_z	Zeeman energy difference
δ_{Iso}	isotropic chemical shift
ΔJ	anisotropy in the scalar coupling
ω_R	spin rate
$[SiO_{4/2}F]^-$	five coordinate silicon species
$\|F_{(hkl)}\|$	structure factor amplitude

The following colour scheme is generally used for the figures throughout this thesis, unless otherwise stated:

Grey or orange	Si atoms
Purple	Al atoms
Red	O atoms
Green	F atoms / ions
Grey	C atoms
Blue	N atoms / ions
Yellow	H atoms

1.0 Introduction

1.1 Background and Structure

Zeolites are microporous aluminosilicate minerals, which were first discovered by the Swedish mineralogist Baron Axel Cronstedt in 1756.[1] The name zeolite comes from the Greek words *zeo* meaning boil and *lithos* meaning stone and describes the effect seen on heating a hydrated zeolite sample. Over 50 natural zeolites are now known, and this includes minerals that are the main constituents of the semi-precious stone Lapis Lazuli. Most natural zeolite samples are found in igneous basalts and sedimentary tufts and are thought to have been formed at high temperatures and pressures and to have crystallised over many thousands of years.

Zeolites are constructed of both SiO_4 and $[AlO_4]^-$ tetrahedra, which connect through the corner sharing of oxygen atoms to give a regular 3-dimensional crystalline framework containing channels and pores. These channels and pores are usually between 3 and 15 Å in diameter and can be filled with water or other guest molecules.[2] The entrances to these channels are via windows, which are of varying sizes depending on the number of tetrahedral atoms that are linked together. The sizes of the windows are usually expressed by the number of tetrahedral atoms within the ring; for example, 10 MR describes a 10 membered ring or window.[3] The general composition of a zeolite can be expressed as $M_x(Si_{1-x}+Al_x)O_2.zH_2O$, where M is either a mono- or divalent cation and z is the quantity of occluded water. The presence of the cations, which are usually Na^+, Ca^{2+} or Mg^{2+}, is to balance the charge on the framework caused by the negative charge on the $[AlO_4]^-$ tetrahedra.
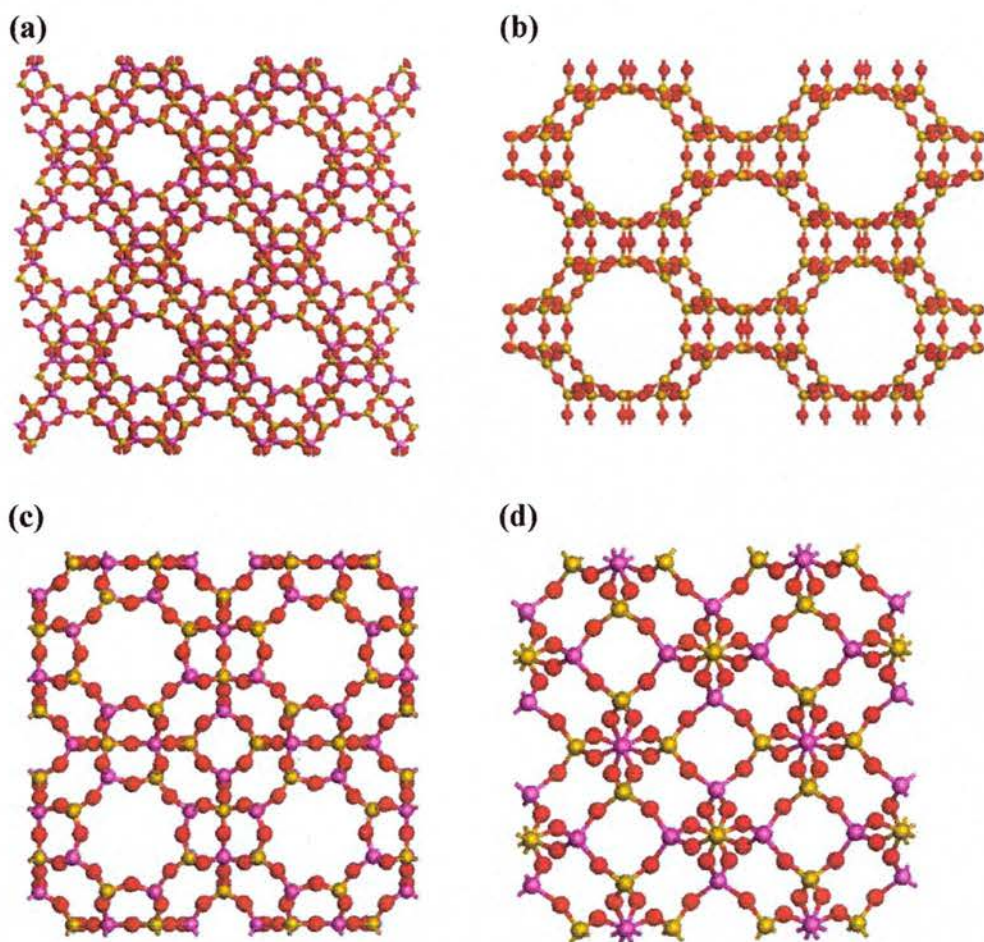
Figure 1.1 Zeolite structures: **(a)** Faujasite; **(b)** ITQ-4; **(c)** Zeolite A; **(d)** Sodalite.

Work to try and synthesise analogues of natural zeolites can be traced back to 1845, but the first successes did not occur until the 1940s when X-ray diffraction became available for routine product identification.[1] Much of this successful work was carried out by a team at Union Carbide led by R. M. Milton,[4] who by the end of 1949 had made synthetic equivalents of gismondite and sodalite. The first purely synthetic zeolite was synthesised in 1948 by Barrer,[5-7] but it was work by the Union Carbide group that produced one of the most well known synthetic zeolites, zeolite A (Figure 1.1 c).[8]

The term zeolite has now come to embrace far more than just the original aluminosilicates and now describes many microporous materials including aluminium phosphates (AlPOs),[9,10] gallium phosphates (GaPOs),[11,12] pure silica zeolites[13,14] and clathrasils.[15-17] Clathrasils are framework based materials, like zeolites, but they lack the channels and the large accessible void spaces that are characteristic of the traditional zeolites. There are now more than 150 known zeolite framework types, with many microporous materials sharing the same structure but with different chemical compositions. These frameworks are all classified by the International Zeolite Association (IZA) and are designated three letter codes such as LTA and SOD for zeolite A and sodalite type frameworks respectively.[18,19] The three letter codes only describe the framework type and do not give any information on the chemical composition of the material.

The framework of zeolites can be thought of as being made up of specific building blocks called secondary building units (SBUs). These SBUs (Figure 1.2) exist in arrays of either chain or layer like frameworks with up to an infinite number of units. Each particular zeolitic framework type is made up of at least one specific type of SBU, which itself can contain up to 16 tetrahedral atoms or primary building units (PBUs). At present, there are 20 defined SBUs, but still more could be observed as new zeolite structures are discovered. It is these well defined architectures that give zeolites their highly valued properties and therefore the more that is known about the structures the better the understanding of current and future applications.
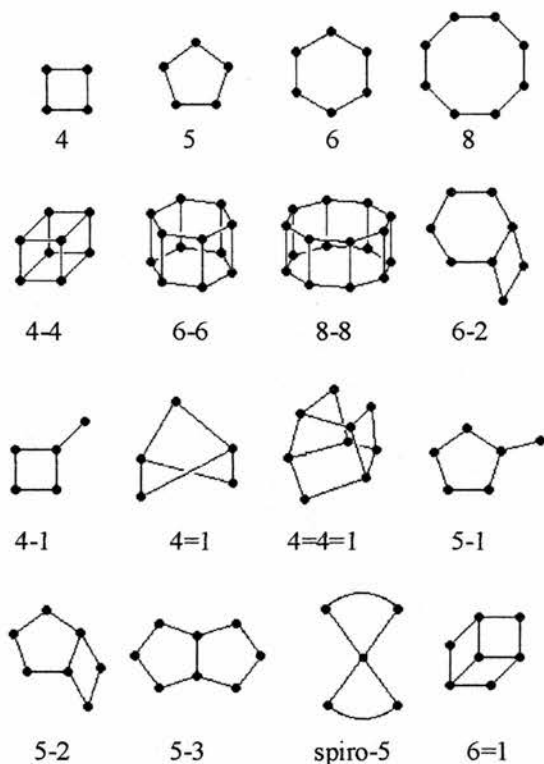
Figure 1.2 16 of the most common zeolite secondary building units (SBUs)

Zeolites are now not thought to be just restricted to Earth. Recent infrared experiments have shown that feldspars and their hydrated counterparts, zeolites, could be present on the surface of Mars.[20] It is also possible that the different atmospheric and geological conditions on Mars will have produced new framework types that cannot be synthesised easily on Earth.

1.2 Synthesis and Characterisation of Zeolites

1.2.1 Background to Synthesis

The early zeolite syntheses centred on mimicking the geological conditions that form natural minerals, which involved high pressures (>100 bar) and temperatures (>200 °C). It was not until the late 1940s that Milton's group developed the hydrothermal zeolite synthesis method using reactive alkali-metal aluminosilicate gels at temperatures around 100 °C and at autogenous pressures.[4]

In 1961, a zeolite synthesis using tetramethylammonium cations was reported by Barrer and Denny.[21,22] They had noticed that the addition of alkyl ammonium ions to a sodium aluminosilicate gel increased the Si/Al ratio for zeolites consisting of sodalite cages. Since then many zeolites have been synthesised using organic additives, especially quartenary ammonium ions, which are often referred to as structure directing agents (SDAs) or templates. Many of today's zeolites are prepared using a hydrothermal technique. This involves heating a solution or gel in a Teflon-lined stainless steel autoclave at temperatures of between 90 and 200 °C for a period of a few hours up to several weeks. The synthesis gels mainly consist of water, a source of aluminium and / or silicon, a mineralising agent and a SDA but they can also contain other metals and organic solvents.

1.2.2 Role of the Organic Species During Synthesis

Initial investigations in to the role of the organic molecules during zeolite syntheses showed that they were not simply acting as charge balancing cations. Instead it was suggested that the organic molecules were acting to direct the synthesis in some way, due to close correlation seen between the size of the zeolite pores and the shape and dimensions of the organic templates. This process is demonstrated well in the synthesis of sodalite using tetramethylammonium cations, were in the final product the cations are located in the centre of the sodalite cages and are too big to enter or leave. This case, along with other examples, led to the theory that the organic molecules were acting as templates for the aluminosilicate framework to build around and therefore leading to specific structures. This theory cannot be applied to most zeolites, such as ZSM-5 for which tetrapropylammonium cations are often used in the synthesis.[23-25] These tPA$^+$ cations are located at the intersection of two channels in the ZSM-5 structure from which they cannot enter or leave. The ZSM-5 zeolite can however be successfully synthesised in the absence of any organic species showing that the structures can still be prepared without the need of templates. There are also many examples of the same organic species being used to synthesise several different zeolites and this has led to the proposal that the organic molecules have some form of structure directing role. Davis and Lobo have suggested that the organic molecules used in zeolite syntheses may in fact act in three different ways: (1) as structure directing agents, (2) as templates and (3) as space filling species.[26]

The role of the structure directing agent is to help to produce a preferential structure, although the final material made is often dependent on other factors such as electrostatic interactions or the effect of the organic species on the pH of the reaction

mixture. Figure 1.3 shows a proposed mechanism of structure direction and crystal growth of [TPA]-ZSM-5 by Burkett and Davis,[27] where interactions can be seen between the tPA$^+$ cations and the silicate species.
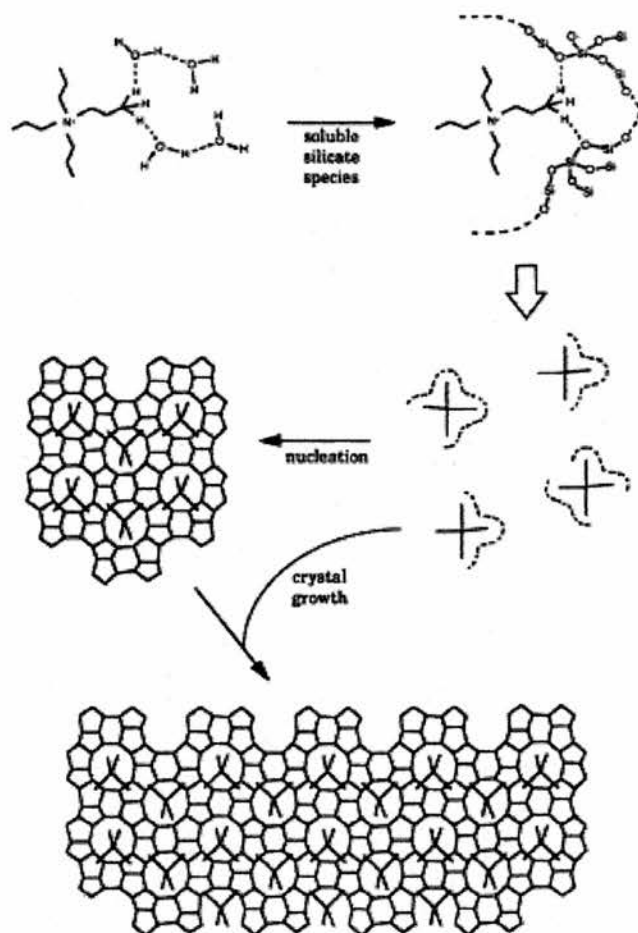
Figure 1.3 Schematic diagram of the proposed mechanism for the formation of [tPA]-ZSM-5 by Burkett and Davis, redrawn from ref. 27.

The role of a template is to form a unique structure that reflects the electronic and geometrical features of the template. The final way that the organic molecules can influence the zeolite formed is to act as space filling agents within the zeolite pores, which has the effect of reducing the water that is trapped within the framework. This

is thought to reduce the unfavourable energetic interactions between the water molecules and the growing zeolite framework.

Zones and co-workers have shown that the C/N^+ ratio of the organic molecules is a critical parameter for the synthesis of high silica zeolites when using hydroxide ions as a mineraliser.[28] SDA cations with C/N^+ ratio of between 11 and 15 work very well for the synthesis of high silica zeolites and may explain why small cations like tetramethylammonium cannot easily be used to synthesise high silica phases in hydroxide media.

The exact role of the organic molecules within zeolite syntheses is still not completely understood and more work will be needed if the question of the role of the organics is to be finally answered. However, to do this will require a more in-depth structural investigation of zeolite frameworks and in particular the location of the organic molecules within the pores.

1.2.3 Role of the Mineralising Agent

The role of the mineralising agent in its simplest form is to get the sparingly soluble silica and alumina species in to solution. Up until the late 1970s, the only species used as a mineralising agent was hydroxide ions, which meant that all syntheses were carried out at high pHs usually of between 10 and 12. In 1976 Flanigen and Patton introduced the use of fluoride ions as a mineralising agents,[29] which enabled zeolites to be synthesised at low or neutral pHs. It waswas not until the late 1980s, however, that fluoride ions began to be widely experimented with for the synthesis of zeolites and in particular for the production of high silica zeolites.[30] The use of fluoride ions has enabled many new phases to be synthesised including several

that do not crystallise if hydroxide ions are used as the mineralising agent.[31,32] The major advantage of using the fluoride method for the synthesis of high silica zeolites is that larger crystals[33] can be produced, which have less defects[34,35] and often lower densities[31] than if the hydroxide method had been used. When high silica zeolites are synthesised using the hydroxide method lots of defects occur in the framework in the form of Si-O⁻,[36] which is needed to balance the charge on the organic cations (Figure1.4). These defects do not occur as often in high silica phases produced by the fluoride route as the incorporated fluoride anions balance the charge on the organic cations.[32,37,37]
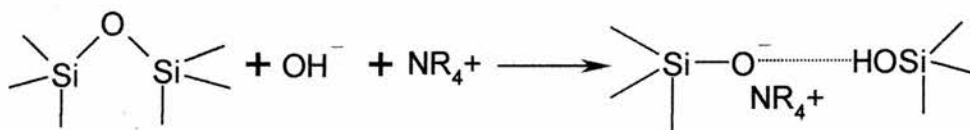
Figure 1.4 Structural integration of OH⁻ ions in framework defect sites, redrawn from ref 41.

Therefore, most of the high and pure silica phases are synthesised using fluoride ions as a mineraliser, whereas the aluminosilicate zeolites are often prepared in hydroxide media. The use of fluoride ions has not just been restricted to the synthesis of zeolites. Many other zeolite related materials have also been prepared by the fluoride route, including aluminium[38] and gallium phosphates[12,39,40] although these will not be discussed in this thesis.

1.2.4 Further Roles of the Fluoride Ions

The role of the fluoride ion as a mineralising agent, where it acts to get silica species in to solution, has just been described. It has been suggested by Camblor *et al.*[32,37] that the fluoride ions also have another role in the synthesis of pure silica zeolites. This is to act as a catalyst for the condensation reaction, for the production of Si-O-Si bonds. This catalytic process is shown in Figure 1.5 and involves the formation of a 5-coordinate silicon species ($[SiO_{4/2}F]^-$).[41,42] This penta coordinated silica undergoes a nucleophilic attack on a neighbouring 5-coordinate silica species and culminates in the loss of water and the formation of a new Si-O-Si bond.
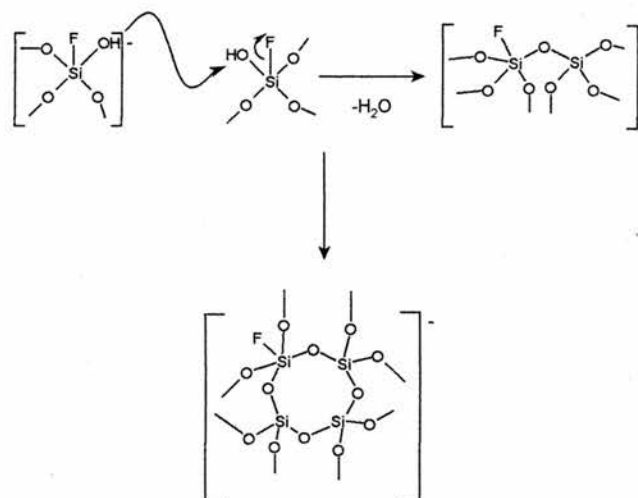
Figure 1.5 Fluoride ion catalysed condensation reaction for the formation of new Si-O-Si bonds.

Solid state NMR[41-44] and X-ray diffraction[3,45-47] studies of fluoride containing pure silica zeolites have shown that the fluoride ions can be covalently incorporated in to the zeolite framework, usually in small four membered ring cages. The pure silica clathrasil, octadecasil, has fluoride ions centred in double four ring cages and it is

thought that the fluoride ion stabilises this cage and may even have a structure directing effect.[17]

In addition, the fluoride ions have been shown to interact with the positive charge on the SDAs causing the organic molecules to align within the zeolite ITQ-4.[47,48] The structure of ITQ-4 is characterised by an undulating one-dimensional 12 membered ring pore system. Morris *et al.* have shown that the fluoride ions, in the as-synthesised sample, are present as part of a penta-coordinate species $[SiO_{4/2}F]^-$ in one of two possible $[4^3 5^2 6^1]$ cages. The fluoride ions, however, were found to be disordered over two possible sites within the cages they occupy.[47] The presence of these fluoride ions in specific cages causes the template molecules to align head to tail (noncentrosymmetrically) and show long range order within the zeolite pores, even though the zeolite framework is centrosymmetric (Figure 1.6a). This is thought to be due to the negative charge on the fluoride anion electrostatically attracting the positive charge on the asymmetric quinuclidinium derivative. Two potential reasons for the fluoride ions being in only every other cage have been proposed by Morris *et al.* The first is purely electrostatic, it is thought that the negative charge on the fluoride ions would force them to be as far apart as possible. The second reason is due to the strain put on the four membered rings between the two adjacent six membered rings by the presence of one fluoride ion (Figure 1.6b). The presence of fluoride ions in all of the six membered rings would put too much strain on the four membered rings and would make the structure unstable.[47]

(a)   (b)
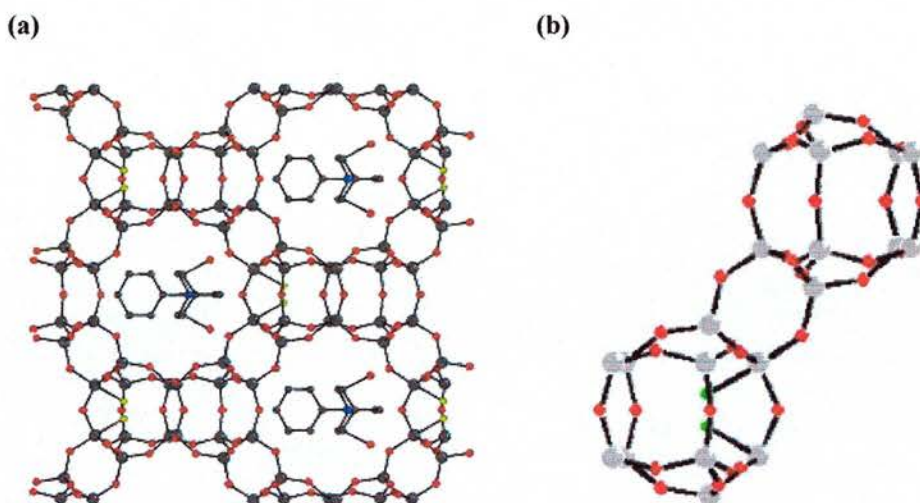
Figure 1.6 (a) Structure of ITQ-4 showing noncentrosymmetric alignment of template molecules, (b) $[4^3 5^2 6^1]$ cage of ITQ-4 showing the two potential fluoride locations.

Chapters 4 and 5 describe more about the location of the fluoride ions within pure silica zeolites and their effects on template ordering within other pure and high silica zeolites.

1.2.5 Characterisation

Many analytical techniques have been used to study zeolites over the past 50 years, yet still the main method of characterisation involves diffraction. There are many different diffraction techniques now available, but still the most widely used for zeolite characterisation is powder X-ray diffraction (XRD). Powder XRD enables a zeolite sample to be quickly identified as a specific framework type[19,49] and has been used on many occasions to solve whole structures.[13,50,51] More recently single crystal X-ray diffraction and in particularly microcrystal XRD[3,47] have been applied to pure silica zeolites and this work is described in Chapter 1.5.

Among the other techniques that have been used in zeolite characterisation are neutron diffraction on powders and single crystals,[52] infrared spectroscopy.[53] and computer modelling.[54] Computer modelling has been used extensively to help solve structures using powder diffraction data as well as to suggest synthesis mechanisms and to predict new zeolitic structures.

The use of solid state NMR in the characterisation of zeolites is well known, however, much of this work has been used to 'backup' results from other techniques. More recently solid state NMR has started to be used as a main characterisation technique, quite often along with diffraction experiments, to gain more information about the structures of these materials.[44,45,55] Chapter 1.4 discusses the role of solid state NMR in zeolite chemistry and Chapters 5 and 6 show that MAS NMR and X-ray diffraction can be highly complementary techniques for the structural study of zeolites. Another characterisation technique widely employed for the study of zeolites is electron microscopy that can probe crystal surfaces at almost atomic resolution and show the presence of faults and defects within the structure.[56,57]

Many of the techniques mentioned give valuable information on the framework structure, but it is often the void space within the zeolite that enables them to be applied to such a variety of applications. This void space is measured by the absorption of gases in to the zeolite and can give information on how much gas and which particular gases can be stored within the zeolite framework.

1.3 Applications of Zeolites

The well-defined and highly specific structures of zeolites lead to them having some very useful and interesting properties and therefore applications. There are three

main uses of zeolites, these being for catalysis, separation and ion exchange. Acid exchanged zeolites are now probably the most important heterogeneous acid catalysts in industry with the majority of the world's petroleum being produced by fluidised catalytic cracking using a faujasite type zeolite catalyst.[58,59] The most important part of a zeolite in terms of catalysis is the number of accessible Brönsted acid sites.[60] These acid sites are linked to the number of aluminium atoms in the framework and are often referred to as defects. The ability to synthesise aluminosilicate zeolites to an exact repeatable formula boosted the use of them in industrial catalytic processes, as natural versions were often unreliable. One of the most well known synthetic zeolites used in heterogeneous catalysis is ZSM-5,[61] which is used in the synthesis of ethylbenzene, the isomerisation of xylenes and the disproportionation of toluene. The role of ZSM-5 in the isomerisation of xylenes as a shape selective catalyst is depicted in Figure 1.7. A mixture of meta, ortho and para xylene are passed over the ZSM-5 catalyst, which has a well defined pore size that is only large enough to allow the p-xylene to pass through. This leads to p-xylene being the main product with only smaller amounts of the m- and o- xylenes.
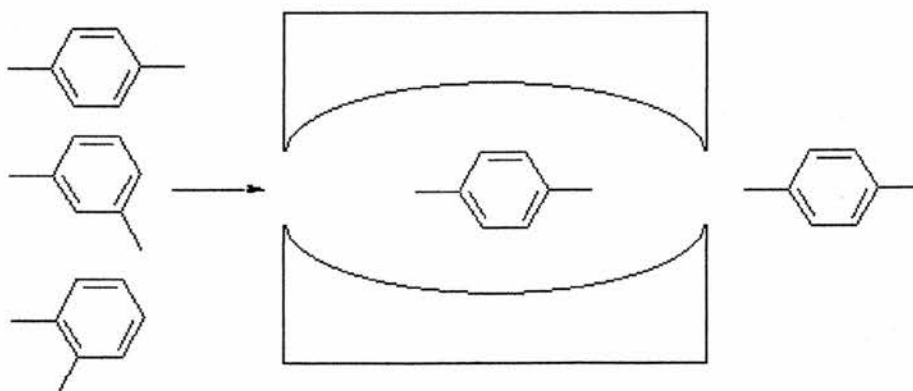
Figure 1.7 Shape selective catalysis of xylenes by the zeolite catalyst ZSM-5

Zeolites are also used as ion exchangers due to them having negatively charged porous frameworks in which cations are able to sit.[62] This property is extensively used in washing powders where the zeolite role is to mop up Ca^{2+} and Mg^{2+} ions in exchange for Na^+ ions and hence soften the water to enable a lather to be produced. The ability to synthesise zeolites with different pore sizes has enabled the selective removal of larger radioactive cations from aqueous nuclear waste and spills.[63-66]

The specific pore sizes of zeolites are also why they are extensively used for separations of gasses. The separation relies on only certain sizes of molecules being able to pass through the zeolite pores. This can be used either for the removal of specific molecules such as organics from an air supply or for the selective increase of one particular gas such as oxygen.[67]

The use of zeolites as catalytic and sorptive materials is well known, however these types of materials can also show excellent optical properties.[68] This is due to the well-defined pore structure of microporous materials that can be occupied by optically active organic molecules or ions. The main advantage of using microporous materials is that good optically active organic molecules can be incorporated into a thermally robust inorganic framework and therefore bringing together the best properties of both materials. Bull *et al.* have already shown that the alignment of the template molecules in ITQ-4 gives rise to second harmonic generation;[48] as does the incorporation of guest molecules in to the pores.[68-71] Hence, it is believed that zeolites and related materials will be increasingly used as optical materials in the future.

More recently many new zeolite applications have been found; and these have included uses as diverse as contrast agents for magnetic resonance imaging (MRI) scans[72,73], nanoscale electronic devices[74] and zeolite-dye microlasers,[75] as well as for

growing plants on the Russian Space Station, Mir, using zeoponics.[76-78] There are of course many other uses for zeolites and their related materials, several of which are reviewed in an excellent paper by F. A. Mumpton.[79]

It is the well-defined structure of pores and channels in microporous materials like zeolites that has enabled them to be applied to such a variety of applications. However, if new applications are to be found or existing ones improved this will require a more extensive knowledge of zeolite structures and the interaction of guest species with the frameworks.

1.4 Solid State NMR of Zeolites

The use of solid state NMR for the study of zeolites grew rapidly with the advent of high resolution techniques such as magic angle spinning (MAS) and cross polarization (CP).[80] These enabled the individual resonances corresponding to specific tetrahedral sites to be examined due to a large increase in spectral resolution.[81-83] This ability to resolve individual resonances in a spectrum led to a vast increase in the information that could be gained about zeolitic frameworks, especially for high and pure silica zeolites. Much of this initial work was dominated by the nuclei ^{29}Si and ^{27}Al but nearly all the nuclei found in zeolites and their related materials are NMR active and have since been investigated.[84] These include ^{15}N, ^{17}O, ^{19}F, ^{23}Na, ^{31}P, ^{45}Sc, and ^{71}Ga as well as numerous other nuclei that are present as guest molecules absorbed in to zeolite channels. Numerous solid state NMR experiments have been applied to zeolites for studying their frameworks, host-guest interactions, their synthesis and crystallisation. Examples of these include ^{29}Si Incredible Natural Abundance Double Quantum Transfer (INADEQUATE) experiments for studying Si-

O-Si framework connectivities.[85] ^{1}H-^{13}C-^{29}Si Transferred-Echo Double Resonance
(TEDOR) experiments for studying the interaction between organic guest molecules
and the framework[86] and, Multiple Quantum Magic Angle Spinning (MQMAS)
experiments on ^{23}Na to study the crystallisation of zeolites.[87] Solid state NMR has
been applied in many other areas of microporous materials and these have been
discussed in many reviews and books such as those by Engelhardt and Michel,[84]
Klinoswki[88] and Fyfe *et al.*[89]

1.5 Microcrystal X-ray Diffraction of Zeolites

Microcrystal X-ray diffraction involves the use of synchrotron radiation to enable
the study of crystals that are too small for a conventional laboratory diffractometer.[90]
On average, the single crystals studied using synchrotron radiation have dimensions of
20 x 20 x 10 μm. The structures of many pure silica zeolites and related microporous
materials have been solved using microcrystal XRD.[3,31,47,48] Many of these samples
were synthesised by the fluoride route, as often only this method yields large enough
crystals. One of the earliest uses of microcrystal XRD for the study of zeolites was
for the structure solution of SSZ-23 by Morris *et al.*.[3] The determination of the
structure of this zeolite was initially attempted by synchrotron powder XRD,[91] as
crystals could not be grown large enough for conventional single crystal XRD.
However, even with the combination of synchrotron powder diffraction data and
Monte Carlo computational techniques the structure could not be solved. Morris *et al.*
successfully determined the structure of SSZ-23 and were able to show that the
framework consisted of 7-MR and 9-MR and in addition determined the location of
the SDAs. The solving of this structure and many others since then was only made

possible due to microcrystal XRD being a very powerful technique and without it, many crystal structures of zeolites and other materials would not be known.

1.6 Aims and Objectives

There are several aims to this thesis; however, the main aim is to understand more about the structure of zeolites by combining two very powerful analytical techniques, MAS NMR and microcrystal X-ray diffraction. This overall aim can be broken down in to several individual objectives:

1. Synthesis of SDA and pure and high silica zeolites – In order to carry out accurate structural investigations it is necessary to synthesise the highest quality samples of pure and high silica zeolites and the necessary structure directing agents.

2. Find other zeolites like ITQ-4 that show the property of second harmonic generation and attempt to increase the SHG signal of ITQ-4 by functionalising the organic SDA.

3. Use microcrystal X-ray diffraction and non-linear optics to study the structures of unknown as-synthesised zeolites in order to gain more information about the roles of the structure directing agents and the fluoride ions.

4. Investigate the local structure of the $[SiO_{4/2}F]^-$ units in pure silica zeolites using both microcrystal X-ray diffraction and MAS NMR.

5. Determine the structure of a known pure silica zeolite using MAS NMR of an isotopically enriched sample and show that MAS NMR could be used as a routine method for zeolite characterisation.

6. Investigate the phase transition in both calcined pure silica ferrierite and aluminosilicate ferrierite using MAS NMR.

aluminosilicate ferrierite using MAS NMR.

1.7 References for Chapter 1

1. M. L. Occelli and H. E. Robson, *Zeolite Synthesis*, American Chemical Society, Washington DC, 1989.

2. C. S. Cundy and P. A. Cox, *Chem. Rev.*, 2003, **103**, 663.

3. M. A. Camblor, M. J. Diaz-Cabanas, J. Perez-Pariente, S. J. Teat, W. Clegg, I. J. Shannon, P. Lightfoot, P. A. Wright and R. E. Morris, *Angew. Chem. Int. Ed.*, 1998, **37**, 2122.

4. R. M. Milton, *ACS Symp. Ser.*, 1989, **398**, 1.

5. R. M. Barrer, L. Hinds and E. A. White, *J. Chem. Soc.*, 1953, 1466.

6. R. M. Barrer and C. Marcilly, *J. Chem. Soc.*, 1970, 2735.

7. R. M. Barrer, *J. Chem. Soc.*, 1948, 127.

8. R. M. Milton, *US* 2,882,243, 1959.

9. S. T. Wilson, B. M. Lok and E. M. Flanigen, 4,310,440, 1982.

10. S. T. Wilson, B. M. Lok, C. A. Messina, T. R. Cannan and E. M. Flanigen, *J. Am. Chem. Soc.*, 1982, **104**, 1146.

11. S. J. Weigel, R. E. Morris, G. D. Stucky and A. K. Cheetham, *J. Mater. Chem.*, 1998, **8**, 1607.

12. D. S. Wragg and R. E. Morris, *J. Phys. Chem. Solids*, 2001, **62**, 1493.

13. P. A. Barrett, M. A. Camblor, A. Corma, R. H. Jones and L. A. Villaescusa, *Chem. Mater.*, 1997, **9**, 1713.

14. P. Wagner, Y. Nakagawa, G. S. Lee, M. E. Davis, S. Elomari, R. C. Medrud and S. I. Zones, *J. Am. Chem. Soc.*, 2000, **122**, 263.

15. J. B. Higgins, *Silica: Physical Behavior, Geochemistry and Materials Applications*, 1994, **29**, 507.

16. G. Vandegoor, C. C. Freyhardt and P. Behrens, *Zeitschrift Fur Anorganische Und Allgemeine Chemie*, 1995, **621**, 311.

17. P. Caullet, J. L. Guth, J. Hazm, J. M. Lamblin and H. Gies, *Eur. J. Solid State Inorg. Chem.*, 1991, **28**, 345.

18. W. M. Meier, D. H. Olson and C. Baerlocher, *Zeolites*, 1996, **17**, 1.

19. *International Zeolite Association* [Web Page], available at http:\\www.iza-online.org.

20. S. W. Ruff, *Icarus*, 2004, **168**, 131.

21. R. M. Barrer, P. J. Denny and E. M. Flanigen, *US* 3,306,922, 1967.

22. R. M. Barrer and P. J. Denny, *J. Chem. Soc.*, 1961, 971.

23. R. W. Grose and E. M. Flainigen, *US* 4 257 885, 1981.

24. R. W. Grose and E. M. Flanigen, *Belgium* 851,066, 1977.

25. R. W. Grose and E. M. Flanigen, *UK* 574,840, 1980.

26. R. F. Lobo, S. I. Zones and M. E. Davis, *J. Inclusion Phenom.*, 1995, **21**, 47.

27. S. L. Burkett and M. E. Davis, *Chem. Mater.*, 1995, **7**, 1453.

28. S. I. Zones, Y. Nakagawa, G. S. Lee, C. Y. Chen and L. T. Yuen, *Microporous Mater.*, 1998, **21**, 199.

29. E.M. Flanigen and R.L. Patton, *US* US 4 073 865, 1976, 1978.

30. G. A. Ozin, A. Kuperman and A. Stein, *Angew. Chem., Int. Ed. Engl.*, 1989, **28**, 359.

31. M. A. Camblor, A. Corma, P. Lightfoot, L. A. Villaescusa and P. A. Wright, *Angew. Chem., Int. Ed. Engl.*, 1997, **36**, 2659.

32. M. A. Camblor, L. A. Villaescusa and M. J. Diaz-Cabanas, *Top. Catal.*, 1999, **9**, 59.

33. A. S. Kuperman, S. Oliver, G. A. Ozin, J. M. Garces and M. M. Olken, *Nature*, 1993, **365**, 239.

34. J. M. Chezeau, L. Delmotte, J. L. Guth and Z. Gabelica, *Zeolites*, 1991, **11**, 598.

35. J. M. Chezeau, L. Delmotte, J. L. Guth and M. Soulard, *Zeolites*, 1989, **9**, 78.

36. H. Koller, R. F. Lobo, S. L. Burkett and M. E. Davis, *J. Phys. Chem.*, 1995, **99**, 12588.

37. P. A. Barrett, M. J. Diaz-Cabanas, M. A. Camblor and R. H. Jones, *J. Chem. Soc., Faraday Trans.*, 1998, **94**, 2475.

38. P. S. Wheatley and R. E. Morris, *J. Solid State Chem.*, 2002, **167**, 267.

39. A. Matijasic, B. Marler, J. C. M. Acevedo, L. Josien and J. Patarin, *Chem. Mater.*, 2003, **15**, 2614.

40. A. Matijasic, J. L. Paillaud and J. Patarin, *J. Mater. Chem.*, 2000, **10**, 1345.

41. H. Koller, A. Wolker, L. A. Villaescusa, M. J. Diaz-Cabanas, S. Valencia and M. A. Camblor, *J. Am. Chem. Soc.*, 1999, **121**, 3368.

42. H. Koller, A. Wolker, H. Eckert, C. Panz and P. Behrens, *Angew. Chem., Int. Ed. Engl.*, 1997, **36**, 2823.

43. C. A. Fyfe, D. H. Brouwer, A. R. Lewis and J. M. Chezeau, *J. Am. Chem. Soc.*, 2001, **123**, 6882.

44. C. A. Fyfe, D. H. Brouwer, A. R. Lewis, L. A. Villaescusa and R. E. Morris, *J. Am.*

Chem. Soc., 2002, **124**, 7770.

45. I. Bull, P. Lightfoot, L. A. Villaescusa, L. M. Bull, R. K. B. Gover, J. S. O. Evans and R. E. Morris, *J. Am. Chem. Soc.*, 2003, **125**, 4342.

46. L. A. Villaescusa, P. Lightfoot and R. E. Morris, *Chem. Comm.*, 2002, 2220.

47. L. A. Villaescusa, P. S. Wheatley, I. Bull, P. Lightfoot and R. E. Morris, *J. Am. Chem. Soc.*, 2001, **123**, 8797.

48. I. Bull, L. A. Villaescusa, S. J. Teat, M. A. Camblor, P. A. Wright, P. Lightfoot and R. E. Morris, *J. Am. Chem. Soc.*, 2000, **122**, 7128.

49. W. M. Meier and D. H. Olson, *Zeolites*, 1992, **12**, 1.

50. R. W. Grosse-Kunstleve, L. B. Mccusker and C. Baerlocher, *J. Appl. Crystallogr.*, 1999, **32**, 536.

51. L. B. Mccusker, C. Baerlocher, R. Grosse-Kunstleve, S. Brenner and T. Wessels, *Chimia*, 2001, **55**, 497.

52. R. E. Morris, S. J. Weigel, N. J. Henson, L. M. Bull, M. T. Janicke, B. F. Chmelka and A. K. Cheetham, *J. Am. Chem. Soc.*, 1994, **116**, 11849.

53. L. A. Villaescusa, F. M. Marquez, C. M. Zicovich-Wilson and M. A. Camblor, *J. Phys. Chem. B*, 2002, **106**, 2796.

54. D. W. Lewis, C. R. A. Catlow and J. M. Thomas, *Faraday Discuss.*, 1997, 451.

55. G. T. Kokotailo, C. A. Fyfe, Y. Feng, H. Grondey, H. Gies, B. Marler and D. E. Cox, *Stud. Surf. Sci. Catal.*, 1995, **94**, 78.

56. M. W. Anderson, T. Ohsuna, Y. Sakamoto, Z. Liu, A. Carlsson and O. Terasaki, *Chem. Comm.*, 2004, 907.

57. G. Gonzalez, W. Stracke, Z. Lopez, U. Keller, A. Ricker and R. Reichelt, *Microscopy and Microanalysis*, 2004, **10**, 224.

58. T. F. Degnan, *Top. Catal.*, 2000, **13**, 349.

59. J. Weitkamp, *Solid State Ionics*, 2000, **131**, 175.

60. Y. Yokomori, J. Wachsmuth and K. Nishi, *Microporous Mater.*, 2001, **50**, 137.

61. R. J. Argauer and G. R. Landolt, *US* 3,702,886, 1972.

62. Y. Watanabe, H. Yamada, J. Tanaka, Y. Komatsu and Y. Moriyoshi, *Sep. Sci. Technol.*, 2004, **39**, 2091.

63. B. De Gennaro, A. Colella, P. Aprea and C. Colella, *Microporous Mater.*, 2003, **61**, 159.

64. H. Faghihian, M. G. Maragheh and A. Malekpour, *J. Radioanal. Nucl. Chem.*, 2002, **254**, 545.

65. S. Kesraouiouki, C. R. Cheeseman and R. Perry, *J. Chem. Technol. Biotechnol.*, 1994, **59**, 121.

66. A. E. Turkman, F. Aslan and I. Ege, *Fresenius Environmental Bulletin*, 2004, **13**, 574.

67. M. W. Ackley, R. F. Giese and R. T. Yang, *Zeolites*, 1992, **12**, 780.

68. N. Herron, *J. Inclusion Phenom.*, 1995, **21**, 283.

69. S. D. Cox, T. E. Gier, G. D. Stucky and J. Bierlein, *J. Am. Chem. Soc.*, 1988, **110**, 2986.

70. S. D. Cox, T. E. Gier and G. D. Stucky, *Chem. Mater.*, 1990, **2**, 609.

71. K. Hoffmann, D. Prescher and F. Marlow, *Journal of Information Recording*, 1998, **24**, 191.

72. K. J. Balkus and I. Bresinska, *J. Alloys Compd.*, 1994, **207**, 25.

73. I. Bresinska and K. J. Balkus, *J. Phys. Chem.*, 1994, **98**, 12989.

74. M. E. Davis, *Nature*, 2002, **417**, 813.

75. U. Vietze, O. Krauss, F. Laeri, G. Ihlein, F. Schuth, B. Limburg and M. Abraham, *Phys. Rev. Lett.*, 1998, **81**, 4628.

76. T. N. Ivanova, Y. A. Bercovich, A. L. Mashinsky and G. I. Meleshko, *Acta Astronaut*, 1993, **29**, 639.

77. D. L. Bish and J. M. Boak, *Natural Zeolites: Occurrence, Properties, Applications*, 2001, **45**, 207.

78. D. L. Bish and J. W. Carey, *Natural Zeolites: Occurrence, Properties, Applications*, 2001, **45**, 403.

79. F. A. Mumpton, *Proc. Natl. Acad. Sci. U. S. A.*, 1999, **96**, 3463.

80. S. R. Hartmann and E. L. Hahn, *Phys. Rev. A*, 1962, **128**, 2042.

81. C. A. Fyfe, *Nature*, 1987, **325**, 194.

82. C. A. Fyfe, *Solid State NMR for Chemists*, C.F.C. Press, 1984.

83. C. A. Fyfe, H. Strobl, G. T. Kokotailo, G. J. Kennedy and G. E. Barlow, *J. Am. Chem. Soc.*, 1988, **110**, 3373.

84. G. Engelhardt and D. Michel, *High Resolution Solid State NMR of Silicates and Zeolites*, John Wiley & Sons, New York, 1987.

85. C. A. Fyfe, H. Grondey, Y. Feng and G. T. Kokotailo, *Chem. Phys. Lett.*, 1990, **173**, 211.

86. C. A. Fyfe and A. C. Diaz, *J. Phys. Chem. B*, 2002, **106**, 2261.

87. P. Sarv, B. Wichterlova and J. Cejka, *J. Phys. Chem. B*, 1998, **102**, 1372.

88. J. Klinowski, *Chem. Rev.*, 1991, **91**, 1459.

89. C. A. Fyfe, Y. Feng, H. Grondey, G. T. Kokotailo and H. Gies, *Chem. Rev.*, 1991, **91**, 1525.

90. R. J. Cernik, W. Clegg, C. R. A. Catlow, G. Bushnell-Wye, J. V. Flaherty, G. N. Greaves, I. Burrows, D. J. Taylor, S. J. Teat and M. Hamichi, *J. Synchrotron Rad.*, 1997, **4**, 279.

91. M. A. Camblor, M. J. Diaz-Cabanas, P. A. Cox, I. J. Shannon, P. A. Wright and R. E. Morris, *Chem. Mater.*, 1999, **11**, 2878.

2.0 Methodology

2.1 Solid State NMR

2.1.1 Introduction to Solid State NMR

Nuclear magnetic resonance spectroscopy (NMR) is now well established as one of the most powerful methods available to chemists for gaining structural information about a material. NMR spectroscopy involves the probing of transitions between atomic nuclear spin energy levels within a magnetic field by the application of radio-frequency radiation.[1] Solution state NMR is frequently used to determine the structures of proteins and complex organic molecules as well as to provide information on reaction kinetics and dynamics.[2] However, it is often the case that certain materials cannot be studied in solution due to their insolubility. These materials include zeolites, ceramics, glasses, batteries and heterogeneous catalysts, which have all traditionally been studied using diffraction techniques.

Solid state NMR, unlike X-ray diffraction, can probe the local structure of a material and can provide details, such as disorder, that would not normally be accessible by diffraction techniques alone.[3] The NMR of solid samples does, however, differ from that in solution and this has both advantages and disadvantages. The main difference is that the rapid molecular tumbling of the sample in solution is not present in the solid state and therefore, interactions that are normally averaged out in solution are still observed in solids. These interactions often lead to a lack of resolution, with only broad signals being seen in solid state NMR spectra.[4]

The use of high resolution solid state NMR and in particular magic angle spinning (MAS) NMR can remove some of these interactions and lead to sharp resonances in spectra.[5] However, these anisotropic interactions can provide a lot of structural and dynamical information about a material and can be selectively re-introduced and observed in solid state NMR by the use of specialised pulse programs.

2.1.2 Nuclear Spin Interactions

The main interaction on a nuclear spin system during a NMR experiment is that with the external applied magnetic field B_0 named the Zeeman interaction. There are however, other interactions between a nuclear spin and its surroundings, although these are usually orders of magnitude smaller than the Zeeman interaction. These interactions are the chemical shielding (magnetic shielding), the dipolar coupling, the spin-spin coupling (J-Coupling) and quadrupolar coupling. A general Hamiltonian can be written to describe the combination of the sum of all of these interactions:

$$H_{Tot} = H_Z + H_{CS} + H_{DC} + H_{SS} + H_Q \qquad \text{Equation 2.1}$$

All of these interactions are dependent on the orientation of the spin system within the applied magnetic field and therefore have an anisotropic (orientation dependent) term.

In solution state NMR the anisotropic terms are removed due to the rapid random tumbling of the molecules within solution, leading to only the isotropic resonance being observed for each environment of a particular type of nuclei.[6] A basic description of each of these nuclear spin interactions is given below.

2.1.2.1 Zeeman Interaction

The Zeeman interaction occurs for all nuclei that possess the property of spin, I, and have an associated nuclear magnetic moment, μ. This interaction is between the magnetic moment of nuclei and the strong applied magnetic field. The Zeeman interaction is always the most important spin interaction for spin ½ nuclei and leads to the creation of 2I+1 energy levels, where I is the nuclear spin quantum number (Figure 2.1).
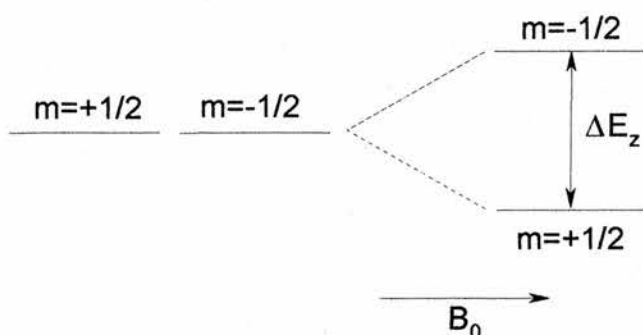
Figure 2.1 Zeeman splitting of the energy levels of a spin ½ nuclei.

The energy of a particular level is given by:

$$E = -\mu B_0 \text{ where } \mu = \frac{\gamma I h}{2\pi}$$

Equation 2.2

The two energy levels are separated by an amount of energy ΔE_z that is field dependent:

$$\Delta E_z = \frac{h\gamma B_0}{2\pi}$$

Equation 2.3

where h is Planck's constant, γ is the magnetogyric ratio and B_0 is magnitude of the applied static magnetic field. The magnetogyric ratio is a fundamental nuclear constant that is unique for any given isotope.

The splitting of the energy levels also dictates the Larmor or observation frequency of specific nuclei and is expressed in terms of γ and B_0:

$$\omega_0 = \gamma B_0 \quad \text{and} \quad \nu_0 = \frac{\gamma B_0}{2\pi} \qquad \qquad \text{Equation 2.4}$$

where ω_0 is the Larmor frequency in rads^{-1} and ν_0 is the Larmor frequency in Hz.

The population difference of the energy levels is described by a Boltzmann distribution with the ratios being given by:

$$\frac{N_\alpha}{N_\beta} = \exp\left(\frac{-\Delta E_z}{kT}\right) \qquad \qquad \text{Equation 2.5}$$

where N_α and N_β are the populations of the lower and upper states respectively, k is the Boltzmann constant and T the temperature. This difference in population is dependent on both the field strength and the nuclear species.

2.1.2.2 Chemical Shielding

NMR occurs when suitable nuclei are placed in a strong magnetic field and are irradiated with radio frequency electromagnetic waves. The resonance condition for just a nucleus (i.e. one without any electrons) is given by:

$$v_0 = \frac{\gamma B_0}{2\pi}$$

Equation 2.6

However, a 'real' nucleus is surrounded by electrons that have the effect of

shielding the nucleus from the external magnetic field B_0. This leads to the effective

field B_{eff} at the nucleus usually being slightly smaller than B_0 and the resonance

condition becomes:

$$v_{obs} = v_0 + \Delta v$$

Equation 2.7

The effect of B_{eff} is to slightly alter the Larmor frequency of the nucleus and this is

what is referred to as the chemical shift (δ). The chemical shift is highly sensitive to

the electronic structure and hence to local structural and chemical environment. The

values of chemical shift are measured by the frequency difference from a reference

material, e.g. tetramethylsilane, and the units reported in parts per million (ppm).

$$\delta = \frac{10^6 (v_{sample} - v_{ref})}{v_{ref}}$$

Equation 2.8

In solid state NMR the chemical shift is a directional quantity and varies with a

crystallites orientation within the magnetic field, leading to a chemical shift anisotropy

(CSA). Therefore, for a single crystal in a magnetic field the position of the resonance

in the NMR spectrum will depend on the orientation of the crystal. In the case of a

powdered sample where all possible orientations are available, the spectrum contains a

broad peak that is the sum of all the individual resonances (Figure 2.2c).

The chemical shift anisotropy can be described numerically by a 3 x 3 matrix or

tensor, which characterises the three-dimensional nature of the interaction. If the CSA

tensor is converted to a 'diagonal form' using the correct coordinate system then the three diagonal principal components (δ_{11}, δ_{22}, δ_{33}) and three Euler angles can be used to fully describe the CSA tensor. The CSA may also be described in terms of the isotropic chemical shift (δ_{iso}), the anisotropy parameter (δ_{aniso}) and the asymmetry parameter (η) where:

$$\delta_{iso} = \frac{1}{3}(\delta_{11} + \delta_{22} + \delta_{33}) \quad \delta_{aniso} = \delta_{33} - \delta_{iso} \quad \eta = \frac{\delta_{22} - \delta_{11}}{\delta_{aniso}} \qquad \text{Equation 2.9}$$

The CSA can be reduced or removed by magic angle spinning for high resolution solid state NMR, as will be described later in this chapter.
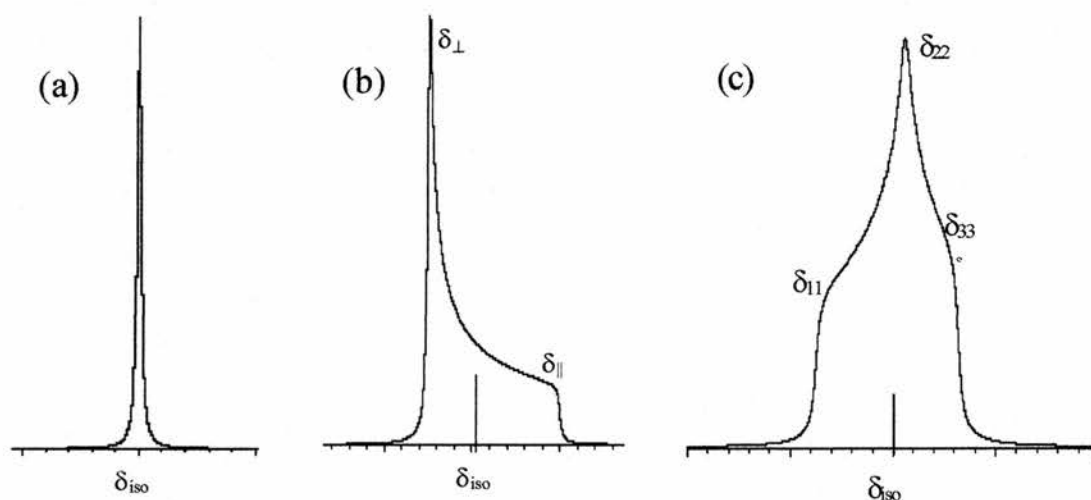
Figure 2.2 Simulated powder lineshapes of shift anisotropy patterns. (a) isotropic chemical shift (MAS) (δ_{iso}), (b) axially symmetric shielding powder pattern, (c) asymmetric shielding powder pattern.

2.1.2.3 Dipolar Coupling

Dipolar coupling or dipole-dipole interactions occur when the magnetic moments of a collection of spins interact through space. Each spin acts like a small bar magnetic with its own local magnetic field that other surrounding spins feel and interact with. This interaction is a major cause of line broadening in solids NMR of powders, but is averaged to zero in the solution state due to the rapid random tumbling of the molecules in solution. Dipolar coupling can occur between nuclei of the same type e.g. ^{1}H-^{1}H (homonuclear) or between different nuclei e.g. ^{1}H-^{13}C (heteronuclear).
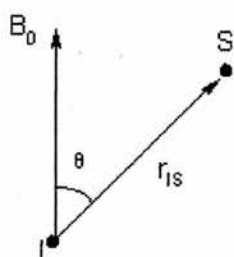
Figure 2.3 Dipole-dipole interaction between two nuclei I and S.

The magnitude of the dipolar coupling (b_{IS}) between two nuclei I and S is dependent on the distance between them (r), a function of the magnetogyric ratios of the nuclei, and the angle (θ) between the internuclear vector and the applied magnetic field.

$$b_{IS} = \frac{\mu_0 \gamma_I \gamma_S \hbar}{8\pi^2 r^3}(3\cos^2\theta - 1) \quad \text{where} \quad \frac{\mu_0 \gamma_I \gamma_S \hbar}{8\pi^2 r^3} = D_{IS} \text{ (in Hz)} \qquad \text{Equation 2.10}$$

and $\mu_0 = 4\pi \times 10^{-7}$ kg m s^{-2} A^{-2} and is the permittivity of free space, γ_I and γ_S are the magnetogyric ratios for nuclei I and S respectively, $\hbar = h/2\pi$ where h is the Planck constant 6.6261×10^{-34} Js and D_{IS} is the dipolar coupling constant.

The effects of dipolar coupling can be reduced and even removed by magic angle spinning and high power decoupling as will be described later in this chapter. The dipolar interaction can also be selectively reintroduced in MAS experiments and due to the distance dependence of the coupling, it can be used to measure internuclear distances in the case of isolated spin pairs, as applied in Chapter 5.

2.1.2.4 *Spin-Spin Coupling*

The spin-spin coupling or *J*-coupling is an interaction between a pair of nuclei and occurs via the bonding electrons. The coupling can be both homonuclear and heteronuclear and is independent of the strength of the applied magnetic field. Values for the *J*-coupling are usually much smaller than for the other interactions, but still lead to changes in the Zeeman energy levels and can lead to additional resonance frequencies. The *J*-coupling is not reduced by the isotropic tumbling in solution or by MAS in the solid state and is frequently used to provide information on the structures of molecules, particularly in solution state NMR.

2.1.2.5 *Quadrupolar Coupling*

Nuclei that have a spin quantum number I greater than ½ are termed quadrupolar nuclei and these make up over two thirds of the periodic table. Quadrupolar nuclei include ^{11}B, ^{27}Al and ^{49}Ti, all of which have odd half integer spin quantum numbers, I

= 3/2, 5/2, 7/2 respectively. Quadrupolar nuclei undergo Zeeman splitting in the same way as spin ½ nuclei, but have more energy levels and therefore multiple transitions and hence multiple resonances for a single nucleus can occur (Figure 2.4).
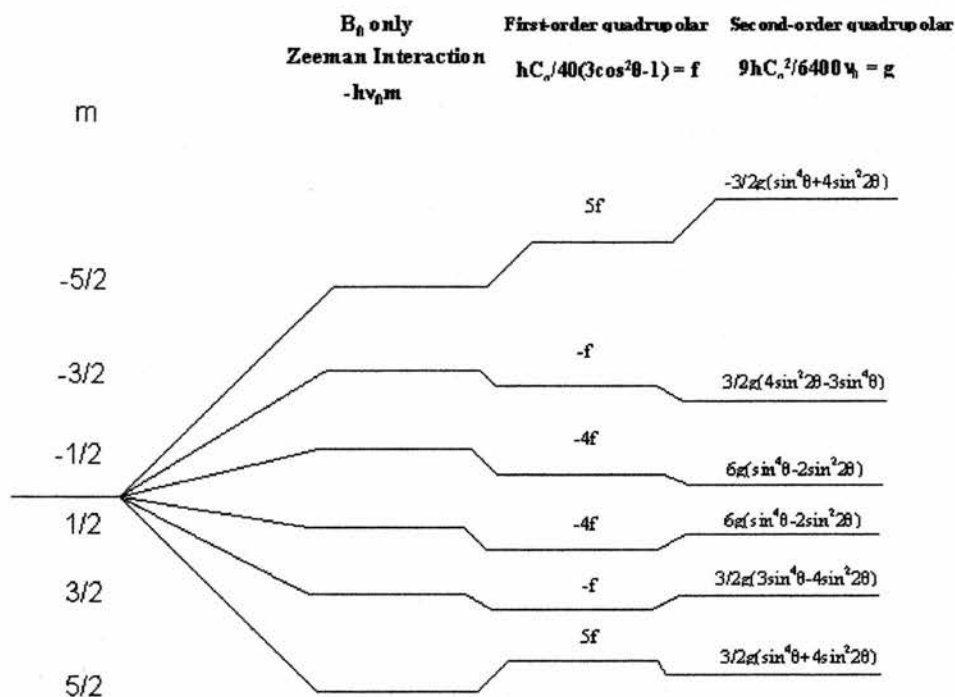
Figure 2.4 Energy level diagram for a single I=5/2 nuclei (e.g. ^{27}Al) under Zeeman only interaction, and Zeeman plus first order and second order quadrupolar perturbations. Redrawn from ref 7.

Nuclei with I > ½ have a quadrupole moment (eQ) caused by the non-spherical distribution of electrical charge. This moment interacts with the electric field gradient present in a sample due to the asymmetric distribution of electrons around the nucleus. This interaction, like that for the dipolar coupling and the chemical shift anisotropy, is asymmetric and leads to powder pattern in the NMR spectrum. The line widths and shapes of these powder patterns are dependent on two parameters: (1) the quadrupolar

coupling constant, $C_q = e^2qQ/h$ and (2) the asymmetry parameter, η^q. The quadrupolar coupling constant is proportional to the product of the electric field gradient along its principal axis and the nuclear electric quadrupole moment.

Many techniques have been developed to reduce the quadrupolar anisotropy and hence, increase spectral resolution and these include multiple quantum magic angle spinning (MQMAS), double rotation (DOR) and dynamic angle spinning (DAS). Several good reviews have been published on quadrupolar solid state NMR and the methods available to reduce the quadrupolar anisotropy.[8,9]

2.1.3 The Vector Model

The vector model of NMR spectroscopy provides a simple, non-mathematical description of the behaviour of an isolated spin ½ nuclei during an NMR experiment. The model has only limited use for systems in which nuclei interact, but is the basis of more in-depth descriptions of NMR theory, which are beyond the scope of this thesis. A ^1H nucleus with spin quantum number $I=1/2$ has 2 non-degenerate energy levels, often labelled α and β, when placed in an applied magnetic field. In a classical description the nuclear magnetic moment precesses in the magnetic field B_0 with its axis aligned either parallel (low energy) or antiparallel (high energy) to the field.
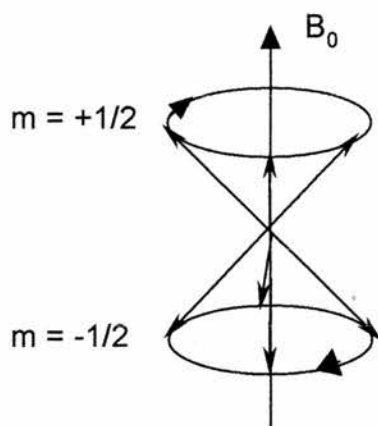
Figure 2.5 Vector model of the low and high energy precession states of a spin ½ nuclei.

A sample at thermal equilibrium has a bulk magnetisation M, which is stationary and aligned parallel to B_0, and is caused by there being a slight excess of spins in the lower energy level. The direction of B_0 defines the z` axis of an x`, y`, z` coordinate system, which is referred to as the laboratory frame. During a NMR experiment it is necessary to perturb the equilibrium and this is achieved by the application of a r.f. field (B_1) at the Larmor frequency of the nucleus perpendicular to B_0. The effect of this pulse is to tilt the net magnetisation vector M away from the z` axis and to start it precessing about the z` axis. This motion is best viewed in a rotating frame, which rotates about the z` axis at the frequency of the applied r.f. field (B_1). In this rotating frame the applied r.f. field B_1 appears to be stationary and the net magnetisation appears to process (or nutates) about it at a frequency called the nutation frequency $\omega = \gamma B_1$.
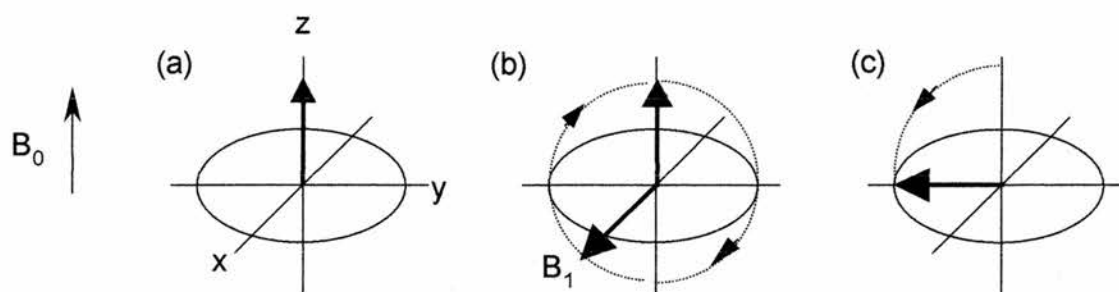
Figure 2.6 (a) Net magnetisation is aligned along the z axis (B_0) of the rotating frame. (b) An r.f. field (B_1) is applied along the x axis and the net magnetisation (M) precesses about the B_1 field. (c) A 90_x° pulse flips the magnetisation along the –y axis.

In the simplest of NMR experiments, a single short pulse is applied to a sample at a frequency close to the resonance frequency of the spins ω_0, so that B_1 is much greater than the offset field ΔB. If B_1 is applied along the x axis it will cause the net magnetisation to precess in yz plane, as shown in Figure 2.6b, with the angle through which the magnetisation has turned being the flip angle β:

$$\beta = \gamma \, B_1 \, t_p \hspace{4cm} \text{Equation 2.11}$$

where t_p is the duration of the pulse in seconds. For example, a 90_x° pulse rotates the bulk magnetisation M from the z axis by 90° to the –y axis (Figure 2.6c). After the B_1 field is turned off, the net magnetisation does not remain in the xy plane indefinitely. Instead, the z magnetisation returns to its equilibrium value restoring the populations of the energy levels back to their equilibrium Boltzmann distribution by a process called spin-lattice relaxation with a time constant of T_1 (Figure 2.7a). The xy magnetisation decays to zero by undergoing free induction decay (FID) with a time constant T_2 and is referred to as spin-spin relaxation (Figure 2.7b).

(a)

(b)
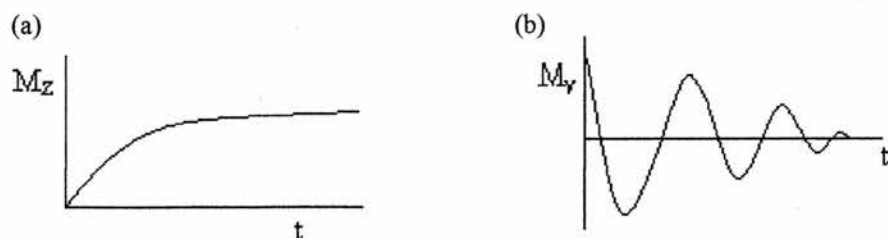
Figure 2.7 (a) The z component of the magnetisation grows back with a time constant T_1. (b) The xy components of M decay towards zero with a time constant T_2.

The free induction decay of the xy magnetisation, which is the sum of all the individual oscillating voltages from the various nuclei in the sample, is detected by the NMR spectrometer via the voltage generated in the receiver coil. The FID is then Fourier transformed to generate a NMR spectrum with line widths of $(\pi T_2)^{-1}$.

2.1.4 NMR Relaxation Processes

2.1.4.1 Spin-Lattice Relaxation Time (T_1)

The spin-lattice or longitudinal relaxation describes the rate at which the z component of the net magnetisation (M_z) returns to its full magnitude (M_0) along the z axis after a pulse or series of pulses. This process is actually the return of a perturbed spin system back to the equilibrium population levels as described by a Boltzmann distribution (Equation 2.12)

$$\frac{N_\beta}{N_\alpha} = \exp(-\frac{\Delta E}{kT}) = \exp(-\frac{2\mu\mu_0}{kT})$$

Equation 2.12

To restore this Boltzmann distribution requires the exchange of energy between the spin system and its surroundings, often referred to as the lattice.

The rate at which these population levels are restored to their equilibrium values is characterised by the rate constant T_1 and the process is assumed to be a first order kinetic one, described by the equation:

$$\frac{dM_z}{dt} = -\frac{(M_z - M_0)}{T_1}$$

Equation 2.13

The spin-lattice relaxation time is usually measured by two methods, Saturation Recovery and Inversion Recovery experiments, the former of which is illustrated in Figure 2.8.
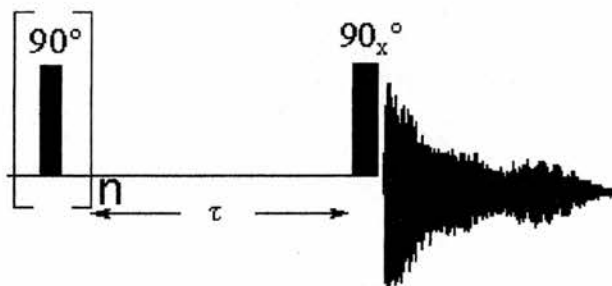
Figure 2.8 Saturation recovery pulse sequence for the measurement of T_1

In the saturation recovery experiment a series of $\pi/2$ pulses are applied in rapid succession in order to saturate the nuclear spins. After a set time, τ, a $\pi/2$ pulse along the x axis is applied and a FID is collected, the experiment is repeated for several increasing values of τ. The magnitude of the FIDs increases with increasing values of τ as the magnetisation returns to its equilibrium value before the final $\pi/2$ pulse.

2.1.4.2 Spin-Spin Relaxation (T_2)

Spin-spin or transverse relaxation is a measure of the rate at which the net magnetisation is lost in the xy plane after a pulse, owing to an exchange of energy between two spins, and is described by the rate constant T_2. This net magnetisation in the xy plane (M_{xy}), produced by the application of a r.f. pulse, precesses at a variety of frequencies throughout the sample. This is due to the wide range of local fields in the applied magnetic field B_0, as well as local fields caused by the neighbouring nuclear dipoles. The measurement of M_{xy} (T_2) as a function of time can give information about the local fields and can be useful when studying dynamical and structural properties of a material. T_2 rates are usually measured by Spin Echo experiments, with the most common being the Carr-Purcell-Meiboom-Gill (CPMG) pulse sequence

2.1.4.3 Spin-Lattice Relaxation in the Rotating Frame ($T_{1\rho}$)

The spin-lattice relaxation time for spins in the rotating frame, describes the rate at which a nuclear magnetisation, spin-locked in the rotating frame, reapproaches its thermal equilibrium value.

In the rotating frame a 90° pulse along the x axis rotates the net magnetisation from the z axis to the y axis. A second pulse at 90° to the previous one (B_1) spin locks the magnetisation along the y axis and the spins precess about B_1. The spins do not undergo spin-spin relaxation as previously discussed, as the spin locking field (B_1) acts like a static field. As the effective magnetic field in the rotating frame is orders of magnitude smaller than B_0, the magnetisation in the rotating frame will decay towards its equilibrium value with a time constant $T_{1\rho}$. $T_{1\rho}$ relaxation times are measured

using a spin-locking experiment, as illustrated in Figure 2.9, with the values of $T_{1\rho}$ being important parameters in cross polarization experiments.
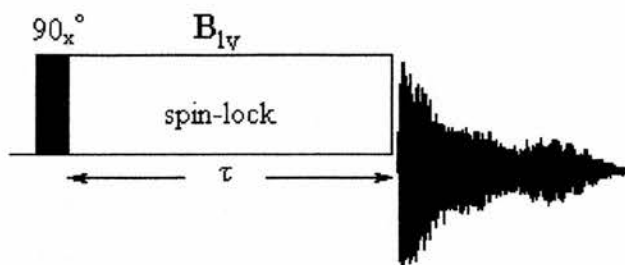
Figure 2.9 Spin-lock pulse sequence for the measurement of $T1_\rho$

$T_{1\rho}$ is measured by performing a series of experiments in which the length of time that the spin-lock field is applied (τ) is varied. Removal of the spin-lock field allows a FID to be obtained, the amplitude of which decreases with increasing spin-lock time, as the magnetisation decays.

2.1.5 High Resolution Solid State NMR

Many of the magnetic interactions described earlier affect the resolution of the spectra seen in solid state NMR experiments. This is mainly due to the restricted motion of the atoms and molecules in the solid state as compared to those in solution for which the rapid tumbling motion removes many of the interactions. For spin ½ nuclei the greatest causes of line broadening are the dipole-dipole interactions and the chemical shift anisotropy. This broadening often leads to the overlapping of several individual resonances in a spectrum and makes any form of interpretation almost impossible. This has led to a need for techniques to reduce or even remove the effects of the dipolar coupling and the CSA, and to increase the signal strength of low

abundance nuclei such as ^{29}Si (4.7 % abundant) and ^{13}C (1.1 % abundant). There are

a number of techniques available to help produce well resolved spectra for solid

samples and these include magic angle spinning (MAS), high power decoupling and

cross polarization (CP). These techniques are often combined to produce very high

resolution spectra of spin ½ nuclei and a description of each is given below.

2.1.5.1 Magic Angle Spinning (MAS)

The rapid random tumbling motion of molecules in solution that averages out the

dipolar interactions and the CSA in solution state NMR can be mimicked in solid state

NMR by spinning the sample about an axis at an angle θ_R to B_0. This technique is

known as magic angle spinning (MAS) and is now routinely used in solid state NMR

experiments to reduce the CSA and dipolar interactions as well as to narrow lines for

quadrupolar nuclei. As previously mentioned the dipolar interaction and the CSA

have an orientation dependence, which is in the form of $3\cos^2\theta$-1, where θ is an angle

that describes the orientation of the spin interaction tensor (e.g. dipolar coupling

tensor) as illustrated in Figure 2.10.
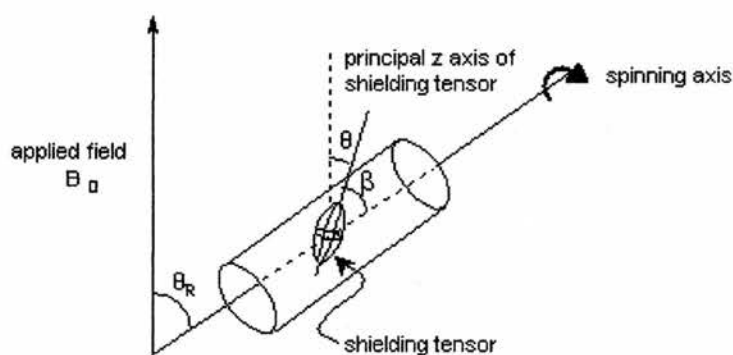
Figure 2.10 Magic angle spinning. The sample is spun about at an axis orientated at the magic angle

(θ_R=54.74°) with respect to the applied magnetic field B_0. The chemical shielding tensor, represented

by an ellipsoid, rotates with the sample. The angle θ is the angle between B_0 and the principal z axis of

the shielding tensor; β is the angle between the z axis of the shielding tensor principal axis frame and

the spinning axis. Redrawn from ref. 6.

In a powder sample all the molecular and hence all the interaction tensor

orientations are possible, so the angle θ effectively takes on all possible values. If the

sample is then spun about an axis orientated at the angle θ_R to B_0, then θ will vary with

time and the orientation dependence becomes:

$$<3\cos^2\theta-1> = \frac{1}{2}(3\cos^2\theta_R -1)(3\cos^2\beta-1) \qquad \text{Equation 2.14}$$

where the angle β is between the principal z axis of the shielding tensor and the

spinning axis. If the angle θ_R is set to 54.74 ° then $(3\cos^2\theta_R-1) = 0$ and so the average

$<3\cos^2\theta-1>$ is also zero, and if the spinning rate is high enough, the CSA and the

heteronuclear dipolar couplings are averaged to zero. This angle of 54.74 ° is known

as the magic angle.

Should the rate of spinning be smaller than 3 times the value of the CSA then

spinning sidebands will be produced. These spinning sidebands are lines, which are

separated by the spinning rate and radiate out from the line at the isotropic chemical

shift. The overall intensity of the spinning sidebands maps out the chemical shift

anisotropy as seen in the static powder spectrum. Analysis of the intensities of the

spinning sidebands can give values for the principal tensor elements of the CSA as

used in Chapter 5 to determine F-Si internuclear distances.

Magic angle spinning can also be used to reduce the effects of quadrupolar line

broadening, especially for nuclei that have weak quadrupole moments for which first

order perturbation theory holds well. Again, this is due to the orientation dependence of the first order quadrupole interaction, which like the dipolar interaction is described by the term $(3\cos^2\theta-1)$. As shown above, θ can be averaged to zero by spinning rapidly at the magic angle, although for most quadrupolar nuclei there is a large second order contribution that cannot be removed by spinning at the magic angle.

MAS NMR has been shown to provide much higher levels of resolution than could ever be achieved in static spectra, but frequently samples cannot be spun at sufficient rates to remove the heteronuclear dipolar interactions and therefore high power decoupling is often required in addition.

2.1.5.2 High Power Decoupling

The simplest of techniques to reduce the linewidths in solid state NMR spectra, especially the heteronuclear dipolar coupling is high power decoupling. The technique is mainly used to remove the coupling between ^1H or ^{19}F with other nuclei such as ^{13}C. The method involves the application of continuous very high power fields (100 – 1000 watts) at the resonance frequency of the ^1H or ^{19}F nuclei, whilst collecting the spectra for the other nuclei. High power decoupling can also be used to remove homonuclear dipolar couplings but this requires the use of multiple pulse sequences such as WAHUHA[10] and MREV-8.[11] These pulse sequences are important for removing the very strong ^1H-^1H homonuclear dipolar coupling, which cannot be removed by magic angle spinning.

High power decoupling is often combined with other techniques for reducing linewidths and increasing signal strength such as MAS and CP.

2.1.5.3 Cross Polarization (CP)

Cross polarization is a technique for increasing the sensitivity of dilute spins such as natural abundance ^{13}C by making use of the spin interactions with abundant nuclei such as ^{1}H and ^{19}F.[12] There are two main problems with observing nuclei such as ^{13}C, the first is the low natural abundance of the NMR active nuclei making the signal to noise ratio very low. The second is that low abundance nuclei tend to have very long T_1 relaxation times and this leads to the length of time between successive scans being long, often several minutes. The combination of these two facts means that to collect a spectrum with a sufficiently high signal to noise ratio can take several hours or even days. Cross polarization solves both of these problems, firstly by increasing the population difference between the spin up and down states for the dilute species up to a maximum of γ_I/γ_S. Secondly, by effectively cutting down the relaxation time and therefore the experiment recycle time due to the overall relaxation time being dependent on the T_1 relaxation of the abundant spins.
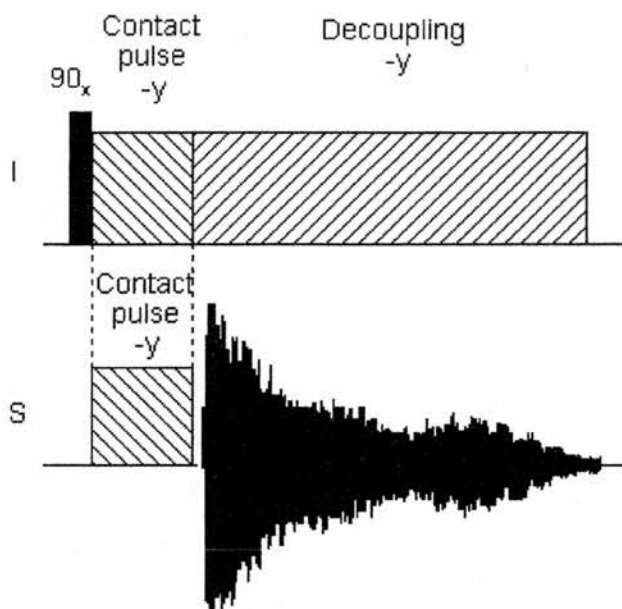
Figure 2.11 The pulse sequence for the cross polarization from abundant I spins to dilute S spins.

The pulse sequence for the cross polarization transfer from abundant I spins to dilute S spins is shown in Figure 2.11. A $90_x°$ pulse is firstly applied to the abundant I spins and then they are spin locked along the –y axis by the application of an on resonance field along –y. Simultaneously a r.f. field is applied at the resonance frequency of the S spins (contact pulse). The S spins precess about the applied field B_{IS} with an angular frequency $\omega_{IS} = \gamma_S B_{IS}$. If the applied r.f. fields to the I and S spins are adjusted so that the Hartmann-Hahn[13] match condition $\gamma_I B_{1I} = \gamma_S B_{1S}$ is satisfied such that the angular frequencies of the precession about B_{IS} are equal $\omega_{1I} = \omega_{1S,}$ then the I and S spins will have same time dependence in the rotating frame.

The energy levels for the I and S spins have now essentially the same energy difference under the Hartmann-Hahn match condition and a resonance energy exchange can take place between the two spin systems. The mechanism of this

exchange is through mutual spin flipping controlled by the I-S dipolar couplings. The dynamics of the cross polarization can be described well by the concept of spin temperature and the flow of heat. The abundant I spins are highly polarised and have a cold spin temperature, whilst the dilute S spins have a high spin temperature. Under the Hartmann-Hahn match condition, heat flows between the I and S spins until the systems are equal, and as the I spin system has a larger heat capacity, the S spin system is cooled to the initial spin temperature of the I spins. The spin temperature of the S spin system is reduced by a factor of γ_S / γ_I and corresponds to an increase in the magnetisation by a factor of γ_I / γ_S. At the end of the contact time there is observable S spin magnetisation in the xy plane that can be recorded by collecting an FID. Cross polarization can be combined with high power decoupling and MAS to give high resolution spectra in a much shorter time period than would be possible without these techniques.

2.1.6 Experimental Details

2.1.6.1 NMR Spectrometers

The experiments were performed on a Varian Infinityplus NMR spectrometer operating at frequencies of: 500.156 MHz for ^1H; 470.531 MHz for ^{19}F; 99.355 MHz for ^{29}Si; 122.606 MHz for ^{27}Al; and 50.68 MHz for ^{15}N. The spectrometer was equipped with one 1000 W amplifier for ^1H and ^{19}F and two 300 W amplifiers for the lower frequency nuclei. The spectrometer was controlled from a Sun Workstation running the Chemagnetics Spinsight software.

The experiments on SSZ-44 were performed at the University of British Columbia on a Bruker Avance DSX-400 NMR spectrometer operating at frequencies of: 400.13 MHz for ^1H; 376.343 MHz for ^{19}F; and 79.495 MHz for ^{29}Si. The spectrometer was equipped with two 1000 W amplifiers for ^1H and ^{19}F as well as two 300 W amplifiers for the lower frequency nuclei. The spectrometer was controlled from a Silicon Graphics workstation, running Bruker's XWIN-NMR software.

2.1.6.2 Probes

Solid state NMR experiments using the Varian Infinityplus spectrometer were performed using two magic angle spinning probes. The variable temperature work on ^{29}Si was performed on a Chemagnetics 7.5 mm double resonance MAS probe. This probe was capable of spinning the sample at rates of up to 7 kHz, with a stability of ± 5 Hz as it was equipped with an optical spin rate detector that controlled the bearing and drive pressures. The rest of the experiments were performed on a Chemagnetics 4.0 mm triple resonance (H/X/Y) CP MAS probe. This probe was capable of spinning sample at rates of up to 18 kHz, again with a stability of ± 5 Hz due to the optical spin rate detector. Modest r.f. powers gave 90° pulses for ^1H, ^{19}F and ^{29}Si of between 3 and 6 μs. Both probes were capable of variable temperature work between the ranges of 120 K and 520 K, the temperature of which was controlled by a Varian temperature control unit.

The work on the Bruker Avance spectrometer was performed on a Bruker 4.0 mm H/X/Y triple resonance CP MAS probe. The probe was capable of spinning samples at rates of up to 15 kHz with a stability of ± 5 Hz, as it was equipped with an optical sensor controlling the bearing and drive pressures.

2.1.6.3 Magic Angle Spinning

Samples were packed in 4mm or 7.5 mm zirconia rotors with Teflon end caps for the majority of the experiments. ^{19}F experiments required end caps and spacers with no fluorine background and therefore ones made from Vespel were used. The magic angle was set using the spinning sidebands of the ^{79}Br resonance of potassium bromide. The 'spikes' in the FID were optimised to decay out to 10 ms by varying the angle of the MAS housing. All the spin rates during experiments were controlled by the Varian MAS unit, which used an optical detector on the probe and a negative feedback loop to control the bearing and drive pressures. For ambient and high temperature experiments the gas used for the drive and bearing was compressed air.

2.1.6.4 Variable Temperature Experiments

All of the ^{29}Si MAS variable temperature experiments were performed using a Chemagnetics 7.5 mm double resonance probe capable of temperatures between 120 and 520 K. Low temperature experiments were performed with nitrogen as both the bearing and drive gasses and the temperature controlled using a Varian temperature control unit. The samples were heated / cooled by gas supplied from a Varian variable temperature stack, which was supplied with cold gas produced using a heat exchange coil placed in a 25 L dewar of liquid nitrogen. An electric heater in the variable temperature stack warmed the gas as necessary and this was controlled by a negative feedback system to the computer.

The variable temperature, bearing and drive gasses were all produced by the 'boil-off' from a 200 L liquid nitrogen dewar, which provided enough gas for approximately 8 hours at a spinning rate of 2 kHz. To keep the sample below ambient temperature required the dewar containing the heat exchange coil to be filled approximately every hour. These two factors heavily influenced the number of acquisitions that could be collected for a sample at low temperatures and therefore, the desired signal to noise ratios could not always be achieved.

The probe temperature was calibrated using the ^{207}Pb chemical shift of PbNO$_3$ following the procedure by Dybowski.[14] An initial static spectrum was collected at 295 K and the isotropic shift referenced to –3490.4 ppm. To convert between the ^{207}Pb chemical shift and temperature, the following relationship proposed by Dybowksi was used:

$$T(K) = \frac{3714.5 + {}^{207}Pb\ chemical\ shift}{0.753}$$

<div style="text-align:right">Equation 2.15</div>

Several spectra were then collected at a variety of temperatures for spin rates of 2, 3 and 4 kHz and the chemical shifts converted to temperature using the relationship in Equation 2.15. A plot of observed temperature vs. set temperature is shown in Figure 2.12 for the three spinning speeds and for a linear correlation. It can be seen that the observed temperature is slightly lower than the set temperature above 0°C, however, below 0°C the two temperatures start to differ quite significantly. Examination of the isotropic peak widths at half height revealed that there was some unequal heating / cooling of the sample leading to temperature gradients, although these were fairly small and regular. All the temperatures reported in this thesis are the observed

temperatures with the value for the set temperature having been calculated from the

equations for the lines of best fit in Figure 2.12. Variable temperature experiments

were usually performed using a 2 to 3 kHz spin rate to limit sample heating due to

friction and to conserve the nitrogen gas supply.
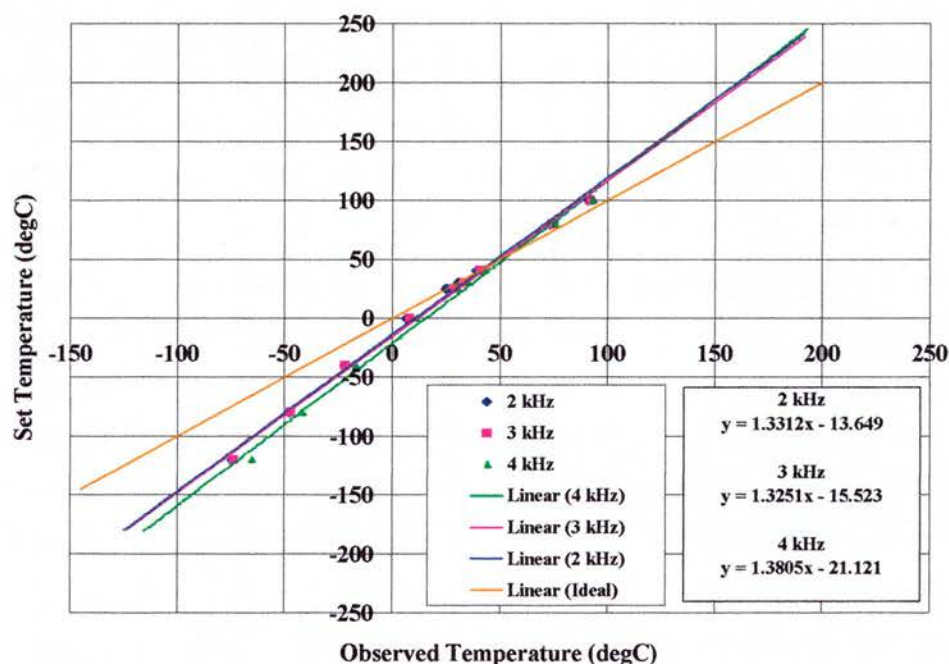
Figure 2.12 Temperature calibration plot for 7.5 mm probe using the [207]Pb chemical shift of PbNO$_3$.

2.1.6.5 Reference Samples

The experimental conditions were first determined for a reference sample before

the actual sample under investigation. This generally consisted of determining pulse

lengths, CP matching conditions and setting the chemical shift reference.

^{29}Si and ^{29}Si{^{1}H} CP MAS experiments were generally set-up on the cubic octamer,

Q$_8$M$_8$, Si$_8$O$_{12}$[OSi(CH$_3$)$_3$] (Figure 2.13), which was synthesised by Katherine Haxton

according to literature procedures. [15] The Q$_8$M$_8$ sample shows six lines in its ^{29}Si{^{1}H}

CP MAS spectrum and the highest field peak is set to -109.7 ppm relative to TMS. The four peaks at the high field end of the spectrum give an indication of how well the magic angle is set and the quality of the shimming due to their narrow line widths (Figure 2.14).
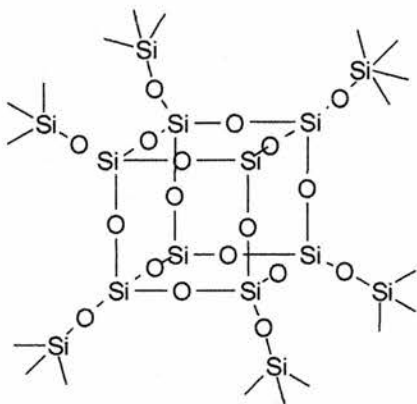
Figure 2.13 Cubic octamer Q_8M_8, with only six of the 'arms' shown for clarity.

$^{29}Si\{^{19}F\}$ CP and ^{19}F MAS experiments were set-up on octadecasil, which was synthesised according the method in Chapter 3.2.2.1.[16] The ^{29}Si spectrum of octadecasil shows two lines with an intensity ratio of 1:4 with the lowest field resonance having a chemical shift of -107.8 ppm. The ^{19}F MAS NMR spectrum of octadecasil shows only one peak at a chemical shift of -38.2 ppm. ^{27}Al and ^{15}N MAS experiments were set-up on an aqueous sample of aluminium nitrate and a solid sample of ammonium nitrate respectively. The single resonance seen in the static ^{27}Al spectrum of aluminium nitrate was set to a chemical shift of 0.0 ppm, and the single ^{15}N resonance observed in the ammonium nitrate spectrum was set to a chemical shift of -5.1 ppm relative to liquid nitromethane.
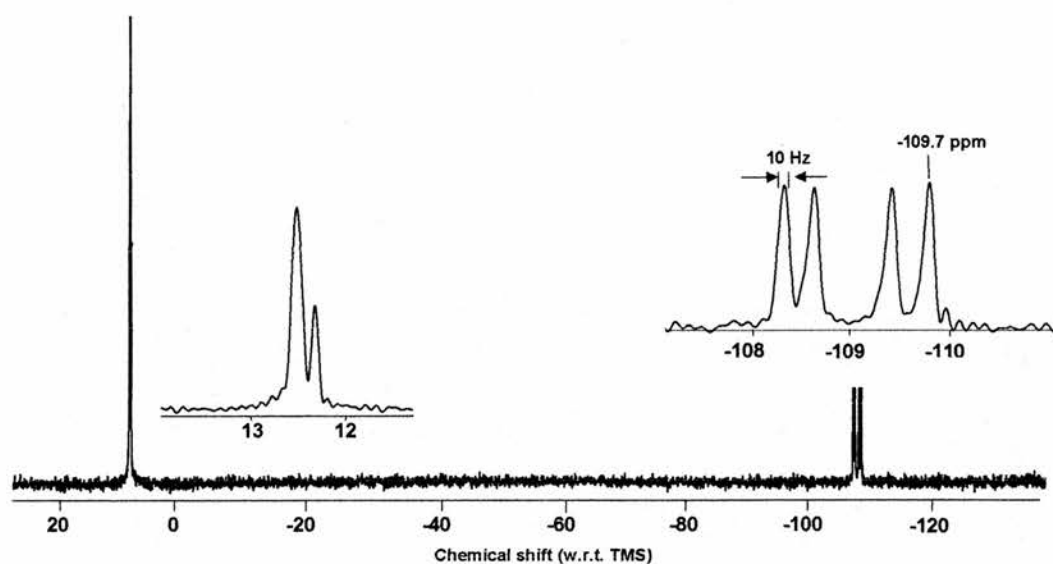
Figure 2.14 ^{29}Si{^{1}H} CP MAS NMR spectrum for Q_8M_8. Spectrum collected at a 4kHz spin rate, 3 ms contact time and 2 s recycle time.
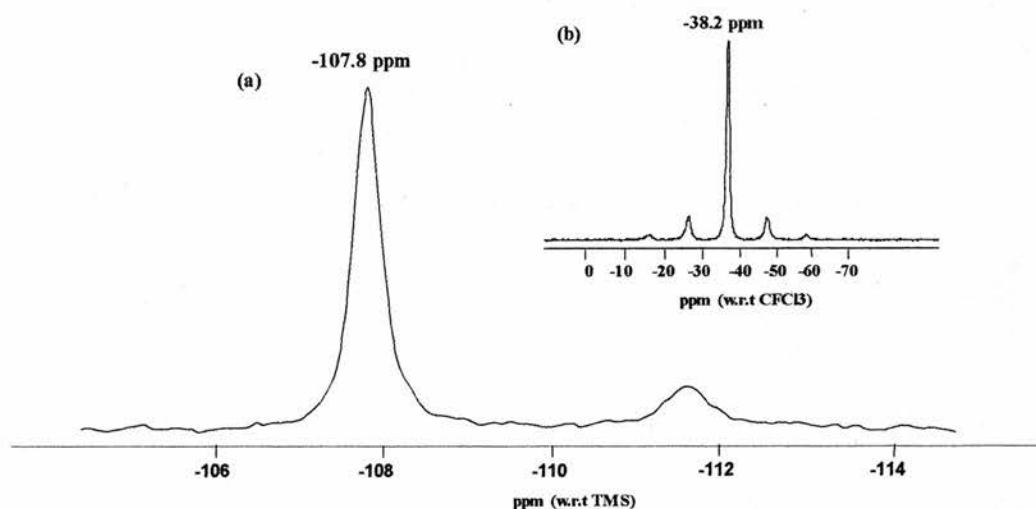
Figure 2.15 (a) ^{29}Si and (b) ^{19}F MAS NMR spectra of octadecasil. The ^{29}Si spectrum was collected at a 3 kHz spin rate and a 300 s recycle time. The ^{19}F spectrum was collected at a 2.5 kHz spin rate and a 60 s recycle time.

Nuclei	Secondary reference sample	Reference chemical shift	Solid or Liquid
^{15}N	Ammonium nitrate	-5.1 ppm relative to neat liquid nitromethane	Solid
^{19}F	Octadecasil	-38.2 ppm relative to liquid $CFCl_3$	Solid
^{27}Al	Aluminium nitrate	0.0 ppm	Liquid
^{29}Si	Q_8M_8 or Octadecasil	-109.7 or -107.8 ppm relative to TMS	Solid

Table 2.1 Secondary reference samples and their chemical shifts.

2.1.6.6 ^{29}Si MAS and ^{29}Si{^{1}H} CP MAS NMR Experiments

^{29}Si MAS NMR experiments were mainly performed on a Chemagnetics 7.5 mm probe with a spinning rate of between 3 – 4 kHz, which was usually more than sufficient to remove the ^{29}Si chemical shift anisotropies. The experiments were initially set-up using Q_8M_8 as the reference sample before switching to the sample to be investigated. The r.f. power for an appropriate pulse duration (e.g. 90° pulse) was determined on the reference sample by using the Spinsight array function to vary the power levels for a fixed pulse duration, typically 4 µs. The collected spectrum was referenced setting the highest field peak to –109.7 ppm, which had previously been determined from TMS. The T_1 relaxation times for the sample under investigation were then determined using the saturation recovery method. As the samples usually gave more than one resonance in their ^{29}Si spectrum, the recycle time was determined for the peak with the largest T_1 relaxation time. This led to the recycle time being set to at least 5 times the largest T_1 relaxation time, for a 90° pulse. Typically as many acquisitions as necessary for a sufficient signal to noise ratio were collected, and the exact value varied with sample.

^{29}Si$\{^1$H$\}$ CP MAS experiments were set-up initially on Q_8M_8 to determine the parameters needed for the actual sample. ^{1}H MAS NMR spectra were initially collected on the sample and the ^{1}H signal set on resonance. The ^{29}Si r.f. powers were then varied using the Spinsight array feature to find the Hartmann-Hahn match condition(s) at a fixed ^{1}H power and a known spin rate. The ^{29}Si and ^{1}H pulse durations were then checked by arraying the values and observing the maximum signal. The recycle time used was typically set to give the maximum signal to noise and was usually 1.25 x ^{1}H T_1 relaxation time. The contact time (CT) used was typically 3 ms, although the array function was again used to determine the exact contact time for the sample. ^{29}Si$\{^1$H$\}$ CP experiments were typically performed with a spinning rate of 3 kHz unless otherwise stated.

2.1.6.7 ^{29}Si$\{^{19}$F$\}$ CP MAS NMR Experiments

The ^{29}Si$\{^{19}$F$\}$ CP experiments were performed on a Bruker Avance spectrometer using a 4mm probe capable of providing strong r.f. pulses and very stable control over the spinning rate. The experimental conditions were initially determined on octadecasil and then accurately redetermined for the SFF sample. ^{19}F MAS NMR spectra were initially collected and the ^{19}F frequency set on resonance and the ^{19}F T_1 relaxation time measured using the saturation recovery method. The recycle time was then set to 1.25 times T_1, which gave a 15 s recycle time for the SFF sample. The ^{19}F r.f. power was then fixed whilst the CP match condition for the +1 spinning sideband of the CP matching profile was carefully found by varying the ^{29}Si r.f. power in very small steps. The ^{19}F and ^{29}Si pulse durations were then accurately measured by varying the pulse duration for ^{19}F and by varying a 'flip-back' pulse applied after CP

for ^{29}Si. The ^{29}Si{^{19}F} CP curves were acquired by collecting a series of ^{29}Si{^{19}F} CP spectra with incrementing contact time. The spinning rate for the SFF sample was set to 12 kHz and accurately maintained using the spin rate controller.

2.1.6.8 ^{27}Al, ^{15}N and ^{15}N{^{1}H}CP MAS NMR Experiments

^{27}Al MAS NMR spectra were collected using a Chemagnetics 4 mm probe, which was capable of spinning the sample at 15 kHz to reduce the effects of quadrupolar broadening. The experiments were initially set-up on an aqueous 1M solution of aluminium nitrate and the ^{27}Al r.f. powers determined for a known pulse duration. The actual ^{27}Al r.f. power used for the solid samples was reduced to a third of the value determined on the aqueous solution of aluminium nitrate and the samples were spun at 15 kHz with a 1 s recycle time.

^{15}N and ^{15}N{^{1}H} CP experiments were performed using a 4 mm probe, which was capable of tuning to the relatively low frequency required for ^{15}N. The pulse lengths, CP match conditions and chemical shift reference were firstly determined on a ^{15}N enriched ammonium nitrate sample and all the experiments were performed at a 3 kHz spinning rate. The CP match conditions were determined in a similar manner as for the ^{29}Si{^{1}H} CP experiments. ^{1}H and ^{15}N T_1 relaxation times were determined using the saturation recovery method. Recycle times were set to five times the ^{15}N T_1 value for the ^{15}N experiments and 1.25 times the ^{1}H T_1 value for the ^{15}N{^{1}H} CP experiments.

2.1.6.9 Data Analysis and Calculations

Analysis of ^{29}Si$\{^{19}$F$\}$ CP curves were performed using computer programs written as Mathematica[17] notebooks by Drs Andrew Lewis and Darren Brouwer of the University of British Columbia. Deconvolution of spectra and the analysis of the chemical shift tensors in Chapter 5 were performed using the DM2003[18] and the SIMPSON[19] programs respectively.

2.2 Microcrystal X-ray Diffraction

2.2.1 Introduction

Diffraction based techniques, such as X-ray diffraction, are well established as the most common methods for structural determination of solids.[20] Single-crystal X-ray diffraction is now commonly used to determine interatomic distances and bond angles for both organic and inorganic crystalline solids and can provide vital information about the structure and the properties of a new material. Synchrotron radiation is highly intense, polarised, and has a wide spectral distribution that can be easily tuned using appropriate monochromating devices. The high intensity and collimation of synchrotron radiation makes it ideal for studying microcrystals, in particular zeolites, as these have large volumes of empty space and do not scatter X-rays well.[21]

Synchrotron radiation is produced when electrons are accelerated to speeds approaching that of light around a circular ring called a synchrotron. A synchrotron consists of several main parts (Figure 2.16) and produces a full array of electromagnetic radiation wavelengths from high energy x-rays to infrared light. The electron source for a synchrotron is the electron gun that consists of a heated cathode, which produces electrons that are then accelerated by a linear accelerator or linac.
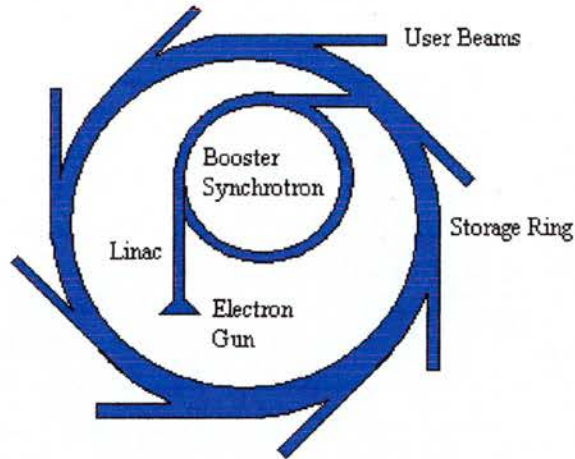
Figure 2.16 Diagrammatic representation of a synchrotron radiation source.

The electrons then undergo further acceleration by being fired around a small or booster ring under the influence of strong electric fields. Once the energy of the electrons is sufficient, they are injected in to a larger storage ring, where they circulate emitting synchrotron radiation. This loss of energy, as electromagnetic radiation, must be replenished to keep the electrons circulating and this is achieved by using klystrons. Large magnets of varying strengths are placed at intervals around the storage ring to keep the electrons travelling in a circular path. The electromagnetic radiation produced comes off the storage ring at tangents to the path of the travelling electrons, when the beam changes direction at a magnet. Further magnets called wigglers and undulators are used to produce additive series of X-rays and interference respectively by altering the electron beam orbit. Stations are placed around the ring where the beams come off, and the wavelength of the radiation can be specifically tuned using monochromators to obtain the highest quality data.

2.2.2 Crystal Symmetry

A crystalline structure is often described in terms of the simplest repeating unit, termed the unit cell, which is itself defined by three translations a, b, and c, and three angles α, β, and γ. There are seven basic shapes, with specific symmetries, of unit cell and these are listed in Table 2.2. A lattice point can be found at the origin of each unit cell and these lie on lattice planes, which are always parallel and equally spaced and cut the cell axes in fractional parts (e.g. $^1/_1$, $^1/_2$, $^1/_3$,... $^1/_n$). The reciprocal of the intercepts on the three axes (x, y, z) are known as the Miller indices (h, k, l) and these describe the three dimensional lattice planes. The spacing between adjacent lattice planes is designated d_{hkl}.

Crystal system	Lattice parameters	Lattice symmetry
Triclinic	$a \neq b \neq c$; $\alpha \neq \beta \neq \gamma$	$\bar{1}$
Monoclinic	$a \neq b \neq c$; $\alpha = \gamma = 90°$; $\beta \neq 90°$	2/m
Orthorhombic	$A \neq b \neq c$; $\alpha = \beta = \gamma = 90°$	Mmm
Tetragonal	$a = b \neq c$; $a = b = \gamma = 90°$	4/mmm
Rhombohedral	$A = b = c$; $\alpha = \beta = \gamma \neq 90°$	3m
Hexagonal	$a = b \neq c$; $\alpha = \beta = 90°$; $\gamma = 120°$	6/mmm
Cubic	$A = b = c$; $\alpha = \beta = \gamma = 90°$	m3m

Table 2.2 The seven crystal systems with their defining lattice parameters.

2.2.3 X-ray Production and Diffraction Theory

X-rays are usually produced by bombarding a metal target, often Cu or Mo, with a beam of high-energy electrons from a heated filament inside a vacuum tube. The effect of these high-energy electrons is to ionise electrons from the K-shell of the metal atoms, leading to the production of X-rays as the positive vacancy is filled from

the L or M levels. The filling of the vacancies from two different orbitals leads to the production of X-rays of two wavelengths. One of these X-ray beams is then selected, by the use of either a monochromator or a filter, and directed at the sample.

A large quantity of the X-rays directed at the sample pass straight through, however, some are scattered by their interaction with the atomic electrons and the degree of scattering is related to the quantity of atomic electrons and therefore the atomic number. This scattering by the atomic electrons can be described in terms of reflections from a set of lattice planes using the Bragg equation, which is universally used as the basis of X-ray diffraction geometry (Figure 2.17).[22]
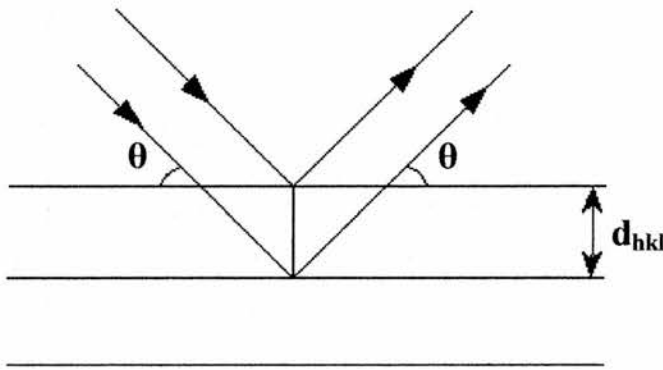
Figure 2.17 Bragg reflection from crystal planes with spacing d_{hkl}.

Bragg showed that the angle of incidence and reflection must be equal and that the incoming and outgoing beams must lie in the same plane. The diffraction of the beam by adjacent planes leads to interference that can either be destructive or constructive depending on the phase of the reflected beams. Bragg showed that for constructive interference of X-rays reflected by two adjacent planes:

path difference = $2d_{hkl}\sin\theta = n\lambda$ Equation 2.16

where λ is the wavelength of the X-rays and 2θ is the deviation of the beam.

The Bragg equation allows each reflection to be uniquely labelled with its three indices (h, k, l), and for the scattering angle (2θ) to be determined from the unit cell geometry. The scattering power f_x increases with an increasing number of atomic electrons, but also decreases with an increasing scattering angle (2θ).

The reflections of the X-ray beams can be collected as a diffraction pattern, which gives several pieces of information about the crystal structure. The first of these is the actual geometry of the diffraction pattern, which can be related to the lattice and unit cell geometry of the structure. The second piece of information is from the symmetry of the diffraction pattern, which relates to the crystal symmetry and the spacegroup of the material. The final piece of information is from the intensities of the spots that provide information, which can be used to find the positions of the atoms in the unit cell.

The diffraction pattern is created by Fourier transforming the electron density within the unit cell, in a process known as the forward Fourier transform, and is described by:

$$F_{(hkl)} = \sum_{j}^{N} f_j \exp(-8\pi^2 U_j \sin^2\theta / \lambda^2 \cdot \exp[2\pi i(hx_j + ky_j + lz_j)]$$ Equation 2.17

The value I is a complex number which contains information about the amplitude and the phase of each reflection. The value U is the isotropic displacement parameter and gives a measure of how much an atom is vibrating within the unit cell. Equation 2.16 relates the structure factor (F_j) for an atom j to the atomic coordinates x_j, y_j, z_j

and its scattering factor f_j. The summation is made over all the atoms (N) in the unit cell and produces a set of structure factors, consisting of both an amplitude $|F_{(hkl)}|$ and a phase $\varphi_{(hkl)}$.

To solve a crystal structure requires the location of the electron density from the diffraction pattern and this is achieved by a reverse Fourier transform, as show in Equation 2.18.

$$\rho_{(xyz)} = \frac{1}{V} \sum_{h,k,l} F_{(hkl)} \cdot \exp[-2\pi i(hx + ky + lz)]$$ Equation 2.18

The term 1/V, where V is the unit cell volume, has to be included in order to correct the units (as the structure factors have units of electrons, e, but electron density is in $e\text{Å}^{-3}$). The summation is performed over all values of h, k, and l, but in practice the reflections are usually, only measured to a maximum value as above this they become too weak. The value $F_{(000)}$ must, however, be included as this is equal to the total number of electrons in one unit cell and ensures that the correct electron density values are obtained. The diffraction experiment only gives the amplitude $F_{(hkl)}$ and not the phases of each reflection and it is, therefore, not possible to directly obtain the electron density. This is known as the phase problem.

Several methods exist for solving the phase problem and this includes the direct methods. Direct methods attempts to determine the structure factor phases by purely mathematical means. This involves selecting the most important reflections, which are those that contribute most to the Fourier transform, working out the probable relationships among their phases and then testing different potential phases to see how well the probability relationships are satisfied. Once the most promising combinations have been found, Fourier transforms can be calculated from the observed amplitudes

and the trial phases are examined for recognisable molecular fragments. This generally allows most of the non-hydrogen atoms to be located for a material composed of atoms with a similar scattering power. Direct methods do not work well for a structure containing heavy atoms; instead the Patterson synthesis technique would need to be used. The model produced by the direct methods can then be used to refine the structure using a least-squares technique.

The model structure is refined to locate the remaining atoms and to vary the atomic parameters systematically to provide the best possible agreement between the observed structure factor amplitudes ($|F_{hkl}|_o$) and those calculated by Fourier transform ($|F_{hkl}|_c$). Least-squares refinement of the amplitudes defines the 'best-fit' of the two data sets when a minimum in the function shown in Equation 2.19 is found.

$$\sum w_{hkl}(|\,F_{hkl}\,|_o^2 - |\,F_{hkl}\,|_c^2)^2 \qquad\qquad \text{Equation 2.19}$$

Each reflection is weighted according to its reliability, which usually depends on standard uncertainties (w_{hkl}) on F^2, as defined by the equation:

$$w_{hkl} = \frac{1}{\sigma^2(|\,F_{hkl}\,|_c^2)^2} \qquad\qquad \text{Equation 2.20}$$

There are several structural parameters that are refined, and these include; the atomic coordinates (x, y, z) for every atom, the atomic displacement parameters (U) – one U value per atom for an isotropic model or six U values for an anisotropic model, an overall scale factor, and sometimes the site occupancy. It is always best if there are many more observations than refined parameters for the least-squares refinement to be accurate. The least-squares calculation is usually repeated several times in order to

produce a refinement that is stable and that has converged to a minimum. The progress of the refinement is monitored by the value of the minimisation equation in order to ensure that the best possible fit is achieved. This fit is often reported as the *R* factor, and can take two forms, a weighted and unweighted function. The unweighted function has been used for many years and is based on the amplitudes of the reflections:

$$R = \frac{\sum \left\| F_{hkl} \right|_o - \left| F_{hkl} \right|_c \right|}{\sum \left| F_{hkl} \right|_o}$$

Equation 2.21

However, the weighted version (wR_2) is most closely related to the minimisation and incorporates the reflection weights:

$$wR_2 = \frac{\sum w(\left| F_{hkl} \right|_o^2 - \left| F_{hkl} \right|_c^2)^2}{\sum \left| F_{hkl} \right|_o}$$

Equation 2.22

A 'good' structure is often considered to have a wR_2 value of < 0.15 and a R value of < 0.05, although an incorrect structure can also meet these criteria, so any result must be closely scrutinised.

2.2.4 Experimental Details

All of the crystals analysed in this work were too small for a conventional laboratory X-ray diffractometer and this led to all the experiments being performed at the high-flux single crystal diffraction station 9.8 at the CCLRC Daresbury Laboratory Synchrotron Radiation Source, Cheshire, UK.[23] The data were collected at low temperature (150 K) using a Bruker AXS SMART CCD area-detector diffractometer with X-rays of wavelength between 0.68 and 0.70 Å. The wavelength of the X-rays

was selected by a horizontally focussing silicon (111) monochromator and focussed

vertically using a cylindrically bent palladium-coated zerodur mirror. The data sets

covered more than a hemisphere of reciprocal space with several series of exposures,

each series with a different crystal orientation and each exposure taken over 0.2°

rotation. Corrections were made for the decay of the synchrotron beam intensity as

part of the standard inter-frame scaling procedures. The refinements of the data were

carried out using a least-squares method, using the programs SHELX-97[24] and

WINGX.[25] The computer programs PLATON and SQUEEZE[26] were used to examine

for missing / additional symmetry and for removing unrefined electron density from

the model of the zeolite pores respectively.

2.3 Non-Linear Optics (SHG)

2.3.1 Introduction to Non-linear Optics

When a conventional light source is shone on a material, the optical behaviour is

classed as being linear as the intensity of the light radiation is less than strength of the

atomic fields within the material. The advent of lasers, which have a high degree of

coherence, has led to sources of light which have intensities of equal to or greater than

the atomic field strengths of materials, this gives a non-linear behaviour.[27] Non-

linear behaviour can be illustrated by considering the example of a stretched spring.

In the case of a linear process the spring obeys Hooke's law, which states that the

force (F) exerted on a spring is proportional to its extension (x) or:

$$F = kx \quad \text{where } k \text{ is the spring constant} \qquad \text{Equation 2.23}$$

A spring is unlikely to keep stretching indefinitely, and as the force on the spring is increased a point will be reached when Hooke's law is no longer obeyed and instead some relationship with additional powers of x will result, as shown below:

$$F = k_1x + k_2x^2 + k_3x^3....$$

Equation 2.24

This behaviour is non-linear and it can be shown that plucking the non-linear spring will cause it to oscillate at frequencies ω_0, $2\omega_0$, $3\omega_0$... compared to the single frequency ω_0 for the linear spring. An almost identical analysis has been deduced for optical non-linearity, where the bonds between the atoms are likened to springs. In the optical case a non-linear medium is needed to act as a catalyst for the non-linear process, this is often a crystal, a powder or a surface. A highly coherent light source is needed to generate a measurable non-linear optical effect, as the photons interacting with the medium must have sufficient energy to perturb the atomic fields. The interaction of the photons with the medium can be illustrated in an energy level diagram as shown in Figure 2.18.
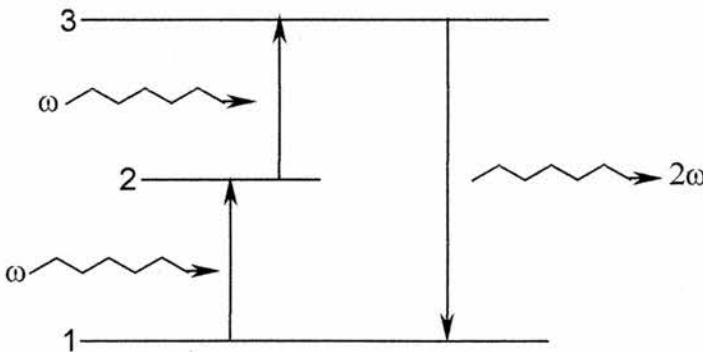
Figure 2.18 Energy level diagram for second harmonic generation

The energy level diagram for second harmonic generation shows that an initial photon of frequency ω is absorbed leading to the transition of an electron from state 1

to 2. A second photon of frequency ω is subsequently absorbed leading to the transition of an electron from state 2 to 3. The high-energy electron in state 3 now returns to the ground state 1 by releasing a photon of frequency 2ω and the process begins again.

Franklin *et al.*[28] in 1961 were the first to observe the non-linear optical behaviour in the form of second harmonic generation. Their experiment consisted of shining a recently invented ruby laser through a quartz crystal and observing that green light was produced. This phenomenon is known as second harmonic generation (SHG) and is dependent on the polarizability (P) of the material, which is itself a function of the applied field strength (E) and the dielectric (or linear) susceptibility (χ) of a material as shown below:

$$P = \chi^{(1)}E \ \text{ or } \ P = \chi^{(1)}E + \chi^{(2)}E^2 + \chi^{(3)}E^3 + ...$$

<div align="right">Equation 2.25</div>

$\chi^{(1)}$, $\chi^{(2)}$ and $\chi^{(3)}$ are the first order (linear), second order (non-linear) and third order (non-linear) susceptibility tensors, which relate the electric field to the polarization as a function of spatial direction.[29]

Equation 2.25 has both a quadratic and a cubic term, the cubic term, however, is very small in comparison to the quadratic term and can generally be ignored, giving:

$$P = \chi^{(1)}E + \chi^{(2)}E^2$$

<div align="right">Equation 2.26</div>

and as $E = E_0 \cos(\omega t)$, where ω is the frequency of the incident radiation, this gives:

$$P = \chi^{(1)}E_0 \cos(\omega t) + \chi^{(2)}(E_0 \cos(\omega t))^2$$

<div align="right">Equation 2.27</div>

And therefore:

$$P = \frac{1}{2} \chi^{(2)} E_{0(2)} + \chi^{(1)} E_0 \cos(\omega\, t) + \frac{1}{2} \chi^{(2)} E_{0(2)} \cos(2\omega\, t)$$ Equation 2.28

Equation 2.28 now contains a component of double frequency $(2\omega t)$, which corresponds to the production of visible green light from an initial infrared laser light.

For second harmonic generation to occur, certain criteria must be met, the main one is that the crystal does not possess inversion symmetry, that is, the crystal structure does not remain the same on swapping the coordinate r by –r. Centrosymmetric crystals are ones that possess inversion symmetry and exhibit extremely weak if any second harmonic generation. Crystals that lack inversion symmetry are termed noncentrosymmetric and give strong second harmonic generation. The presence or lack of inversion symmetry are the zero and non-zero components of the nonlinear susceptibility tensor (χ). It can be seen from Equation 2.28 that if $\chi^{(2)}$ is zero then no second harmonic generation will be observed, as is the case for centrosymmetric crystals.

X-ray diffraction techniques are well established as the main source of crystal symmetry information, however, they do have one major drawback when it comes to samples without a centre of symmetry due to them breaking Friedel's law. Friedel's law states that a centre of symmetry is automatically introduced in to diffraction experiments and can be derived from the expression for the structure factor:

$$|F_{hkl}| = (A_{hkl}^2 + B_{hkl}^2)^{1/2} \text{ and } F_{hkl} = A_{hkl} + iB_{hkl}$$

where
$$A_{hkl} = \sum f_j \cos 2\pi (hx_j + ky_j + lz_j) \text{ and}$$

$$B_{hkl} = \sum f_j \sin 2\pi (hx_j + ky_j + lz_j)$$

it follows that $A_{hkl} = A_{\overline{hkl}}$ and $B_{hkl} = -B_{\overline{hkl}}$ and since $I = A^2 + B^2$,

then $I_{hkl} = I_{\overline{hkl}}$, which is Friedel's law.

The problem in diffraction, is determining whether a centre of symmetry is present or not, despite Friedel's law. This can be done by using X-rays having energies close to an absorption edge of an atom, which results in anomalous dispersion.[21] This anomalous dispersion produces a phase lag between the anomalous scatterer and the rest of the atoms. In a centrosymmetric structure, the dispersion simply changes the magnitude of that atom's contribution. However, in a noncentrosymmetric structure, the relative magnitudes of the reflection intensity of pairs of reflections hkl and $\overline{hkl}$ are changed by the dispersion and therefore it is possible to determine if Friedel's law is violated. The amount of anomalous dispersion from a sample, such as a zeolite, is very small as all the atoms have similar scattering factors and, this makes it much harder to determine if a crystal is noncentrosymmetric. Non-linear optics can often provide a relatively simple test for the presence of a noncentrosymmetric crystal or noncentrosymmetric molecules within a centrosymmetric crystal.
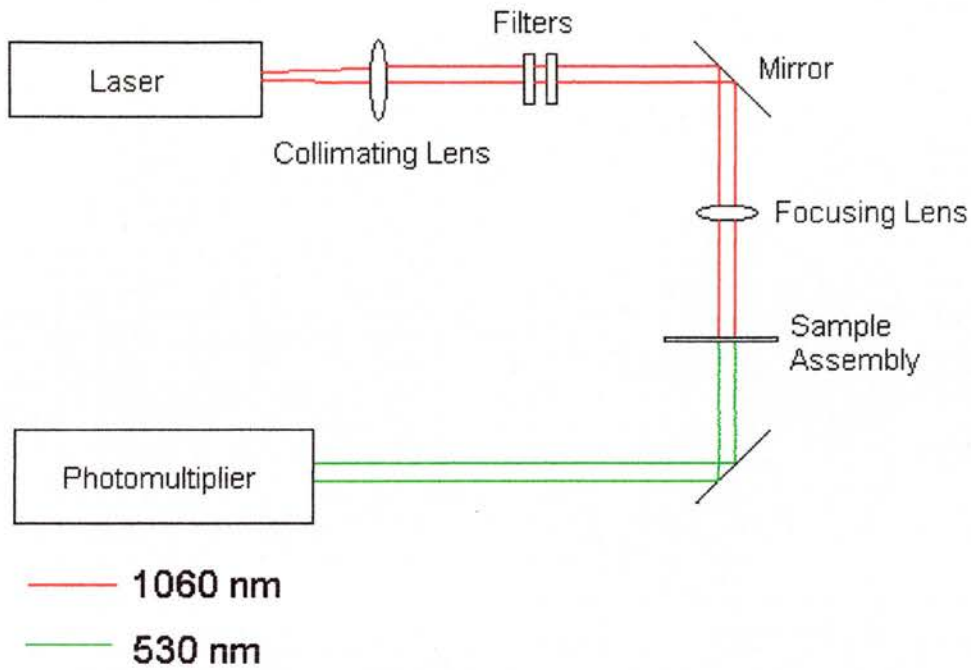
Figure 2.19 Diagrammatic representation of SHG testing equipment.

Kurtz and Perry[30] carried out the first measurements of second harmonic generation

(SHG) in powdered samples and since then, many other researchers have carried out

similar work.[31] The instruments used are all based around the initial design by Kurtz

and Perry and can be seen in Figure 2.19.

2.3.2 Experimental Details

All of the non-linear optics work was carried out using a Nd: YAG laser with a

wavelength of 1060 nm. Any light of doubled frequency produced by

noncentrosymmetric samples was detected by a photomultiplier and by the presence

of a visible green light ($\lambda = 530$ nm).

The samples were prepared by grinding them to a fine powder using a pestle and

mortar and then examining the powder under an optical microscope to ensure that all

the samples had similar particle sizes. The samples were then mounted between two very thin sheets of Mylar, using a small quantity of silicone grease to hold the samples in place. The Mylar sheets were then fixed between two microscope slides and clamped in the path of the laser beam. A reference sample of potassium titanyl phosphate (KTP) was used to ensure that a significant second harmonic signal was seen and a sample of sodium chloride was used as a blank. Before any measurements were recorded, another blank sample consisting of just the Mylar sheets, silicone grease and the microscope slides was used to ensure that no SHG signal was observed.

Many of the samples investigated did not produce a strong enough second harmonic signal to be quantified using the photomultiplier. This was partly due to the small particles that scattered much of the second harmonic signal and due to the experimental set-up, which did not allow for the collection and focussing of the scattered light. Therefore, for many of the samples it is only possible to give a qualitative result for the non-linear optical experiments based on the presence or absence of a second harmonic signal.

2.4 Other Experimental Techniques

2.4.1 Powder X-ray Diffraction

Powder X-ray diffraction patterns were collected for phase identification purposes only on a STOE STADIP diffractometer using monochromated Cu $K_{\alpha 1}$ radiation (λ = 1.54 Å). Samples were mounted with silicone grease between Mylar sheets and placed within diffraction discs, which enabled the sample to be rotated, in order to reduce any preferred orientation effects.

2.4.2 Solution State NMR

Solution state NMR experiments were performed on a Bruker Avance NMR spectrometer operating at 300 MHz for ^{1}H and 75.44 MHz for ^{13}C. All the organic structure-directing agents were completely dissolved in either D_2O or $CDCl_3$ with tetramethylsilane (TMS) added, as a primary standard.

2.4.3 CHN Elemental Analysis

CHN analysis was performed on all of the organic structure directing agents to determine the C: H: N ratios and hence the purity of the samples. The analysis was performed on a Carlo Erba 1106 CHN elemental analyser.

2.5 References for Chapter 2

1. C. A. Fyfe, *Nature*, 1987, **325**, 194.

2. H. J. Dyson and P. E. Wright, *Chem. Rev.*, 2004, **104**, 3607.

3. C. A. Fyfe, D. H. Brouwer, A. R. Lewis, L. A. Villaescusa and R. E. Morris, *J. Am. Chem. Soc.*, 2002, **124**, 7770.

4. C. A. Fyfe, *Solid State NMR for Chemists*, C.F.C. Press, 1984.

5. C. A. Fyfe, J. H. O'brien and H. Strobl, *Nature*, 1987, **326**, 281.

6. M. J. Duer, *Introduction to Solid State NMR Spectroscopy*, Blackwell Publishing, Oxford, 2004.

7. M. E. Smith, *Private Communication*, 2004.

8. C. A. Fyfe, K. T. Mueller, H. Grondey and K. C. Wongmoon, *J. Phys. Chem.*, 1993, **97**, 13484.

9. M. E. Smith and E. R. H. Van Eck, *Prog. Nucl. Magn. Reson. Spectrosc.*, 1999, **34**, 159.

10. S. J. Waugh, L. M. Huber and U. Haeberlen, *Phys. Rev. Lett.*, 1968, **20**, 180.

11. W. K. Rhim, D. D. Elleman and R. W. Vaughn, *J. Chem. Phys.*, 1973, **59**, 3740.

12. M. Mehring, *Principles of High-Resolution NMR in Solids, 2nd Ed.*, Springer-Verlag, Berlin, Germany, 1983.

13. S. R. Hartmann and E. L. Hahn, *Phys. Rev. A*, 1962, **128**, 2042.

14. G. Neue and C. Dybowski, *Solid State Nucl. Magn. Reson.*, 1997, **7**, 333.

15. C. W. Lentz, *Inorg. Chem.*, 1964, 574.

16. P. Caullet, J. L. Guth, J. Hazm, J. M. Lamblin and H. Gies, *Eur. J. Solid State Inorg. Chem.*, 1991, **28**, 345.

17. S. Wolfram, Mathematica, A System for Doing Mathematics by Computer , Wolfram Media, Champaign, IL, ver. 3.0.

18. D. Massiot, F. Fayon, M. Capron, I. King, S. Le Calve, B. Alonso, J. O. Durand, B. Bujoli, Z. H. Gan and G. Hoatson, *Magn. Reson. Chem.*, 2002, **40**, 70.

19. M. Bak, J. T. Rasmussen and N. C. Nielsen, *J. Magn. Reson.*, 2000, **147**, 296.

20. A. K. Cheetham and P. Day, *Solid State Chemistry Techniques*, Clarendon Press, Oxford, 1987.

21. G. H. Stout and L. H. Jensen, *X-Ray Structure Determination - A Practical Guide*, John

Wiley & Sons, New York, 1989.

22. L. V. Azaroff, *Elements of X-Ray Crystallography*, McGraw-Hill, New York, 1968.

23. R. J. Cernik, W. Clegg, C. R. A. Catlow, G. Bushnell-Wye, J. V. Flaherty, G. N. Greaves, I. Burrows, D. J. Taylor, S. J. Teat and M. Hamichi, *J. Synchrotron Rad.*, 1997, **4**, 279.

24. Siemens, *SHELXTL. Structure Determination Software*, Siemens Analytical X-ray Instruments Inc., Madison, Wisconsin, USA, 1995.

25. L. J. Farrugia, *J. Appl. Crystallogr.*, 1999, **32**, 837.

26. A. L. Spek, *PLATON. A Multipurpose Crystallographic Tool*, Utrecht University, Utrecht, The Netherlands , 1999.

27. B. B. Laud, *Lasers and Non-Linear Optics*, Wiley Eastern Ltd, New Delhi, India, 1985.

28. D. H. McMahon and A. R. Franklin, *Appl. Phys. Lett.*, 1965, **6**, 1965.

29. I. S. Ruddock, *Eur. J. Phys.*, 1994.

30. S. K. Kurtz and T. T. Perry, *J. Appl. Phys.*, 1968, **39**, 3798.

31. J. P. Dougherty and S. K. Kurtz, *J. Appl. Crystallogr.*, 1976, **9**, 145.

3.0 Synthesis of Structure Directing Agents and Pure Silica Zeolites

3.1 Synthesis and Characterisation of Structure Directing Agents

3.1.1 Introduction and Aims

The possible roles of the structure directing agents during a zeolite synthesis were described in Chapter 1. The SDAs used to synthesise pure silica zeolites are usually quartenary ammonium ions and often have to be in the form of the hydroxide salt. This is because many pure silica zeolites can only be prepared from tetraethylorthosilicate (TEOS), which needs hydrolysing by OH⁻ ions, and is described in more detail in Chapter 3.2. The constant search for new zeolites has meant that new and more complex organic molecules have been investigated as SDAs. This has led to the synthesis of many new pure silica zeolites over the last 10 years such as ITQ-4[1] and ITQ-9.[2]

The aim of this work was to synthesise several SDAs to allow the preparation of samples of pure silica zeolites for further structural elucidation. Many of these quartenary ammonium salts have been previously shown to act as SDAs for the synthesis of pure silica zeolites. In particular *N*-Benzylquinuclidinium ions are well established as SDAs for the synthesis of the zeolite ITQ-4.[3] A further aim, therefore, of this work was to functionalise the *N*-benzylquinuclidinium using simple organic reactions, so that these new molecules could be investigated for use in zeolite syntheses.

3.1.2 Experimental Details

3.1.2.1 N-Benzylquinuclidinium chloride

To a solution of benzyl chloride (3.32 g, 26.25 mmol) in dichloromethane (50 ml) was added quinuclidine (2.52 g, 22.70 mmol) and the mixture stirred at room temperature for 12 hours. The product was then extracted by pouring the solution into an excess of ethyl acetate (350 ml) and filtering off the precipitate produced, which was then washed with more ethyl acetate and yielded a white solid. The white solid was then recrystallised from hot ethyl acetate and ethanol to give white crystals (5.36 g, 98.0 %): Mpt 246-248 °C (decomposes); ^{1}H NMR (300 MHz, D_2O) δ 1.83 (6H, m, $N(CH_2)_3$ –(CH_2)$_3$), 2.06 (1H, m, $(CH_2)_3$-C$\underline{H}$), 3.33 (6H, t, N-($C\underline{H}_2$)$_3$), 4.22 (2H, s, N-$C\underline{H}_2$-Ar), 7.37-7.51 (5H, m, Ar-$\underline{H}$); ^{13}C NMR (300 MHz, D_2O) δ 19.55 ((CH_2)$_3$-$\underline{C}$H), 23.40 (($\underline{C}H_2$)$_3$-CH), 54.48 (N-($\underline{C}H_2$)$_3$), 67.87 (N-$\underline{C}H_2$-Ar), 126.89 (CH_2-Ar$\underline{C}$), 129.03 (Ar$\underline{C}$ o-CH_2), 130.46 (Ar$\underline{C}$ p-CH_2), 132.90 (Ar$\underline{C}$ m-CH_2); CHN analysis calcd. 70.72 %C, 8.48 %H and 5.89 %N found 65.63 %C, 9.14 %H and 5.32 %N.
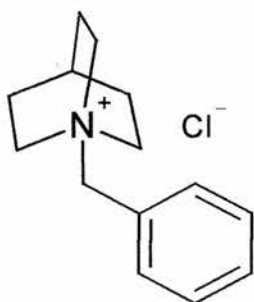
Figure 3.1 *N*-benzylquinuclidinium Chloride

3.1.2.2 Tert-Butyltrimethylammonium iodide (tBTMA)

Tert-butylamine (10.43g, 0.14 mol) was added to toluene (100 ml) and the solution cooled to below −40 °C. Methyl iodide (60.09 g, 0.42 mol) was then added dropwise whilst continuously stirring. The mixture was left stirring at room temperature for one week before filtering the solid produced, which was then washed in a Soxhlet apparatus with dichloromethane to give a white crystalline solid (30.41g, 91.49 %): Mpt 240 − 241 °C (decomposes); ^{1}H NMR (300 MHz, D$_2$O) δ 1.35 (9H, s, C-(C$\underline{H}_3$)$_3$), 2.95 (9H, s, N-(C$\underline{H}_3$)$_3$); ^{13}C NMR (300 MHz, D$_2$O) δ 23.41 (C-($\underline{C}H_3$)$_3$), 49.49 (N-($\underline{C}H_3$)$_3$), 71.10 (N-$\underline{C}$); CHN analysis calcd. 34.58 %C, 7.46 %H, 5.76 %N found 34.31 %C, 7.32 %H, 5.44 %N.
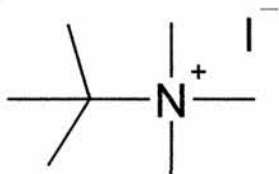
Figure 3.2 t-Butyltrimethylammonium iodide

3.1.2.3 1,3,3,6,6-Pentamethyl-6-azabicyclo[3.2.1]octane iodide (DMABO)

To a solution of 1,3,3-trimethyl-6-azabicyclo[3.2.1]octane (10.01 g, 65.31 mmol) in methanol (100 ml) was added potassium carbonate (13.5 g, 97.67 mmol) and the mixture cooled to −78 °C. Methyl iodide (20.60 g, 0.14 mol) was then added dropwise to the solution, whilst being constantly stirred. The reaction mixture was allowed to warm to room temperature, before being refluxed for 48 hours. The methanol was then removed under reduced pressure and the solids triturated with dichloromethane and filtered to remove the potassium carbonate. The

dichloromethane was then removed under reduced pressure to give a pale yellow

solid, which was recrystallised from warm isopropanol and just enough methanol to

dissolve the product giving pale yellow crystals that where then washed with acetone

yielding white crystals (15.89 g, 78.7 %): Mpt 188-189 °C; ^{1}H NMR (300 MHz,

D_2O) δ 1.05 (3H, s, C-C$\underline{H}_3$), 1.10 (3H, s, C-C$\underline{H}_3$), 1.20 (3H, s, C-C$\underline{H}_3$), 1.65 (2H, m,

C$\underline{H}_2$), 1.82 (2H, m, C$\underline{H}_2$), 2.31 (1H, m, C$\underline{H}$), 3.15 (6H, s, N-(C$\underline{H}_3$)$_3$), 3.31 (2H, m,

C$\underline{H}_2$); ^{13}C NMR (300 MHz, D_2O) δ 25.06 ($\underline{C}H_3$-C), 26.64 (CH$_3$-$\underline{C}$), 33.41 (N-$\underline{C}H_3$),

37.88 (N-$\underline{C}H_3$), 39.22 (CH-$\underline{C}H_2$-C), 40.62 (CH-CH$_2$-$\underline{C}$), 49.91 (C-$\underline{C}H_3$), 51.63 (CH-

$\underline{C}H_2$-C), 57.21 (C-$\underline{C}H_3$), 73.88 (N-$\underline{C}H_2$-C), 75.45 (N-$\underline{C}H$-(CH$_2$)$_2$); CHN analysis

calcd. 46.61 %C, 7.82 %H and 4.53 %N found 46.74 %C, 8.21 %H and 4.43 %N.
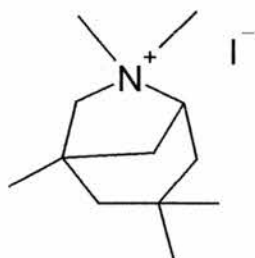
Figure 3.3 1,3,3,6,6-Pentamethyl-6-azabicyclo[3.2.1]octane iodide

3.1.2.4 N-benzyl-1,4-diazabicyclo[2.2.2]octane chloride (BzDABCO)

To a solution of an excess of benzyl chloride (15 g, 0.12 mol) in chloroform (50

ml) was slowly added 1,4-diazabicyclo[2.2.2]octane (10 g, 89.15 mmol) and the

mixture stirred at room temperature for 24 hours. The white solid produced was then

filtered and washed with ethyl acetate before being recrystallised from hot isopropanol

and ethanol to give white crystals (21.50 g): Mpt 242 – 244 °C; ^{1}H NMR (300 MHz,

D_2O) δ 3.85 (12H, s, N-C$\underline{H}_2$), 4.60 (2H, s, N-C$\underline{H}_2$-Ar), 7.48 (5H, m, Ar-H); ^{13}C NMR

(300 MHz, D_2O) δ 50.81 (N-$\underline{C}H_2$), 68.91 (N-$\underline{C}H_2$-Ar), 129.69 ($\underline{A}r$), 131.65 ($\underline{A}r$),

132.95 (Ar); CHN analysis calcd. 65.40 %C, 8.02 %H, 11.73 %N found 62.72 %C, 7.67 %H, 7.43 %N.
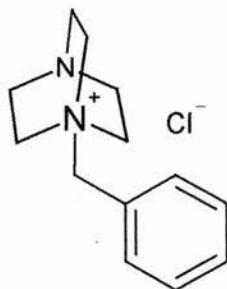
Figure 3.4 *N*-benzyl-1,4-diazabicyclo[2.2.2]octane chloride

3.1.2.5 *N,N-diethyl-2,6-dimethylpiperidinium iodide (DECDMP)*

Cis-2,6-dimethylpiperidine (20 g, 0.18 mol) was added to a mixture of potassium hydrogen carbonate (26.52 g, 0.27 mol) in methanol (250 ml). The mixture was then stirred whilst ethyl iodide (82.63 g, 0.54 mol) was added dropwise over 30 minutes. The resulting mixture was refluxed for 72 hours and then the methanol removed and the resulting solids mixed with chloroform and filtered to remove the insoluble material. The chloroform was then stripped off under reduced pressure and the solid produced was recrystallised from hot isopropanol and ethanol to give white crystals (45.3 g, 86.3 %): Mpt 297 – 298 °C (decomposes); ^{1}H NMR (300 MHz, D$_2$O) δ 1.25 (6H, d, CH-C$\underline{H}_3$), 1.28 (6H, d, NCH$_2$-C$\underline{H}_3$), 1.52 (2H, m, 2C$\underline{H}$ax), 1.74 (3H, m, 3C$\underline{H}$eq), 1.95 (1H, m, C$\underline{H}$ax), 3.44 (4H, m, NC$\underline{H}_2$-CH$_3$), 3.63 (2H, m, CH$_3$C-$\underline{H}$); ^{13}C NMR (300 MHz, D$_2$O) δ 10.37 (CH$_2$-$\underline{C}$H$_2$-CH$_2$), 15.87 ($\underline{C}$H$_2$-CH$_2$-CH$_2$), 17.75 (CH$_2$-CH$_2$-$\underline{C}$H$_2$), 21.71 (CH-$\underline{C}$H$_3$), 22.01 (CH-$\underline{C}$H$_3$), 27.22 (N-CH$_2$-$\underline{C}$H$_3$), 32.09 (N-CH$_2$-$\underline{C}$H$_3$), 46.40 (N-$\underline{C}$H-CH$_2$), 48.97 (N-$\underline{C}$H-CH$_2$), 57.91 (N-$\underline{C}$H$_2$-CH$_3$), 65.49 (N-$\underline{C}$H$_2$-

CH$_3$); CHN analysis calcd. 44.45 %C, 8.14 %H, 4.71 %N found 43.18 %C, 8.25 %H, 4.76 %N.
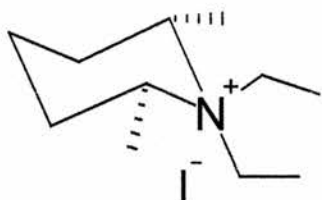
Figure 3.5 *N,N*-diethyl-2,6-dimethylpiperidinium iodide

3.1.2.6 Dimethylazoniaspiro[4.5]decane iodide (DMASD)

Cis-2,6-dimethylpiperidine (15 g, 0.13 mol) and potassium hydrogen carbonate (19.9 g, 0.19 mol) were added to methanol (200 ml) and the resultant mixture stirred. 1,4-diiodobutane (37.0 g, 0.14 mol) was then added dropwise before being refluxed for 48 hours. The methanol was then removed under reduced pressure and the solids formed were added to dichloromethane (50 ml), which was then filtered to remove any of the insoluble material. The dichloromethane was then removed and the product recrystallised from hot isopropanol and methanol to give pale yellow crystals 32.4 g (83.0 %): Mpt 288 – 289 °C (decomposes); ^{1}H NMR (300 MHz, D$_2$O) δ 1.28 (6H, d, CH-C$\underline{H}$$_3$), 1.54 (2H, m, NCH$_2$-C$\underline{H}$$_2$), 1.63 (2H, m, NCH$_2$-C$\underline{H}$$_2$), 1.75 (2H, m, CH$_2$-C$\underline{H}$$_2$-CH$_2$), 1.98 (4H, m, C$\underline{H}$$_2$-CH$_2$-C$\underline{H}$$_2$), 3.25 (2H, t, N-C$\underline{H}$$_2$-CH$_2$), 3.5 (2H, m, N-C$\underline{H}$), 3.62 (2H, t, N-C$\underline{H}$$_2$-CH$_2$); ^{13}C NMR (300 MHz, D$_2$O) δ 16.38 (N-(CH-$\underline{C}$H$_3$)$_2$), 22.03 (CH$_2$-$\underline{C}$H$_2$-CH$_2$), 25.20 ($\underline{C}$H$_2$-CH$_2$-CH$_2$), 26.55 (CH$_2$-CH$_2$-$\underline{C}$H$_2$), 29.62 (N-CH$_2$-($\underline{C}$H$_2$)$_2$-CH$_2$), 48.71 (N-$\underline{C}$H$_2$-(CH$_2$)$_2$-CH$_2$), 62.82 (N-CH$_2$-(CH$_2$)$_2$-$\underline{C}$H$_2$), 70.70 (N-($\underline{C}$H-CH$_3$)$_2$); CHN analysis calcd. 44.76 %C, 7.51 %H and 4.74 %N found 44.90 %C, 7.88 %H and 4.54 %N.
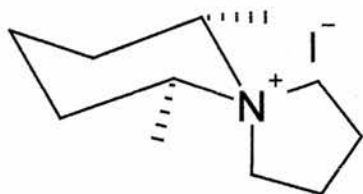
Figure 3.6 Dimethylazoniaspiro[4.5]decane iodide

3.1.2.7 4-Fluorobenzylquinuclidinium chloride

4-fluorobenzyl chloride (10 g, 69.17 mmol) was added to chloroform (100 ml) and the resulting solution stirred. Quinuclidine (7.69 g, 69.17 mmol) was then slowly added to the stirred solution over a period of 5 minutes. The solution was then stirred for a further 3 hours at room temperature before being concentrated under reduced pressure and poured into ethyl acetate (150 ml) to give a white precipitate. The solid was recovered by filtration and recrystallised from hot ethyl acetate and methanol to give white crystals (17.0 g, 96.1 %): Mpt 271 – 273 °C; ^{1}H NMR (300 MHz, D_2O) δ 1.85 (6H, t, $N(CH_2)_3$ –$(CH_2)_3$), 2.07 (1H, m, $(CH_2)_3$-CH), 3.30 (6H, t, N-$(CH_2)_3$), 4.22 (2H, s, N-CH_2-Ar), 7.13 (2H, d, Ar-H *m*-F), 7.45 (2H, d, *o*-F); ^{13}C NMR (300 MHz, D_2O) δ 19.96 (CH_2-CH), 23.79 (NCH_2-CH_2), 54.78 (N-$(CH_2)_3$), 67.30 (N-CH_2-Ar), 116.35 (Ar-C *o*-F), 123.38 (ArC-CH_2), 135.40 (Ar-C *m*-F), 165.67 (F-ArC); CHN analysis calcd. 65.75 %C, 7.49 %H, 5.48 %N found 65.52 %C, 7.79 %H, 5.48 %N.
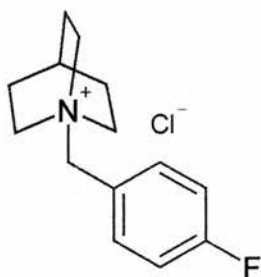
Figure 3.7 4-Fluorobenzylquinuclidinium chloride

3.1.2.8 4-Methoxybenzylquinuclidinium chloride

Quinuclidine (7.1 g, 63.85 mmol) was slowly added to a stirred solution of 4-methoxybenzyl chloride (10 g, 63.85 mmol) in dichloromethane (100 ml). The resulting solution was stirred for a further 3 hours before being concentrated under reduced pressure and poured into ethyl acetate (150 ml) to give a white precipitate. The solid was then recovered by filtration and recrystallised from hot ethyl acetate and methanol to give fine white crystals (16.2 g, 94.8 %): Mpt 217 – 219 °C; ^{1}H NMR (300 MHz, D_2O) δ 1.85 (6H, m, N(CH$_2$)$_3$ –(C$\underline{H}_2$)$_3$), 2.07 (1H, m, (CH$_2$)$_3$-C$\underline{H}$), 3.30 (6H, t, N-(C$\underline{H}_2$)$_3$), 3.78 (3H, s, O-CH$_3$), 4.20 (2H, s, N-C$\underline{H}_2$-Ar), 7.01 (2H, d, Ar-H *m*-OMe), 7.35 (2H, d, Ar-H *o*-OMe); ^{13}C NMR (300 MHz, D_2O) δ 19.64 ((CH$_2$)$_3$-$\underline{C}$H), 23.42 (($\underline{C}$H$_2$)$_3$-CH), 54.27 (N-($\underline{C}$H$_2$)$_3$), 55.45 (O-$\underline{C}$H$_3$), 67.44 (N-$\underline{C}$H$_2$-Ar), 114.39 (Ar$\underline{C}$ *m*-OMe), 119.38 (Ar$\underline{C}$-CH$_2$), 134.40 (Ar$\underline{C}$ *o*-OMe), 160.43 (Ar$\underline{C}$-OMe); CHN analysis calcd. 67.27 %C, 8.28 %H, 5.23 %N found 66.79 %C, 8.62 %H, 5.17 %N.
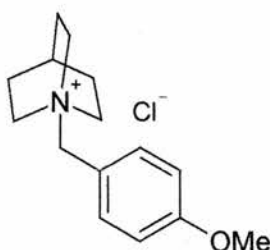
Figure 3.8 4-Methoxybenzylquinuclidinum chloride

3.1.2.9 4-Nitrobenzylquinuclidinium bromide

To a solution of 4-nitrobenzyl bromide (5.85 g, 27.08 mmol) in chloroform (50 ml) was slowly added quinuclidine (3.0 g, 26.98 mmol) whilst under constant stirring. The solution was stirred for a further 5 hours before being concentrated under reduced

pressure and added to ethyl acetate (150 ml) to give a yellow precipitate. The yellow

solid was then recovered by filtration and recrystallised from hot ethyl acetate and just

enough ethanol for the solids to dissolve, giving yellow crystals (7.05 g, 80.04%):

Mpt 246 –248 °C (decomposes); ^{1}H NMR (300 MHz, D$_2$O) δ 1.96 (6H, m, N(CH$_2$)$_3$ –

(C$\underline{H}_2$)$_3$), 2.05 (1H, m, (CH$_2$)$_3$-C$\underline{H}$), 3.20 (6H, t, N-(C$\underline{H}_2$)$_3$), 4.40 (2H, s, N-C$\underline{H}_2$-Ar),

7.64 (2H, d, Ar-$\underline{H}$ *m*-NO$_2$), 8.20 (2H, d, Ar-$\underline{H}$ *o*-NO$_2$); ^{13}C NMR (300 MHz, D$_2$O) δ

19.75 (CH$_2$)$_3$-$\underline{C}$H), 23.78 (($\underline{C}$H$_2$)$_3$-CH), 55.26 (N-($\underline{C}$H$_2$)$_3$), 66.82 (N-$\underline{C}$H$_2$-Ar), 124.35

(Ar$\underline{C}$ *m*-NO$_2$), 134.31 (Ar$\underline{C}$-CH$_2$), 134.55 (Ar$\underline{C}$ *o*-NO$_2$), 149.95 (Ar$\underline{C}$-NO$_2$); CHN

analysis calcd. 51.39 %C, 5.85 %H, 8.56 %N found 50.63 %C, 5.85 %H, 8.24 %N.
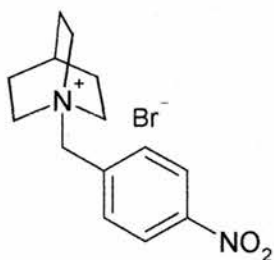
Figure 3.9 4-Nitrobenzylquinuclidinium bromide

3.1.2.10 N-ethyl,N-methyl-2,6-dimethylpiperidinium iodide (EMDMP)

Cis-2,6-dimethylpiperidine (14.92 g, 0.12 mol) was added to a solution of

potassium hydrogen carbonate (23.60 g, 0.24 mol) in methanol (200 ml). The mixture

was then stirred and cooled to – 78°C. Ethyl iodide (37.3 g, 0.24 mol) was then added

dropwise to the mixture before being refluxed for 5 hours. The methanol was then

removed under vacuum, the solids produced were triturated with chloroform, and any

undissolved solids were filtered off. The chloroform solution was then treated with

diethyl ether until a white precipitate was formed. The white solid was then filtered

off and redissolved in water (200 ml) and the pH adjusted to 12 using a sodium

hydroxide solution (25 % w/w). The aqueous solution was then extracted with dichloromethane (3 x 100 ml) and the organic layer was dried over anhydrous sodium sulphate. The solution was then filtered and the solvent removed to give a white solid of *N*-ethyl-cis-2,6-dimethylpiperidine.

N-ethyl-cis-2,6-dimethylpiperidine (5 g, 35.39 mmol) was dissolved in methanol (50 ml) and potassium hydrogen carbonate (6.98 g, 69.73 mmol) was added and the solution stirred. The reaction mixture was then cooled to – 78 °C and methyl iodide (9.94 g, 70.49 mmol) was added dropwise before being refluxed for 24 hours. The methanol was then stripped off under reduced pressure and the solids triturated with dichloromethane, before being filtered and the solvent removed under vacuum to give a white solid. The product was then recrystallised from a mixture of warm isopropanol and just enough ethanol for the solids to dissolve to give white crystals (9.5 g, 95.5 %): Mpt 288 – 289 °C; ^{1}H NMR (300 MHz, D$_2$O) δ 1.33 (6H, d, (C$\underline{H}_3$)$_2$-CH), 1.4-1.8 (6H, m, (C$\underline{H}_2$)$_3$), 2.70 (3H, s, N-CH$_2$-C$\underline{H}_3$), 2.73 (2H, m, N-C$\underline{H}_2$-CH$_3$), 2.98 (3H, s, N-C$\underline{H}_3$), 3.46 (2H, m, N-(C$\underline{H}$-CH$_3$)$_2$); ^{13}C NMR (300 MHz, D$_2$O) δ 15.16 (N-CH$_2$-$\underline{C}$H$_3$), 21.94 (CH$_2$-$\underline{C}$H$_2$-CH$_2$), 27.47 (CH$_2$-CH$_2$-$\underline{C}$H$_2$), 28.19 ($\underline{C}$H$_2$-CH$_2$-CH$_2$), 34.75 & 34.84 (N-(CH-$\underline{C}$H$_3$)$_2$), 49.51 (N-$\underline{C}$H$_3$), 54.42 (N-$\underline{C}$H$_2$-CH$_3$), 63.71 & 70.46 (N-($\underline{C}$H-CH$_3$)$_2$); CHN analysis calcd. 42.41 %C, 7.83 %H and 4.95 %N found 41.23 %C, 8.02 %H and 5.07 %N.
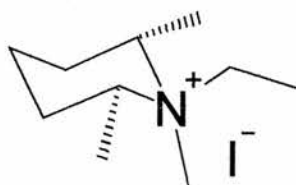
Figure 3.10 *N*-ethyl-*N*-methyl-2,6-dimethylpiperidinium iodide

3.1.2.11 5-Azonia-spiro[4.5]decane iodide (ASD)

Piperidine (2.55 g, 29.96 mmol) was added to a NaOH (100 ml, 0.03 Moldm^{-3})

solution and refluxed for 30 minutes under constant stirring. 1,4-diiodobutane (4.70 g,

15.17 mmol) was then added dropwise over a period of 30 minutes to the refluxing

mixture. The solution was then cooled to 0°C before being shaken with an ice cold

solution of sodium hydroxide (50 ml, 40 % w/w). An oily layer was formed, which

was taken up in chloroform and then extracted using diethyl ether until a solid

precipitated. The solid was then filtered, washed with diethyl ether and recrystallised

from isopropanol and just enough ethanol, to give white crystals (7.30 g, 91.25 %):

Mpt 239 – 240 °C; ^{1}H NMR (300 MHz, D$_2$O) δ 1.48 (4H, m, NCH$_2$-(C$\underline{H}_2$)$_2$-CH$_2$N),

1.62 (6H, m, NCH$_2$-(C$\underline{H}_2$)$_3$-CH$_2$N), 3.02 (8H, m, N-(C$\underline{H}_2$)$_4$); ^{13}C NMR (300 MHz,

D$_2$O) δ 21.48 (N-CH$_2$-($\underline{C}$H$_2$)$_2$-CH$_2$), 22.21 (($\underline{C}$H$_2$)$_3$-CH$_2$-N), 44.55 (N-($\underline{C}$H$_2$)$_4$); CHN

analysis calcd. 61.52 %C, 10.33 %H and 7.97 %N found 49.99 %C, 10.61 %H and

11.92 %N.
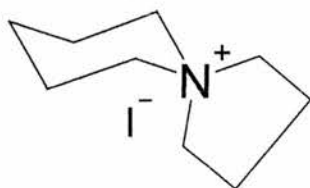
Figure 3.11 5-Azoniaspiro[4.5]decane iodide

3.1.2.12 Anion Exchange

All of the above quartenary ammonium halide salts were then converted to the

hydroxide form, for use in zeolite synthesis, by dissolving them in water and stirring

for 24 hours with a large excess of Ambersep-900 OH anion exchange resin. The

ammonium salts were recovered by filtering out the exchange resin and concentrating the resultant filtrate. The concentration of the solutions was determined in triplicate by titration against 0.1021 moldm^{-3} hydrochloric acid using phenolphthalein as a pH indicator. The titrations showed that on average over 95 % of the initial quartenary ammonium halide had been converted to the hydroxide form. It is thought that this small loss, <5 %, was due to some of the quartenary ammonium salt being trapped in the exchange resin even though the resin was always flushed with a large excess of water.

3.1.3 Discussion and Conclusions

As mentioned in the introduction, many of these quartenary ammonium salts have been previously used as structure directing agents for zeolite synthesis. However, very few of the synthesis procedures for these SDAs have been published and even less information is available on their characterisation. The experimental details given in this chapter are the optimal results achieved, usually after several synthesis attempts in order to improve purity and percentage yields. Initial syntheses often produced low yields of powder like products that ^{1}H NMR showed to contain mixtures of the starting materials and the desired products. Recrystallisation of these products from toluene yielded semi-crystalline material in quite low yields. Attempts to synthesise known zeolites using these quartenary ammonium cations as SDAs failed, even though literature procedures were followed. These failed syntheses were thought to be due to too many impurities remaining in the quartenary ammonium salts, preventing the zeolites from crystallising.

Various methods were employed to improve the syntheses of these SDAs, including changes of solvents and increasing the length of time reactions were left before being worked up. These changes led to an increase in yields and purity and results were further improved by changing the recrystallisation method. It was generally found that the use of hot isopropanol or ethyl acetate with just enough ethanol or methanol to dissolve the solids worked very well for nearly all of the quartenary ammonium halides.

The majority of the SDAs were eventually synthesised in high enough yields and high purities as proven by ^{1}H and ^{13}C solution NMR and CHN analysis. The slight variations between the calculated and the analysed CHN results are thought to be due small amounts of trapped solvent and water within the crystals. The presence of this water is thought to be due the samples absorbing it from the air, as it is well known that quartenary ammonium halides are highly hygroscopic.

The synthesis of *N*-Benzyl-1,4-diazabicyclo[2.2.2]octane chloride, however, was not found to be as straight forward as suggested in the literature.[4] All attempts to synthesise this molecule yielded a white crystalline product, which on analysis by ^{1}H NMR showed only 1 resonance for the diazabicyclo (DABCO) group instead of the two as expected. This is thought to be due to the reaction between the benzyl chloride and the 1,4-diazabicyclo[2.2.2]octane occurring at both free N sites giving the 'dimer' as shown in Figure 3.12.
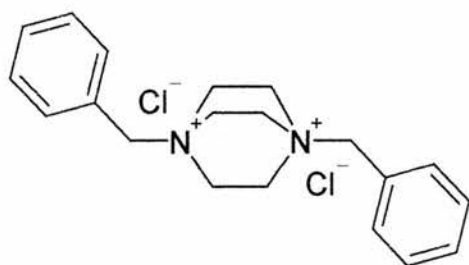
Figure 3.12 Di-substituted DABCO,

The product was confirmed as the 'dimer' by ^{13}C NMR, and the result of the CHN

analysis (62.72 %C, 7.67 %H, 7.43 %N) showed that the predicted values for the di-

substituted DABCO (65.75 %C, 7.17 %H, 7.67 %N) were a lot closer than those for

the mono-substituted DABCO (65.40 %C, 8.02 %H, 11.73 %N). The reaction always

seemed to mainly produce the di-substituted DABCO even if the ratio of the starting

products was 1:1. This of course led to implications when trying to synthesise ITQ-4

using this molecule as a SDA as will be discussed in Chapter 3.2.2.3.

Three new derivatives of *N*-benzylquinuclidinium were successfully synthesised,

these being the 4-fluoro, 4-nitro and 4-methoxy versions. All three of these molecules

were synthesised from the reaction of quinuclidine and a halo form of the

functionalised benzyl group. The para substituted benzyl group was chosen as all of

these were available commercially and it was thought that the SDAs made from these

would best fit within the zeolite cages. The method for the synthesis of these three

derivatives was based on that for the *N*-benzylquinuclidinium as no previous literature

entries could be found.

Altogether eleven quartenary ammonium salts were successfully synthesised, with

three of these believed to be completely new SDAs. They were all converted to the

hydroxide form in aqueous solutions and used for the synthesis of pure silica zeolites.

3.2 Synthesis of Pure Silica Zeolites

3.2.1 Introduction

Pure silica zeolites are normally synthesised using a four co-ordinate silicon source such as tetraethyl orthosilicate (TEOS) and fluoride ions as a mineralising agent. The synthesis gels usually have low silica to water ratio, often between 1:1 and 1:15 and this leads to low density zeolites.[5,6] The TEOS is hydrolysed using a hydroxide form of the SDA to produce ethanol, which is allowed to fully evaporate along with any excess water from the reaction mixture until no ethanol can be detected by ^{1}H NMR. Fluoride ions are then added to the synthesis mixture in the form of either hydrofluoric acid or ammonium fluoride. Figure 3.13 shows the reaction scheme for the general synthesis of pure silica zeolites.[7,8]
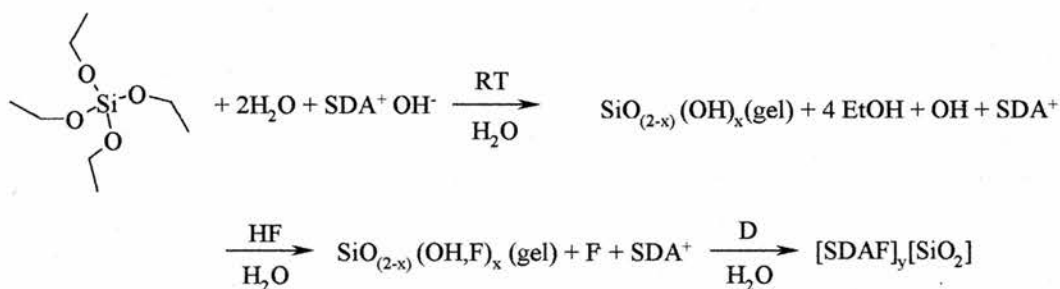
Figure 3.13 Reaction scheme for the synthesis of a typical pure silica zeolite.

The aims of this work were two fold; firstly to synthesise high quality samples, containing single crystals, of pure silica zeolites to enable further structural studies to be performed on them. Secondly, to use newly functionalised benzylquinuclidinium cations to synthesise pure silica zeolites so that the effect of these functional groups on the structures obtained could be investigated.

3.2.2 Experimental Details and Discussions

3.2.2.1 [t-BTMA,F]-AST and [Qncld,F]-AST (Octadecasil)

Pure silica octadecasil (AST)[9] was synthesised using t-butyltrimethylammonium cations with a gel composition of SiO_2: $0.5C_7H_{19}NO$: $0.5HF$: $20H_2O$. In a typical synthesis tetraethylorthosilicate (6.87 g, 32.98 mmol) was hydrolysed with an aqueous solution of $C_7H_{18}N^+$ ^-OH (130.0 cm^3, 0.126 $moldm^{-3}$). The solution was left to stir and lose ethanol (6.07 g, 0.132 mol), produced by the hydrolysis of the TEOS. Water (126.6 g, 7 mol) was then removed from the mixture under reduced pressure to give a white thick liquid. Hydrofluoric acid (48 %) (0.68 g, 34.36 mmol) was then added to the mixture and the thick gel produced thoroughly homogenised by hand. The white gel produced was loaded into Teflon-lined stainless steel autoclaves and heated under static conditions at 170°C. After 12 days the autoclaves were removed from the oven and cooled rapidly in cold water. The contents were filtered and washed thoroughly with distilled water to give a white crystalline solid.

The second method of synthesising pure silica octadecasil was using the SDA quinuclidine with a final gel composition of SiO_2: 0.5 Quinuclidine: 0.5 HF: 20 H_2O. In a typical synthesis quinuclidine (1.85 g, 16.64 mmol) was fully dissolved in distilled water (12 g, 0.667 mol) before Cab-O-Sil (precipitated silica) (2 g, 33.29 mmol) was added under constant stirring by hand. Hydrofluoric acid (48 %) (0.69 g, 34.67 mmol) was then added to the solution and the mixture further homogenised by hand. The resultant gel was then loaded into Teflon-lined steel autoclaves and heated under static conditions at 170 °C. After 15 days the autoclaves were removed from the oven and quenched in cold water. The contents were filtered and washed with

distilled water to give the highly crystalline white product, which was dried at 90 °C for 10 hours.

The products were confirmed as octadecasil by comparing the powder X-ray diffraction pattern collected (Figure 3.14) to those published by the International Zeolite Association.[10]

Figure 3.14 Powder pattern of as-made [Qncld,F]-AST (octadecasil)

Both methods of synthesising the pure silica clathrasil octadecasil were successful. However, it was found that using quinuclidine as a SDA provided better quality octadecasil crystals and proved to be a much more repeatable synthesis method. The crystals of octadecasil, especially those synthesised using quinuclidine as a SDA, had the characteristic diamond shape and were grown to a maximum size of 800 μm.

The octadecasil was synthesised for use as a secondary NMR standard for ^{19}F and ^{29}Si MAS experiments and for setting up $^{29}Si\{^{19}F\}$ CP MAS experiments.

3.2.2.2 [tPABr,F]-MFI (Silicalite-1)

The purely siliceous zeolite silicalite-1 was synthesised using the SDA tetrapropylammonium bromide with a final gel composition of SiO_2: 0.08 tPABr: NH_4F: 20 H_2O. In a typical synthesis tPABr (0.71 g, 2.67 mmol) and NH_4F (1.23 g, 33.21 mmol) were dissolved in distilled water (12g, 0.667 mol). To this solution was added Cab-O-Sil (2 g, 33.29 mmol) and the mixture thoroughly homogenised by hand. The resultant solution was then transferred to Teflon-lined steel autoclaves and heated at 190 °C under static conditions. The autoclaves were removed from the oven after 48 hours and quenched in cold water. The product was then recovered by filtration and washed thoroughly with distilled water before being dried at 90 °C for 12 hours.

The product was confirmed as silicalite-1 by comparing the powder X-ray diffraction pattern collected (Figure 3.15) to those published by the International Zeolite Association.[10]

Figure 3.15 XRD powder pattern of as made [tPABr,F]-MFI (silicalite-1)

There are several methods reported for the synthesis of silicalite-1, which give a wide range of crystal sizes and quality. The chosen method was based on that published by Fyfe *et al.* with a slight modification to the synthesis gel to decrease the crystallisation time.[11] This modification involved increasing the quantity of ammonium fluoride, so that the ratio of Si: NH_4F was 1:1, instead of the published 1: 0.04. Changing this ratio cut the crystallisation time from a minimum of 14 days to just 48 hours, with no visible effect on crystal size or shape. The reason for this dramatic decrease in crystallisation time is believed to be due to the larger quantity of F^- ions in the reaction gel, which have a better mineralising effect and lead to faster formation of Si-O-Si bonds.

The crystals of silicalite-1 produced were on average 100 x 30 x 20 μm in size, with the characteristic lozenge shape.

3.2.2.3 [BzQ,F]-IFR and [BzDABCO]-IFR (ITQ-4)

The pure silica zeolite ITQ-4[1,3] was synthesised using the SDA *N*-benzyl quinuclidinium hydroxide with a gel composition of SiO_2: 0.5 BQOH: 0.5 NH_4F: 14 H_2O. In a typical synthesis TEOS (3.467g, 16.64 mmol) was hydrolysed with an aqueous solution of BQOH (36.405 cm^3, 0.23 moldm^{-3}) and the resulting ethanol (3.06 g, 66 mmol) allowed to evaporate. Water (30.19 g, 1.67 mol) was then removed from the mixture under reduced pressure to give a thick white paste. Ammonium fluoride (0.308 g, 8.31 mmol) was then added to the paste and the resultant gel thoroughly homogenised by hand. The gel was then transferred to Teflon-lined steel autoclaves and heated in a 150 °C oven under constant rotation (~ 60 rpm). After 13 days the

autoclaves were removed and quenched in cold water and the resultant product filtered and washed with distilled water, before being dried at 90 °C for 12 hours.

The product was confirmed as ITQ-4 by comparing the powder X-ray diffraction pattern collected (Figure 3.16) to those published by the International Zeolite Association.[10]

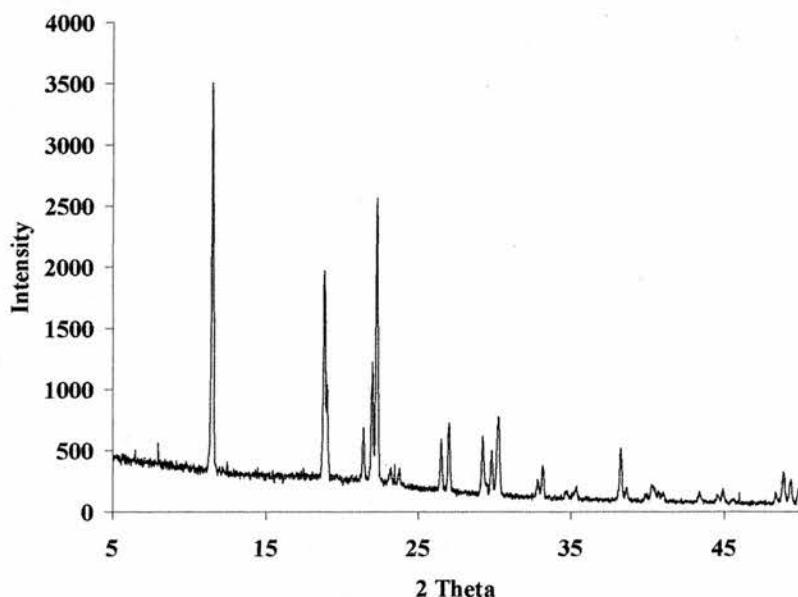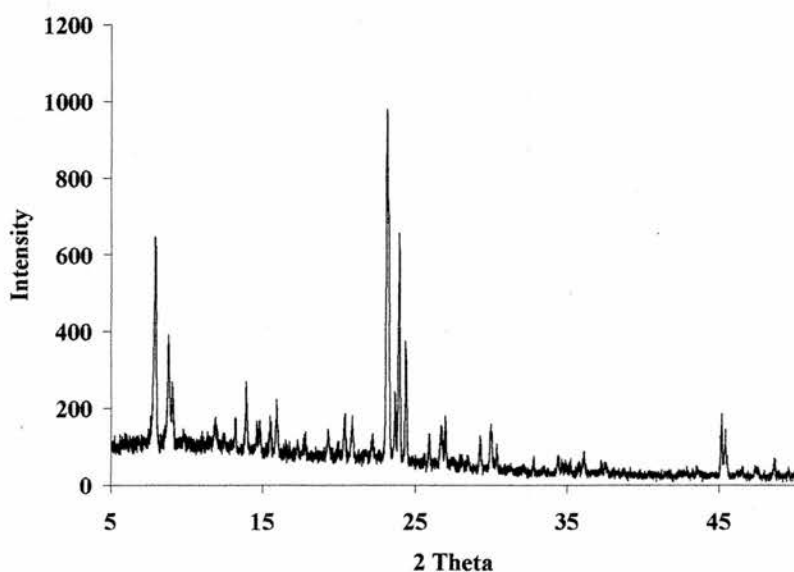Figure 3.16 XRD powder pattern of as-made [BzQ,F]-IFR (ITQ-4)

Initial attempts to synthesise an ITQ-4 sample were not successful and this is thought mainly to be due to the inability to rotate the samples whilst heating. Rotating a sample at around 60 rpm whilst heating appears to aid the crystallisation process. Barrett *et al.*[7] have proposed that this process stops the SDAs burning / decomposing and allows the normal crystallisation to occur. The sample of [BzQ,F]-IFR was eventually synthesised using the exact method of Barrett *et al.* under dynamic conditions and this produced small block shaped crystals with an average size of 30 x

20 x 20 μm. The sample was synthesised to allow confirmation of the previously reported non-linear optical properties.

The pure silica zeolite ITQ-4 was also attempted to be synthesised following the method reported by Barrett *et al.* using *N*-benzyl-1,4-diazabicyclo[2.2.2]octane as a structure directing agent.[3] In a typical synthesis, a gel with the composition SiO_2: 0.50 BzDABCO: 0.50 HF: 10 H_2O was prepared from the hydrolysis of TEOS (3.467g, 16.64 mmol) with an aqueous solution of BzDABCO (26.8 cm^3, 0.31 moldm^{-3}). The ethanol produced (3.06 g, 66 mmol) was removed under reduced pressure along with the excess of water (21.7 cm^3, 1.2 mol). Hydrofluoric acid (48 %, 0.346 g, 17.34 mmol) was then added and the resultant gel thoroughly stirred by hand. The gel was then loaded in to Teflon-lined stainless steel autoclaves and heated at 150 °C and rotated at 60 rpm. After 15 days the autoclaves were removed from the oven and quenched in cold water. The resulting product was a white powder, which was recovered by filtration and thoroughly washed with distilled water and acetone before being dried in air at 90 °C for 15 hours.

Visual examination of the product with an optical microscope revealed that no crystals were present in the sample and this was confirmed by powder XRD. The synthesis was repeated on 8 separate occasions, with again none of these yielding a crystalline product. The failure of these syntheses has been attributed to the impurity of *N*-benzylDABCO structure directing agent, with often a large proportion of the SDA solution being comprised of the di-benzyl substituted 1,4-diazabicyclo[2.2.2]octane as discussed in Chapter 3.1.3. Barrett *et al.* did, however, report in their paper that the BzDABCO SDA had a lower thermal stability than the benzylquinuclidine and this lead them to choose not study the sample any further.

This may also explain why ITQ-4 could not be synthesised from even the purest sample of BzDABCO, even when the greatest of care was taken to follow the reported method.

3.2.2.4 [DMABO,F]-ITE (ITQ-3)

TEOS (3.467 g, 16.64 mmol) was hydrolysed in an aqueous solution of DMABO (68.22 g, 0.122 moldm^{-3}) and the mixture left to loose ethanol (3.067 g, 66mmol). Water (64.39 g, 3.57 mol) was then removed under reduced pressure and hydrofluoric acid (48 %) (0.346 g, 17.34 mmol) was added and the thick gel thoroughly stirred by hand to give the composition SiO_2: 0.5 DMABO: 0.5 HF: 7.7 H_2O. The gel was loaded into Teflon-lined stainless steel autoclaves and heated at 150 °C at 60 rpm for 28 days. After which, the autoclave was removed from the oven and quenched in cold water. The crystalline product was filtered and washed with distilled water before being dried at 90 °C for 12 hours.

The product was confirmed as ITQ-3[5] by comparing the powder X-ray diffraction pattern collected (Figure 3.17) to those published by the International Zeolite Association.[10]
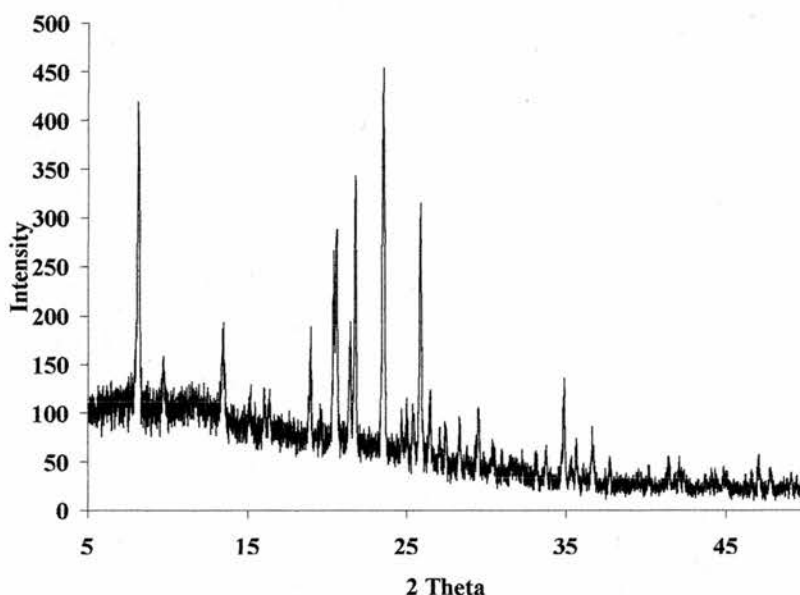
Figure 3.17 XRD powder pattern of as-made [DMABO,F]-ITE (ITQ-3)

The sample of [DMABO,F]-ITE was synthesised following the procedure first published by Camblor *et al.*[5] The method of synthesis involved heating the sample whilst rotating it at approximately 60 rpm. In a similar way to [BzQ,F]-IFR, it was found that ITQ-3 could not be synthesised without rotating the sample and again this is thought to be due to the dynamical conditions stopping the SDA decomposing. The sample of ITQ-3 was synthesised to allow the structure to be determined by microcrystal XRD and MAS NMR. The previous structural determination of ITQ-3 by Camblor *et al.* was done using powder diffraction data, which did not allow the fluoride ions or the SDA to be located within the framework.

3.2.2.5 [DECDMP,F]-SFF (SSZ-44) and [DECDMP,F]-STF (SSZ-35)

The pure silica form of SSZ-44[12,13] was synthesised using the SDA *N,N*-diethyl-2,6-dimethylpiperidinium hydroxide (DECDMP). In a typical synthesis TEOS (3.467 g, 16.64 mmol) was hydrolysed in an aqueous solution of DECDMP (66.89 g, 0.124 moldm^{-3}). The solution was left to allow for the evaporation of the ethanol (3.067 g, 66 mmol) produced from the hydrolysis of the TEOS and then water (64.13 g, 3.56 mol) was removed under reduced pressure. Hydrofluoric acid (48 %) (0.346 g, 17.34 mmol) was then added to the mixture to form a thick gel that was thoroughly homogenised by hand giving a final composition of SiO_2: 0.5 DECDMP: 0.5 HF: 4 H_2O. The gel was then loaded into a Teflon-lined stainless steel autoclave and heated in an oven at 140 °C. After 7 days the autoclave was removed and quenched in cold water and the white crystalline product recovered by filtration and thoroughly washed with water. The sample was then dried at 90 °C for 12 hours.

The product was confirmed as SSZ-44 by comparing the powder X-ray diffraction pattern collected (Figure 3.18) to those published by the International Zeolite Association.[10]
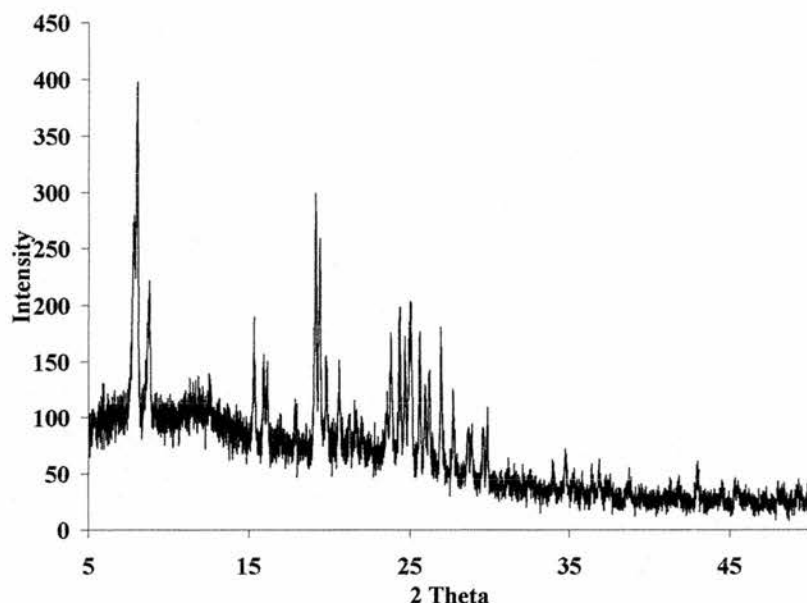
Figure 3.18 XRD powder pattern of as-made [DECDMP,F]-SFF (SSZ-44)

Purely siliceous SSZ-35[2,13,14] was synthesised using the SDA DECDMP with an overall gel composition of SiO_2: 0.5 DECDMP: 0.5 HF: 1 H_2O. In a typical synthesis TEOS (3.467 g, 16.64 mmol) was hydrolysed in an aqueous solution of DECDMP hydroxide (66.89 g, 0.124 $moldm^{-3}$) and the ethanol (3.067 g, 66 mmol) produced allowed to evaporate. Water (65.03 g, 3.6 mol) was then removed from the mixture leaving a dry powder. Hydrofluoric acid (0.346 g, 17.34 mmol) was then added to the dry powder and then mixture homogenised by hand as far as possible. The thick powder was then placed into the Teflon-lined autoclave and heated at 190 °C for 6 days. The autoclave was then quenched in cold water and the crystalline product filtered and washed with distilled water before being dried at 90 °C for 10 hours.

The product was confirmed as SSZ-35 by comparing the powder X-ray diffraction pattern collected (Figure 3.19) to those published by the International Zeolite Association.[10]
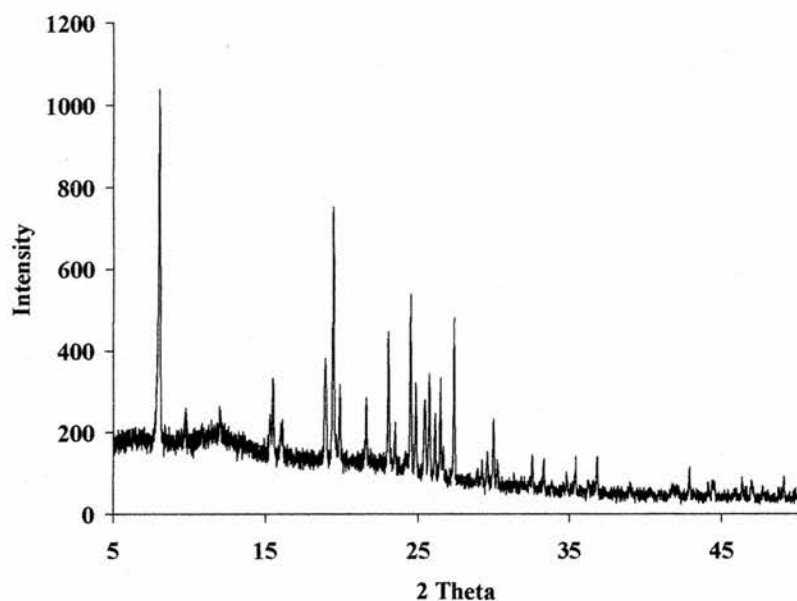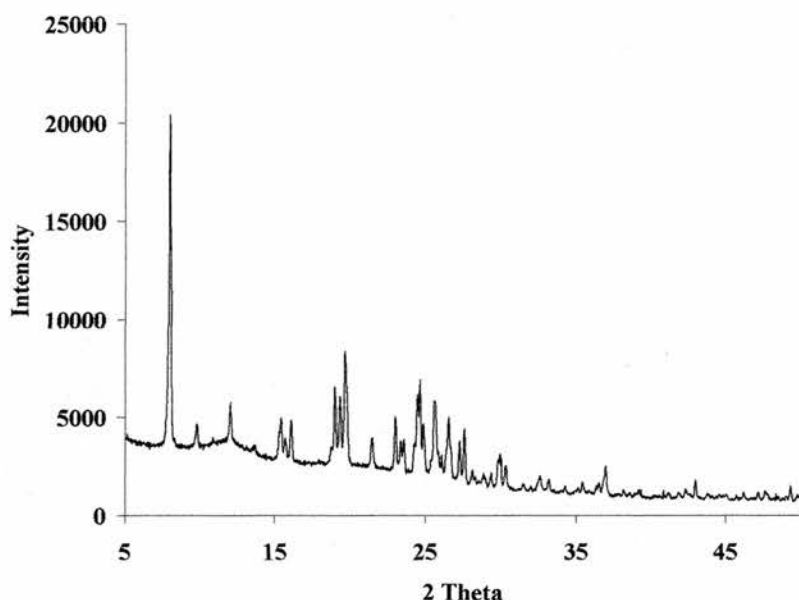
Figure 3.19 XRD powder pattern of as-made [DECDMP,F]-STF (SSZ-35)

The samples of both [DECDMP,F]-SFF and [DECDMP,F]-STF were synthesised

using the method of Villaescusa *et al.* The zeolites SSZ-35 and SSZ-44 are

topologically related and were first reported by Wagner *et al.* who synthesised them

using hydroxide ions as a mineralising agent.[15] The structures of these zeolites can be

described by their periodic building unit (PerBU), which consists of a layer type unit

containing sixteen tetrahedral units. In SSZ-35 these layer type units are related to

each other through inversion centres, whilst in SSZ-44 the layers are related through

mirror planes. Precise synthesis conditions are required in order to control which

material is produced, and it has now been shown that it is possible to synthesise a

whole intergrowth series from STF to SFF.[13] This intergrowth series is different from

some other zeolite series as the SDA for both SSZ-35 and SSZ-44 is DECDMP, with

the only change in the synthesis conditions being the quantity of water. To ensure that

the samples produced were purely SSZ-35 and SSZ-44 and that no mixtures were

produced, the synthesis conditions were slightly altered from those reported by Villaescusa *et al.* This involved adjusting the temperature at which the zeolites were heated to 190 °C for SSZ-35 and 140 °C for SSZ-44 instead of the reported 170 °C and 150 °C respectively. Reducing the synthesis temperature for SSZ-44 produced high quality single crystals with the average dimensions 20 x 10 x 5 μm. Good quality single crystals of SSZ-35 could not be produced, instead the sample consisted of very fine needles, which resembled those reported by Villaescusa *et al.*

The sample of [DECDMP,F]-SFF was synthesised to enable the structure to be properly characterised by microcrystal XRD and NLO as well as to perform MAS NMR experiments to help elucidate the location of the F$^-$ ions. The [DECDMP,F]-STF sample was prepared to help confirm the previous structural studies by Fyfe *et al.*, using NLO to show whether or not the organic SDAs were aligned noncentrosymmetrically.[16]

3.2.2.6 [DMASD,F]-STF (Mu-26)

Mu-26[17] was synthesised using the SDA 6,10-dimethyl-5-azoniaspiro[4.5]decane hydroxide (DMASD) with a final gel composition of SiO_2: 0.5 DMASD: 0.5 HF: 5 H_2O. In a typical synthesis, an aqueous solution of the hydroxide salt of DMASD was used to hydrolyse TEOS (3.467 g, 16.64 mmol) and the resulting ethanol (3.067 g, 66 mmol) was allowed to evaporate. Water (6.75 g, 0.375 mol) was then removed, to give a thick paste, to which hydrofluoric acid (48 %) (0.346 g, 17.34 mmol) was added. The gel was then stirred by hand before being loaded into the Teflon-lined autoclaves and heated under static conditions at 190 °C. After 8 days the autoclaves

were removed and quenched in cold water and the crystalline product filtered and washed with distilled water. The sample was then dried at 90 °C for 12 hours. The product was confirmed as Mu-26 by comparing the powder X-ray diffraction pattern collected (Figure 3.20) to that previously published Harbuzaru *et al.*[17]
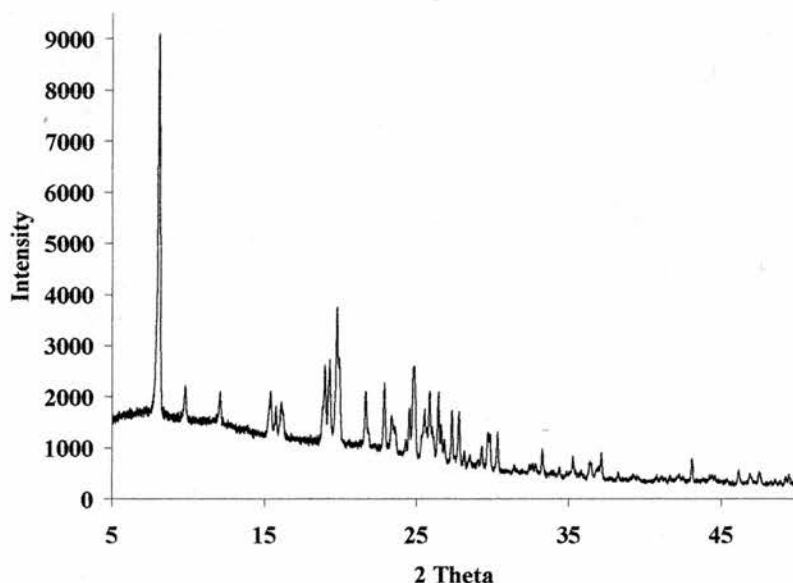
Figure 3.20 XRD powder pattern for as-made [DMASD,F]-STF (Mu-26)

The sample of [DMASD,F]-STF was synthesised using a modification of the method first published by Harbuzaru *et al.*[17] Their synthesis method involved mixing the synthesis gel in the same ratios as above and then heating the gel at 170 °C for 30 days, producing a sample of highly interpenetrating needles. Previous work on the related material [DECDMP,F]-STF[14] has shown that the STF framework is often better prepared at higher temperatures. Therefore, the synthesis of [DMASD,F]-STF was performed at 190 °C for just 8 days, yielding a white sample containing very fine needles. The sample is believed to be less intergrown than that described by

Harbuzaru *et al.*, but still the crystals were too small and not well enough formed to enable studying by microcrystal XRD.

The sample was initially synthesised with the aim of fully characterising it using microcrystal XRD. However, as soon as it was determined that single crystals could not be prepared, it was decided that the sample seemed ideal for investigation by MAS NMR.

3.2.2.7 [FBzQ,F]-IFR

The 4-flurobenzylquinuclidinium cations were synthesised to act as a SDA for the synthesis of ITQ-4, as the molecule is very similar to the known SDA for ITQ-4. The synthesis conditions were, therefore, based on those known to work for ITQ-4;[3] the full list of experiments attempted is presented in Table 3.1. In a typical synthesis TEOS (3.467 g, 16.64 mmol) was hydrolysed using an aqueous solution of 4-fluorobenzylquinuclidinium hydroxide (15.13 g, 0.55 moldm^{-3}). The ethanol (3.06 g, 66 mmol) produced by the reaction was allowed to evaporate along with the excess water (8.966 g, 0.49 mol) to give a thick white paste. Ammonium fluoride (0.308 g, 8.31 mmol) was then added and the mixture stirred by hand. The gel was then transferred to Teflon-lined stainless steel autoclaves and heated at 150 °C under constant rotation (~60 rpm). After 14 days the autoclaves were removed from the oven and quenched in cold water. The contents of the autoclaves were filtered and washed with distilled water, but appeared not to have reacted as the product was a very thick gel. The gel was dried at 90 °C for 12 hours and the XRD powder pattern showed that it contained no crystalline material.

Gel composition	Temperature (°C)	Number of days	Rate of rotation (No. / min)	Final product
SiO$_2$: 0.5FBzQ: 0.5NH$_4$F: 14 H$_2$O	150	21 14	0 60	No sign of any reaction
SiO$_2$: 0.5FBzQ: 0.5HF: 10H$_2$O	150	21 14	0 60	No sign of any reaction
SiO$_2$: 0.5FBzQ: 0.5NH$_4$F: 5H$_2$O	150	21 14	0 60	No sign of any reaction

Table 3.1 Reaction conditions for the attempted synthesis of [FBzQ,F]-IFR.

The reaction was repeated several times with varying conditions, as listed in Table 3.1, but the product was always the same. It was initially thought that making the synthesis gel drier would encourage crystallisation, however, this did not occur. In a final attempt to get a crystalline product one autoclave containing a gel with the initial composition SiO$_2$: 0.5FBzQ: 0.5NH$_4$F: 14H$_2$O was left in the oven for 60 days at 150 °C. The white powder produced still appeared to be amorphous and this was confirmed by powder XRD.

This inability of the 4-fluorobenzylquinuclidinium cations to act as a SDA for this synthesis of ITQ-4 may be explained by recent work on the effect of fluorinated benzylpyrolidines as SDAs for the synthesis of AlPO-5 by Gómez-Hortigüela *et al.*.[18,19] In this work, they used computational techniques to study the differing structure directing effects of meta (*m*), ortho (*o*) and para (*p*) substituted benzylpyrolidine for the formation of AlPO-5 (AFI). Their results showed that the ortho and para-fluoro isomers were not good templates due to the poor packing of the template molecules inside the AFI pores. The unfunctionalised benzylpyrolidine and the meta-fluoro isomer were shown to pack very efficiently and to direct the synthesis of AFI. Benzylpyrolidine and the meta-fluoro isomer were also shown to form stable dimers inside the AlPO framework, unlike the ortho and para-fluoro isomers that

showed template-template repulsion arising between the fluorine atoms. This may also be the case in ITQ-4, as benzylquinuclidinium is well known as an excellent SDA for the synthesis of ITQ-4.[3] The para-fluoro isomer, however, has been shown not to act as SDA for the synthesis of IFR frameworks and this may be due to the unfavourable packing and/or template-template repulsion. To fully understand why 4-fluorobenzylquinuclidinium cations do not act as SDA for the synthesis of ITQ-4 will require an in-depth computational study of the template – template and template – framework interactions.

3.2.2.8 [NOBzQ,F]-IFR

The 4-nitrobenzylquinuclidinium cation was prepared for use as SDA in the synthesis of pure silica ITQ-4, for the same reasons given previously for the 4-fluorobenzylquinuclidinium. Table 3.2 lists the full reaction conditions attempted and the products of the reactions. In a typical synthesis TEOS (3.467 g, 16.64 mmol) was hydrolysed using an aqueous solution of 4-nitrobenzylquinuclidinium hydroxide (33.98 g, 0.245 moldm^{-3}). The ethanol (3.06 g, 66 mmol) produced by the reaction and the excess water (27.59 g, 1.53 mol) were removed under reduced pressure to give a white gel. Ammonium fluoride (0.308 g, 8.31 mmol) was then added and the gel thoroughly homogenised by hand. The gel was then loaded in to Teflon-lined stainless steel autoclaves and placed in a 150 °C oven under dynamic conditions (~60 rpm). After 14 days the autoclaves were removed and quenched in cold water and the contents filtered and washed with distilled water. The product was then dried at 90 °C for 12 hours to give a brown amorphous powder.

Gel composition	Temperature (°C)	Number of days	Rate of rotation (No. / min)	Final product
1SiO$_2$: 0.5NOBzQ: 0.5HF: 20H$_2$O	150 170	21 21	0 0	Burnt amorphous product
SiO$_2$: 0.5NOBzQ: 0.5NH$_4$F: 14H$_2$O	150 150	14 30	60 0	Burnt amorphous product
1SiO$_2$: 0.5NOBzQ: 0.5HF: 20H$_2$O	100 100	21 30	60 0	Burnt amorphous product

Table 3.2 Reaction conditions for the attempted synthesis of [NOBzQ,F]-IFR.

All attempts at synthesising ITQ-4 using 4-nitrobenzylquinuclidinium as a SDA were unsuccessful. The product in all cases was a dark brown amorphous powder that appeared to be burnt. The reason for this burnt material is thought to be the SDA undergoing decomposition due to the presence of the nitro group. Initial attempts at synthesising ITQ-4 using this SDA were done under static conditions and it was believed that rotating the sample during heating might stop the SDA from burning. Rotating the sample at approximately 60 rpm whilst heating did not seem to have any effect on the synthesis, and the product of these reactions was still a burnt material. No records of any other nitro functionalised organics being used as SDAs could be found in the literature and this may indicate that the nitro group makes the organic too unstable for use a SDA.

3.2.2.9 [MeOBzQ,F]-IFR

As for the fluoro and nitro derivatised benzylquinuclidinium, 4-methoxybenzylquinuclidinium was prepared for the synthesis of ITQ-4. Table 3.3 gives the details of all the reactions attempted and the products of these reactions. In a typical synthesis an aqueous solution of 4-methoxybenzylquinuclidinium hydroxide (16.84 g, 0.494 moldm^{-3}) was used to hydrolyse TEOS (3.467 g, 16.64 mmol). The resulting ethanol (3.06 g, 66 mmol) was removed from the mixture along with the excess water (10.57 g, 0.58 mol) under reduced pressure. Ammonium fluoride (0.308 g, 8.31 mmol) was then added to the gel, which was then stirred thoroughly by hand. The thick gel was then transferred to Teflon-lined stainless steel autoclaves and heated at 150 °C in an oven at constant rotation (~ 60 rpm). After 14 days the autoclaves were removed and quenched in cold water and the contents filtered and washed with distilled water. The resulting product appeared not to have reacted in a similar way as for the 4-fluorobenzylquinuclidinium SDA. Further syntheses were attempted, as listed in Table 3.3, but again none of these showed any sign of crystalline material in the product. However, one autoclave with the composition described above was left in the 150 °C oven under static conditions for 90 days and this produced a low quality sample of octadecasil.

Gel composition	Temperature (°C)	Number of days	Rate of rotation (No. / min)	Final product
SiO_2: 0.5MeOBzQ: 0.5NH_4F: 14H_2O	150	14 21	60 0	No sign of any reaction
SiO_2: 0.5MeOBzQ: 0.5HF: 14H_2O	150	14 30	60 0	No sign of any reaction
SiO_2: 0.5MeOBzQ: 0.5NH_4F: 5H_2O	150	14	60	No sign of any reaction

Table 3.3 Reaction conditions for the attempted synthesis of [MeOBzQ,F]-IFR.

The pure silica zeolite ITQ-4 could not be synthesised using 4-methoxybenzylquinuclidinium cations as a SDA. Several different reaction conditions were attempted and the products of all of these was a thick white unreacted gel. There may be many reasons why this organic doesdoes not act as a SDA for the crystallisation of ITQ-4, including electronic and / or steric effects. MeOBzQ cations did produce a very low quality sample of octadecasil consisting of a few intergrown crystals and lots of amorphous material. However, due to the lack and quality of the octadecasil crystals, it was not possible to determine if MeOBzQ was incorporated in to the structure or whether the template had broken up and a fragment had acted as a SDA.

3.2.3 Conclusions

Eleven organic structure directing agents have been synthesised by alkylating a range of primary, secondary and tertiary amines to produce the desired quartenary ammonium salts. The synthesis conditions have been optimised to ensure that the products of the reactions were highly pure and could be produced in sufficient yields. All of the SDAs have been as fully characterised as possible using ^{1}H and ^{13}C NMR and elemental analysis, with much of this information not being previously available even though many of the molecules have been widely used as SDAs. Three new derivatives of *N*-benzylquinuclidinium have been synthesised, but all three have been shown not to act as SDAs for the synthesis of ITQ-4. This is thought to be due to size and steric effects and it is now believed that the meta isomers of fluoro-, methoxy- and nitro- benzylquinuclidinium may act as better SDAs. The meta isomers of the starting alkyl halides are currently not commercially available, and this would mean the

syntheses of these SDAs would be significantly more complex. Potential problems with *N*-benzylDABCO as a SDA have been highlighted during this work, due to its ability to readily form dimers. Although some work has been done on using DABCO polymers as SDAs, these have never been used with fluoride based pure silica zeolite syntheses.[4]

Several pure silica zeolites have been successfully synthesised using fluoride ions as a mineralising agent. These syntheses have been shown to require a very high purity of the starting compounds and particularly the organic structure directing agents. The lack of highly pure SDAs led initially to several zeolite syntheses failing. However, improving the synthesis of the organic SDAs, so that they could be produced in high yield and purity, enabled many pure silica zeolites to be synthesised. The majority of the zeolite syntheses produced samples containing microcrystals (~ 20 x 10 x 10 μm) that were of good enough quality for further structural studies by single crystal X-ray diffraction, and often in sufficient quantity for analysis by MAS NMR. Samples of many of the zeolites reported here were also sent to other research groups to enable different structural investigations to be performed. These included more advanced MAS NMR studies at the Universities of British Columbia and Southampton and high-pressure studies at the University of Birmingham.

3.3 References for Chapter 3

1. P. A. Barrett, M. A. Camblor, A. Corma, R. H. Jones and L. A. Villaescusa, *Chem. Mater.*, 1997, **9**, 1713.

2. L. A. Villaescusa, P. A. Barrett and M. A. Camblor, *Chem. Comm.*, 1998, 2663.

3. P. A. Barrett, M. A. Camblor, A. Corma, R. H. Jones and L. A. Villaescusa, *J. Phys. Chem. B*, 1998, **102**, 4147.

4. T. Takewaki, L. W. Beck and M. E. Davis, *Microporous Mater.*, 1999, **33**, 197.

5. M. A. Camblor, A. Corma, P. Lightfoot, L. A. Villaescusa and P. A. Wright, *Angew. Chem., Int. Ed. Engl.*, 1997, **36**, 2659.

6. M. A. Camblor, A. Corma and S. Valencia, *J. Mater. Chem.*, 1998, **8**, 2137.

7. P. A. Barrett, M. J. Diaz-Cabanas, M. A. Camblor and R. H. Jones, *J. Chem. Soc., Faraday Trans.*, 1998, **94**, 2475.

8. M. A. Camblor, L. A. Villaescusa and M. J. Diaz-Cabanas, *Top. Catal.*, 1999, **9**, 59.

9. P. Caullet, J. L. Guth, J. Hazm, J. M. Lamblin and H. Gies, *Eur. J. Solid State Inorg. Chem.*, 1991, **28**, 345.

10. M. M. J. Treacy, J. B. Higgins and R. Vonballmoos, *Zeolites*, 1996, **16**, 327-&.

11. C. A. Fyfe, D. H. Brouwer, A. R. Lewis and J. M. Chezeau, *J. Am. Chem. Soc.*, 2001, **123**, 6882.

12. L. A. Villaescusa, M. Puche and M. A. Camblor, International Symposium on Zeolites and Microporours Crystals, ZMPC 2000, Sendai, Japan, August, 2000, 2000, p. 2-P-015.

13. L. A. Villaescusa, W. Z. Zhou, R. E. Morris and P. A. Barrett, *J. Mater. Chem.*, 2004, **14**, 1982.

14. L. A. Villaescusa, P. S. Wheatley, I. Bull, P. Lightfoot and R. E. Morris, *J. Am. Chem. Soc.*, 2001, **123**, 8797.

15. P. Wagner, S. I. Zones, M. E. Davis and R. C. Medrud, *Angew. Chem., Int. Ed. Engl.*, 1999, **38**, 1269.

16. I. Bull, L. A. Villaescusa, S. J. Teat, M. A. Camblor, P. A. Wright, P. Lightfoot and R. E. Morris, *J. Am. Chem. Soc.*, 2000, **122**, 7128.

17. B. Harbuzaru, M. Roux, J. L. Paillaud, F. Porcher, C. Marichal, J. M. Chezeau and J. Patarin, *Chem. Lett.*, 2002, 616.

18. L. Gomez-Hortiguela, F. Cora, C. R. A. Catlow and J. Perez-Pariente, *J. Am. Chem. Soc.*, 2004.

19.   J. Perez-Pariente, L. Gomez-Hortiguela and M. Arranz, *Chem. Mater.*, 2004, **16**, 3209.

4.0 Microcrystal X-ray Diffraction Studies of Zeolites

4.1 [BzDABCO,B]-IFR (B-SSZ-42)

4.1.1 Introduction

SSZ-42 is a high silica large pore zeolite that was first reported by Zones *et al.* of the Chevron Research and Technology Company in 1997.[1] The zeolite was prepared as a borosilicate using the SDA N-benzyl-1,4-diazabicyclo[2.2.2]octane, during attempts to make a borosilicate version of zeolite beta. Initial testing of this material showed that it could well have commercial applications as it is thermally stable up to at least 800 °C and could be very useful as a catalyst for hydrocarbon processing.[2]

The structure of B-SSZ-42 was solved using microcrystal X-ray diffraction data for a very small crystal (15 x 15 x 35 μm) and refined using powder X-ray diffraction data. This enabled the silica framework to be described as monoclinic with the spacegroup C2/m with 4 topologically distinct T-atoms and 10 oxygen atoms. SSZ-42 has the framework type IFR and is characterised by an undulating; one-dimensional channel system with distorted 12 membered ring pores. The periodic building unit contains 16 T-atoms forming five 4-MR, four 5-MR and two 6-MR as shown in Figure 4.1.
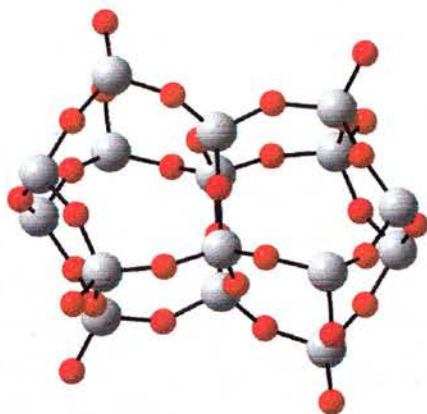
Figure 4.1 IFR $[4^5 5^4 6^2]$ periodic building unit

At around the same time as Zones *et al.* reported the structure of [BzDABCO,B]-IFR, Barrett *et al.* reported the structure determination of the pure silica zeolite ITQ-4,[3] which is isostructural with SSZ-42.

Unfortunately, owing to the small size and quality of the SSZ-42 crystal, the single crystal data was not precise enough to allow Zones *et al.* to locate the template molecules or enable accurate bond distance measurements. Elemental analysis of B-SSZ-42 showed that there were two template molecules per unit cell and molecular modelling gave a possible location of the template as spanning the volume from one side pocket diagonally to the next (Figure 4.2).
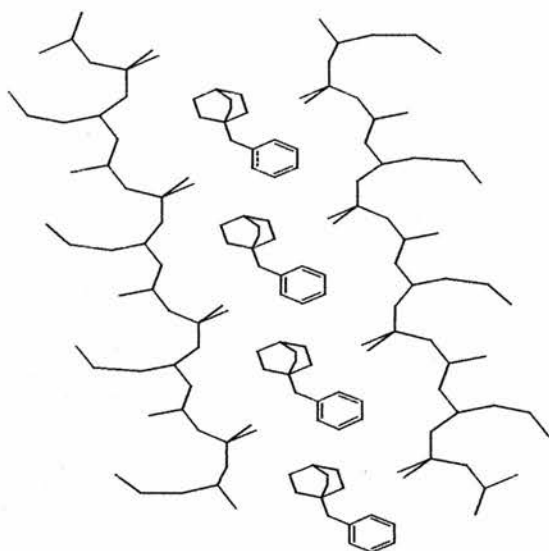
Figure 4.2 xz projection of B-SSZ-42 showing minimised location of template molecules. Redrawn from ref.2.

The molecular modelling, however, was unable help them fully resolve the orientation of the template molecule. If the template molecules were aligned head to tail with long-range order as in ITQ-4, the symmetry would be reduced relative to that of the framework.[4] This would have produced extra peaks in the diffraction pattern, which they report were not observed and led them to believe that the template molecules were disordered. The paper does report, however, that the molecular modelling showed that there was a reduction in the stabilisation energy when four unit cells were considered for the Cm spacegroup. This reduction in energy corresponded to template-template interactions and could lead to head to tail long-range ordering. This led the authors to be uncertain about the location of the template molecules and about the overall assigned spacegroup.

4.1.2 Results and Discussion

4.1.2.1 Synthesis

The sample of B-SSZ-42 was synthesised by C.Y. Chen of Chevron Research and Technology according to the following method.[2] Boric acid (0.25 g, 4.03 mmol) was fully dissolved in an aqueous solution of *N*-benzylDABCO hydroxide (18.11 g, 0.9 moldm^{-3}) and the resulting solution stirred. Sodium hydroxide (0.08 g, 2mmol) was then added to the solution along with Cab-O-Sil (3.26 g, 54.36 mmol) and the resulting mixture stirred at room temperature for 1 hour. The gel was then heated in a stainless-steel autoclave under static conditions for 10 days at 150 °C. The resulting product was recovered by filtration, washed with distilled water and then dried in air at room temperature.

4.1.2.2 Microcrystal X-ray Diffraction and Non-linear Optics

The crystals of the as-synthesised SSZ-42 sample were too small (15 x 15 x 35 μm) for analysis on a standard laboratory diffractometer and were, therefore, analysed using synchrotron radiation at Station 9.8 of the Daresbury SRS.[5]

The structure of the as-made SSZ-42 was solved by direct methods (SHELXS-97)[6] and refined with a full-matrix least-squares technique (SHELXL-97)[7] using the WinGX[8] suite of programs. Two potential symmetries had been suggested previously by Zones *et al.*, the centrosymmetric spacegroup C2/m and the noncentrosymmetric spacegroup Cm.

Refinement of the centrosymmetric C2/m model against the data collected for [BzDABCO,B]-IFR was unsatisfactory, with the final refinement giving an agreement

factor, R-factor, of approximately 8%. Lowering the symmetry to the noncentrosymmetric spacegroup Cm significantly improved the refinement, with a final agreement factor of 4.3%. The refinement revealed only small residual electron density peaks, which could not be modelled as extra/disordered template atoms. Given the difference between the agreement factors for the Cm and C2/m models, it is clear that the structure is correctly solved in the spacegroup Cm. The refinement of the final model against the X-ray diffraction data for [BzDABCO,B]-IFR suggested a monoclinic spacegroup Cm, with unit cell parameters of a= 18.5938(10) Å, b= 13.3145(7) Å, c= 7.5925(4) Å and β= 101.6530(10)°. Full details of the data collection and the refinement parameters can be seen in Table 4.1, and the details of the structure determination can be found on the attached CD as Crystallographic Information Files.
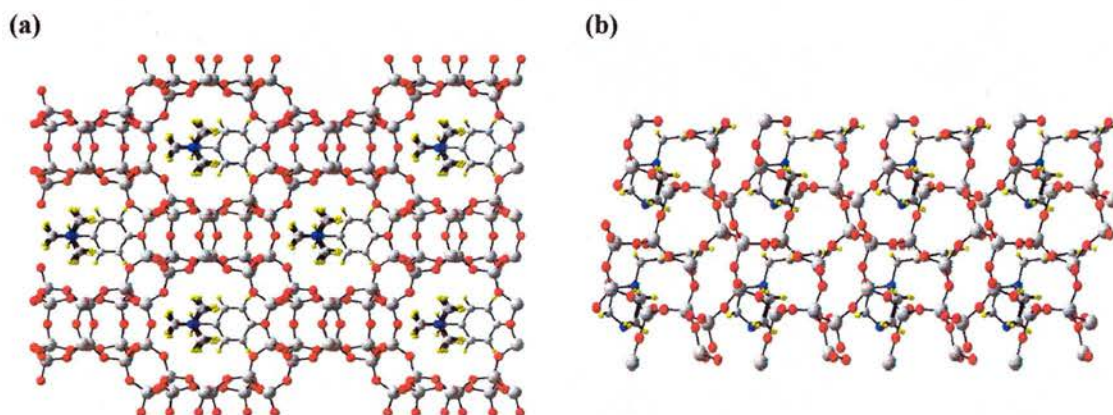
(a)   **(b)**

Figure 4.3 Structure of [BzDABCO,B]-IFR, showing alignment of template molecules.

Identification code	B-SSZ42
Empirical formula	$Si_{32-X}B_XO_{66}C_{28}H_{34}N_2$
Formula weight	~2391.45
Temperature	150(2) K
Wavelength	0.69492 Å
Crystal system	Monoclinic
Space group	Cm
Unit cell dimensions	a = 18.5938(10) Å alpha = 90°
	b = 13.3145(7) Å beta = 101.6530(10)°
	c = 7.5925(4) Å gamma = 90°
Volume	1840.91(17) Å^3
Z, Calculated density	1, 2.157 Mg/m^3
Absorption coefficient	0.554 mm^{-1}
F(000)	1210
Crystal size	0.02 x 0.01 x 0.01 mm
Theta range for data collection	1.85 to 29.55°
Limiting indices	-25<=h<=25, -18<=k<=18, -10<=l<=10
Reflections collected / unique	8708 / 4932 [R(int) = 0.0276]
Completeness to theta = 29.55	93.3 %
Absorption correction	None
Max. and min. transmission	0.9945 and 0.9890
Refinement method	Full-matrix least-squares on F^2
Goodness-of-fit on F^2	0.641
Final R indices [I>2σ(I)]	R1 = 0.0431, wR2 = 0.1207
R indices (all data)	R1 = 0.0453, wR2 = 0.1243
Absolute structure parameter	0.4(2)
Largest diff. Peak and hole	1.142 and –0.686 e.A^{-3}

Table 4.1 Crystal data and structure refinement for [BzDABCO,B]-SSZ42.

The structure of B-SSZ-42 is in good agreement with the previous study by Zones *et al.* and clearly has the same characteristic 12-membered ring windows and the undulating one-dimensional channels (Figure 4.3). This framework type has been given the code IFR, which was first described for the pure silica zeolite ITQ-4. The

organic templates (SDAs) in SSZ-42 are all clearly aligned in the same direction, a phenomenon first noticed by Bull and co-workers in as-made ITQ-4.[4] In this paper, they report that the structure of as-made ITQ-4 is best described in the spacegroup I*m* (a non-standard setting of Cm) with the noncentrosymmetric ordering of the template molecules within the pores of the zeolite. The mechanism of this ordering has always been believed to be due to the presence of pentacoordinate $[SiO_{4/2}F]^-$ units, which occupy one of two possible $[4^3 5^2 6^1]$ cages, and are dynamically disordered over two possible sites within the cage it occupies. The effect of these negatively charged fluoride ions is to electrostatically attract the positive charge on the cationic templates. As the template molecules are asymmetric, with the positive charge localised at one end of the molecule, this produces an excellent driving force for all the molecules to align with their positive charges as close as possible to the fluoride ions. In a centrosymmetric model, some of the template molecules must align in the opposite orientation with their positive charges further away from the fluoride ions. However, [BzDABCO,B]-IFR does not contain any fluoride ions to cause the alignment of the templates within the pores. Fluoride ions, therefore, must not be the only driving force for the alignment of the template molecules. Instead, it is proposed that in the absence of fluoride ions the driving force must be either simple dipolar interactions or electrostatic repulsions between neighbouring template molecules. The template used for the synthesis of SSZ-42 is *N*-benzylDABCO, as shown in Figure 4.4.
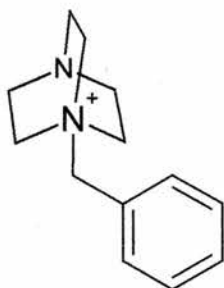
Figure 4.4 *N*-benzyldiazabicyclo[2.2.2]octane

The molecule has a positively charged DABCO group and an electron rich benzene ring at opposite ends. This could lead to a dipole – dipole interaction between the positively charged N atom on one template molecule and the electron rich benzene ring on an adjacent molecule (Figure 4.5a) as seen for the ordering of p-nitroaniline inside zeolite pores.[9] An alternative or even supplementary mechanism can be proposed based upon electrostatic repulsion between two neighbouring molecules. Both the benzene ring end and the positively charged DABCO end of the molecule will repel the like ends of an adjacent molecule, producing the long range ordering of the templates seen in SSZ-42 (Figure 4.5b). Either of these two mechanisms could account for the ordering seen in [BzDABCO,B]-IFR, but it is more likely that some combination of these is the real driving force.
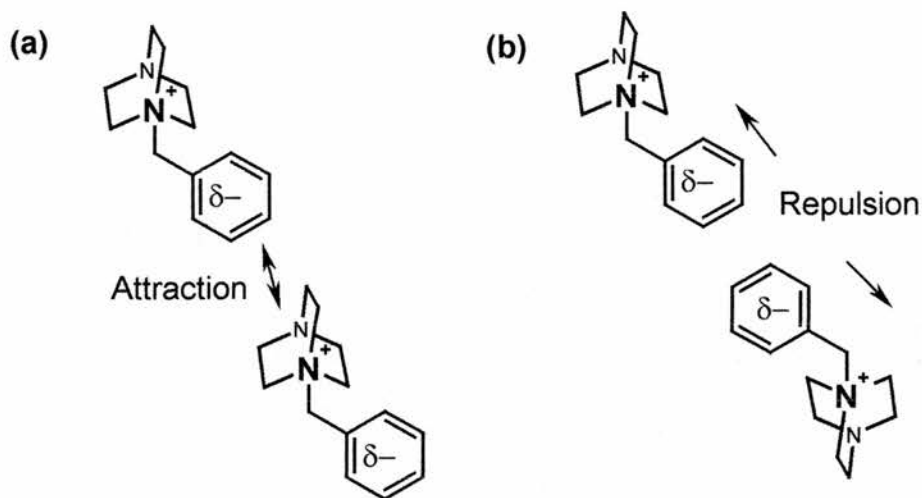
Figure 4.5 Diagrammatic representation of the attractive (a) and / or repulsive interactions between template molecules (b).

The noncentrosymmetric ordering of the template molecules seen in ITQ-4 was confirmed by the frequency doubling of infrared laser light (1064 nm) to give a visible green light (532 nm), thus confirming the that crystal structure is indeed noncentrosymmetric. A similar test was performed on a powdered sample of [BzDABCO,B]-IFR and a small quantity of green light could be observed, thus confirming the noncentrosymmetric spacegroup Cm.

The sample of [BzDABCO,B]-IFR was prepared as a borosilicate material, however, the sites of the boron atoms could not be located. The structure solution does not show the location of the B atoms and there were no significant differences between the temperature factors for the Si sites, which may have indicated that B was present on one or more particular sites. The location of the B atoms may also have indicated the mechanism of the template alignment, as the substitution of boron for silicon in the framework introduces a negative charge, in the form of BO_4^-. This

negative charge on the framework would attract the positive charge on the organic template and provide a third potential mechanism for the observed alignment.

The computer modelling studies reported by Zones *et al.* showed that there was a change in the stabilisation energy when four unit cells were considered for the spacegroup Cm. This implies that there is some form of interaction between neighbouring template molecules and this could be sufficient to allow long-range ordering of the organic templates.

4.1.3 Conclusions

The structure of [BzDABCO,B]-IFR has been determined by microcrystal X-ray diffraction and the organic templates located within the 12-MR channels. The template molecules are aligned noncentrosymmetrically inside a centrosymmetric zeolite framework and this has been confirmed by non-linear optical measurements. The presence of the long-range ordering within this material has shown that fluoride ions are not the sole mechanism by which this phenomenon can occur. The most likely cause is due to template–template interactions, although it is currently not possible to rule out some form of boron–template interaction. The ordering seen in SSZ-42 could enable new optical materials to be synthesised, as it combines a robust inorganic framework with optically active organic guest species.

4.2 [DMABO,F]-ITE (ITQ-3)

4.2.1 Introduction

Pure silica zeolites have attracted a great deal of interest over the past couple of decades due to their lack of Si-OH defects giving them unique hydrophobic properties.[10,11] In particular it was thought that a pure silica zeolite with small 8-MR channels would show excellent shape-selectivity and adsorption properties, which would be highly valued for separation and purification processes.

ITQ-3 was the first pure silica polymorph that had a two dimensional system of eight-membered ring channels and was reported by Camblor *et al.* in 1997.[12] The material was shown to have the second lowest framework density[13] (16.3) (FD, defined as number of Si atoms per 1000 $Å^3$) among all the known pure silica polymorphs and the largest microporous volume.

The structure of calcined ITQ-3 was solved using synchrotron powder X-ray diffraction data and indexed as orthorhombic (a = 20.622(1), b = 9.7242(4), c = 19.623(2) Å) with symmetry Cmcm, $Cmc2_1$, or C2cm as determined by the systematic absences. These spacegroups were consistent with the ^{29}Si MAS NMR, which showed four resonances corresponding to the four crystallographically inequivalent silicon sites. Camblor *et al.* noticed that the unit cell size and symmetry observed for ITQ-3 is consistent with the unit cell twinning seen in the zeolite framework type RTH.[14,15] From this, the authors were able to use the starting atomic coordinates for RTH and apply Cmcm symmetry to produce a model for the structure of ITQ-3. The ITE framework is shown in Figure 4.6 and comprises a two-dimensional system of interconnected 8-MR channels running perpendicular to each other. At the intersection of these channels are four large cavities per unit cell, which can be

denoted as $[4^65^86^48^4]$, where the authors speculate the template molecules could be located.

The aim of this work was, therefore, to solve the structure of as made [DMABO,F]-ITE and to locate the position of the fluoride ions and the SDAs.

4.2.2 Results and Discussion

4.2.2.1 Synthesis

The crystals of as-made [DABCO,F]-ITE were synthesised as reported in Chapter 2.2.2.4 following the general method reported by Camblor *et al.*.[12,16] The crystals produced were slightly tabular in shape with an average size of approximately 30 x 20 x 20 µm.

4.2.2.2 Microcrystal X-ray Diffraction and Non-linear Optics

The crystals of the as-synthesised ITE sample were too small (30 x 20 x 20 µm) for analysis on a standard laboratory diffractometer and were, therefore, analysed using synchrotron radiation at Station 9.8 of the Daresbury SRS.[5]

The structure of the as-made ITE was solved by direct methods (SHELXS-97)[6] and refined with a full-matrix least-squares technique (SHELXL-97)[7] using the WinGX[8] suite of programs.

The structure of [DMABO,F]-ITE was eventually refined in the orthorhombic spacegroup C222$_1$ with unit cell dimensions of a = 9.6956(16) Å, b = 20.564(3) Å and c = 19.510(3) Å with an R-factor of approximately 10%. The data was also fitted to

other models for the C*mcm* and C*mc*2_1 spacegroups although the refinements did not give as good a fit.

Full details of the data collection and the refinement parameters can be seen in Table 4.2, and the details of the structure determination can be found on the attached CD as Crystallographic Information Files.

Identification code	[DMABO,F]-ITE
Empirical formula	$Si_{32}O_{64}FC_{10}H_{10}N_2$
Formula weight	2100.08
Temperature	150(2) K
Wavelength	0.69500 Å
Crystal system	Orthorhombic
Space group	$C222_1$
Unit cell dimensions	a = 9.6956(16) Å alpha = 90°
	b = 20.564(3) Å beta = 90°
	c = 19.510(3) Å gamma = 90°
Volume	3889.9(11) Å^3
Z, Calculated density	2, 1.793 Mg/m^3
Absorption coefficient	0.517 mm^{-1}
F(000)	2106
Crystal size	0.03 x 0.02 x 0.02 mm
Θ range for data collection	1.94 to 29.59°
Limiting indices	-10<=h<=13, -28<=k<=26, -26<=l<=27
Reflections collected / unique	12939 / 5319 [R(int) = 0.0595]
Completeness to theta = 29.59	94.9 %
Absorption correction	None
Refinement method	Full-matrix least-squares on F^2
Data / restraints / parameters	5319 / 0 / 229
Goodness-of-fit on F^2	1.068
Final R indices [I>2sigma(I)]	R1 = 0.1053, wR2 = 0.2560
R indices (all data)	R1 = 0.1174, wR2 = 0.2641
Absolute structure parameter	0(4)
Largest diff. peak and hole	2.268 and -1.178 e.Å^{-3}

Table 4.2 Crystal data and structure refinement for [DMABO,F]-ITE.

The structure of as-made [DMABO,F]-ITE is shown in Figure 4.6(a), unfortunately it was not possible to refine the location of the DMABO template molecules as these were disordered within the zeolite channels. Several attempts were made to locate the template molecules; however, all of these were unsuccessful. The electron density corresponding to the disordered template molecules was removed from the model using the program SQUEEZE to improve the refinement.[17] The location of the fluoride ions was determined, as shown in Figure 4.6(a) as the green atoms. As expected from previous studies of fluoride containing zeolites the fluoride anions occupy the small $[4^45^3]$ cages as shown in Figure 4.6(b).[18-21] This location of the fluoride ions is in excellent agreement with MAS NMR studies by Koller *et al.*, who showed that the fluoride ions in ITQ-3 were bonded to the silicate framework, and this is confirmed with an internuclear distance of 1.92(8) Å from the diffraction data.[22]

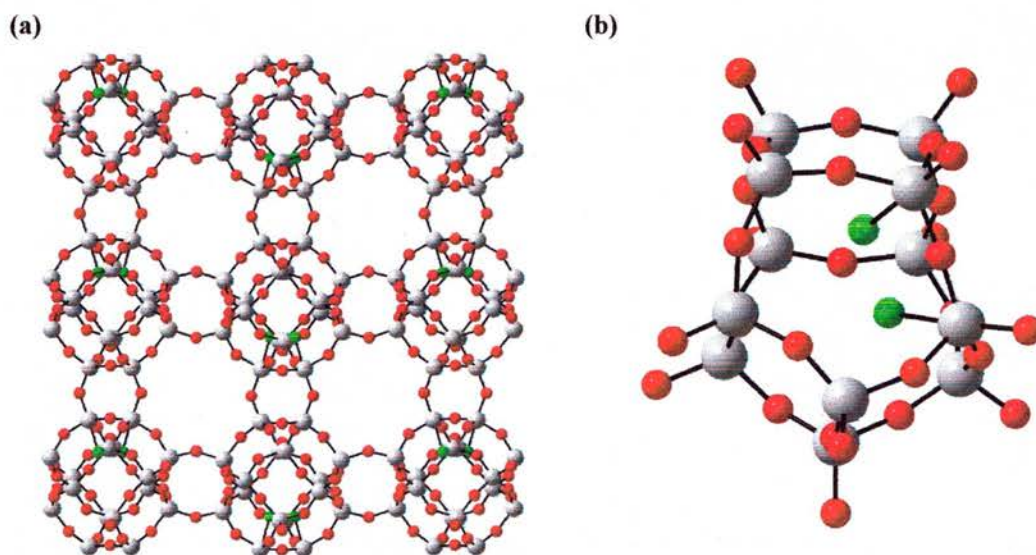**(a)**   **(b)**

Figure 4.6 (a) Si-O-Si framework, showing the location of the fluoride ions. (b) $[4^45^3]$ cage showing disordered fluoride ions.

Each of the small $[4^45^3]$ cages only contains one fluoride ion; however, the time average picture observed from the X-ray diffraction data shows two fluoride ions per small cage. This is due to the fluoride ions being statically disordered over two sites within the small cages, one being the fluoride containing trigonal bipyramidal silicon site and the other a standard tetrahedral silicon.[23] Standard X-ray diffraction data, including synchrotron data, is not of high-enough resolution, on its own, to allow the separation of these two disordered sites. This leads to an average of the trigonal bipyramidal and tetrahedral sites, giving a much greater value for the F-Si bond distance. Chapter 5 shows how the combination of microcrystal X-ray diffraction and solid state NMR can be used to resolve this disorder in the fluoride containing zeolite SFF.

Although it was not possible to locate the template molecules from the X-ray diffraction data, non-linear optical measurements indicated that the template molecules may be aligned within the 8-membered ring channels by the generation of a second harmonic signal. It is, however, also possible that the template molecules are disordered within the channels and that the framework itself is noncentrosymmetric. The second harmonic signal was of similar strength to that previously reported for ITQ-4, as can be seen in Figure 4.7.[4]
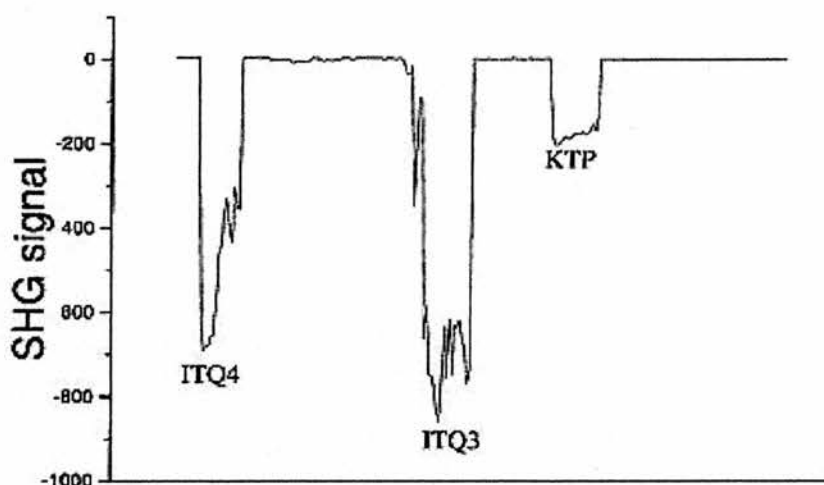
Figure 4.7 Second harmonic generation graph for ITQ-4 and ITQ-3 samples; the recorded KTP reference sample is 1/70 of actual signal strength.

Without being able to accurately locate the template molecules within the ITE framework, it is not possible to determine the mechanism of the template ordering. Much higher quality crystals would need to be synthesised to enable the template molecules to be located and this may then enable the exact mechanism of template alignment within zeolites to be determined.

4.2.3 Conclusions

The pure silica framework of as-made [DMABO,F]-ITE and the location of the fluoride ions have been successfully determined using the high-flux single crystal diffractometer at the Daresbury SRS. The previous description of the ITE framework by Camblor *et al.* has been confirmed and although the template molecules could not be refined, it could be seen that they most likely occupied the $[4^65^86^48^4]$ cages as previously suggested. The location of the fluoride ions in the small $[4^45^3]$ cages is in

good agreement with previous studies on other fluoride containing zeolites and helps confirm the proposed role of the fluoride ion as a structure directing agent for the formation of small cages.

[DMABO,F]-ITE has been shown to have the non-linear optical effect of second harmonic generation, thus confirming the noncentrosymmetric spacegroup and could potentially be used in the future as an optically active composite material. Further work is needed to locate the template molecules within the zeolite pores and enable the mechanism of the template ordering to be determined. However, the strength of the SHG signal will need to be increased if these types of materials are ever to become new optically active materials. This may be achieved by simply changing the SDA or by functionalising the current template molecules.

4.3 References for Chapter 4

1. C. Y. Chen, L. W. Finger, R. C. Medrud, P. A. Crozier, I. Y. Chan, T. V. Harris and S. I. Zones, *Chem. Comm.*, 1997, 1775.

2. C. Y. Chen, L. W. Finger, R. C. Medrud, C. L. Kibby, P. A. Crozier, I. Y. Chan, T. V. Harris, L. W. Beck and S. I. Zones, *Chem-Eur J.*, 1998, **4**, 1312.

3. P. A. Barrett, M. A. Camblor, A. Corma, R. H. Jones and L. A. Villaescusa, *Chem. Mater.*, 1997, **9**, 1713.

4. I. Bull, L. A. Villaescusa, S. J. Teat, M. A. Camblor, P. A. Wright, P. Lightfoot and R. E. Morris, *J. Am. Chem. Soc.*, 2000, **122**, 7128.

5. R. J. Cernik, W. Clegg, C. R. A. Catlow, G. Bushnell-Wye, J. V. Flaherty, G. N. Greaves, I. Burrows, D. J. Taylor, S. J. Teat and M. Hamichi, *J. Synchrotron Rad.*, 1997, **4**, 279.

6. G. M. Sheldrick, *Programs for Crystal Structure Analysis. Release 97-2*, 1997.

7. Siemens, *SHELXTL. Structure Determination Software*, Siemens Analytical X-ray Instruments Inc., Madison, Wisconsin, USA, 1995.

8. L. J. Farrugia, *J. Appl. Crystallogr.*, 1999, **32**, 837.

9. S. D. Cox, T. E. Gier, G. D. Stucky and J. Bierlein, *J. Am. Chem. Soc.*, 1988, **110**, 2986.

10. P. A. Barrett, M. J. Diaz-Cabanas, M. A. Camblor and R. H. Jones, *J. Chem. Soc., Faraday Trans.*, 1998, **94**, 2475.

11. M. A. Camblor, L. A. Villaescusa and M. J. Diaz-Cabanas, *Top. Catal.*, 1999, **9**, 59.

12. M. A. Camblor, A. Corma, P. Lightfoot, L. A. Villaescusa and P. A. Wright, *Angew. Chem., Int. Ed. Engl.*, 1997, **36**, 2659.

13. M. A. Camblor, A. Corma and S. Valencia, *J. Mater. Chem.*, 1998, **8**, 2137.

14. B. Marler, U. Oberhagemann, S. Vortmann and H. Gies, *Abstr. Pap. Am. Chem. S.*, 1995, **209**, 36-PETR.

15. S. Vortmann, B. Marler, H. Gies and P. Daniels, *Microporous Mater.*, 1995, **4**, 111.

16. H. Koller, A. Wolker, H. Eckert, C. Panz and P. Behrens, *Angew. Chem., Int. Ed. Engl.*, 1997, **36**, 2823.

17. A. L. Spek, *PLATON. A Multipurpose Crystallographic Tool*, Utrecht University, Utrecht, The Netherlands , 1999.

18. L. A. Villaescusa, I. Bull, P. S. Wheatley, P. Lightfoot and R. E. Morris, *J. Mater. Chem.*, 2003, **13**, 1978.

19. L. A. Villaescusa, P. S. Wheatley, I. Bull, P. Lightfoot and R. E. Morris, *J. Am. Chem.*

Soc., 2001, **123**, 8797.

20. P. S. Wheatley, C. J. Love, J. J. Morrison, I. J. Shannon and R. E. Morris, *J. Mater. Chem.*, 2002, **12**, 477.

21. D. S. Wragg and R. E. Morris, *J. Phys. Chem. Solids*, 2001, **62**, 1493.

22. H. Koller, A. Wolker, L. A. Villaescusa, M. J. Diaz-Cabanas, S. Valencia and M. A. Camblor, *J. Am. Chem. Soc.*, 1999, **121**, 3368.

23. C. A. Fyfe, D. H. Brouwer, A. R. Lewis, L. A. Villaescusa and R. E. Morris, *J. Am. Chem. Soc.*, 2002, **124**, 7770.

5.0 Determining the Structure of Fluoride Containing Zeolites Using

MAS NMR

5.1 Determining the Structure of the 5-Coordinate Silicon

The use of fluoride ions as a mineralising agent in zeolite syntheses has led to the production of many new and exciting materials.[1] These include; zeolites with low framework densities,[2] large crystals of zeolites,[3] pure silica zeolites with very few framework defects[4,5] and some unique non-linear optical materials.[6] Many of these features have a direct influence on the potential applications of these new materials. For example, the lack of defects in a zeolite increases its hydrophobicity, which can be important in catalytic applications.[7] This is particularly the case for pure silica zeolites that have been doped with catalytic metals such as Ti, Fe or B.[8-10] This has led to significant interest in understanding the role of the fluoride ions and how they are involved in controlling the structure and, therefore, the properties of zeolites.[11] Much of the initial work on understanding the role of the fluoride ions during synthesis has been done by Camblor and co-workers.[7,11] They have suggested two main roles of the fluoride ions; the first as a mineralising agent, and secondly in a catalytic role as detailed in Chapter 1. The fluoride ions have also been shown to be incorporated in to the frameworks of many pure silica zeolites, by both solid state NMR[12] and X-ray diffraction.[13-15] Koller *et al.* have used solid state NMR to show that the fluoride ions are often incorporated in to the zeolite framework and are present as the five coordinate species $[SiO_{4/2}F]^-$.[16,17] The presence of these units, in the absence of fluoride motion, can easily be identified by ^{29}Si MAS NMR as a *J*-

coupled doublet with a chemical shift of between −145 and −150 ppm. In the case of

fluoride motion, as seen in [tPABr,F]-MFI by Fyfe *et al.*, then a broad averaged

resonance centred around −125 ppm can be seen.[18] These five coordinate silicon units

have been shown to balance the charge on the cationic organic structure directing

agents. Morris and co-workers have shown this to be the case by using microcrystal

X-ray diffraction on fluoride containing pure silica zeolites[6,14], AlPOs[19] and GaPOs[20].

These studies have indicated that the fluoride ions can usually be located in small

cages, often consisting of four-membered rings, and it is thought that the fluoride ions

energetically stabilise these cages.[14,21] So far, the locations of only a few fluoride ions

in pure silica zeolites have been reported from XRD data and these are detailed in

Table 5.1. This is often due to the difficulties in locating the fluoride ions, as fluorine

and oxygen have similar numbers of electrons making it difficult to distinguish

between them using X-ray diffraction. This is particularly the case for fluoride

anions, which are isoelectronic with OH groups that are often present as defects in

zeolite frameworks.

Zeolite / Clathrasil	F⁻ location	F-Si distance	Source of XRD	Reference
[tPABr,F]-MFI	Adjacent to N^+	2.32 and 2.45 Å	Single crystal	22
Silicalite-1	$[4^1 5^2 6^2]$ cage	-	Powder XRD	23
[Q,F]-AST Octadecasil	$[4^6]$ cage	2.67 Å	Single crystal	24
[Cocp₂,F]-NON Nonasil	$[4^1 5^4 6^2]$ cage	1.84 Å	Single crystal	25
[tMAda,F]-STT SSZ-23	$[4^3 5^4]$ cage	Average of 1.95 Å	Microcrystal XRD	21
[BzQ,F] ITQ-4	$[4^3 5^2 6^1]$ cage	1.92 Å	Microcrystal XRD at 30 K	6
[F,DMABO]-STF ITQ-9	$[4^1 5^2 6^2]$ cage	1.87 Å	Microcrystal XRD	14
[F,DMABO]-ITE ITQ-3	$[4^4 5^3]$ cage	1.92 Å	Microcrystal XRD	This thesis Chapter 4

Table 5.1 Location of fluoride ions in zeolites and clathrasils from X-ray diffraction data.

The local structure of the $[SiO_{4/2}F]^-$ units reported by X-ray diffraction, is often not the true local structure but is an average between $[SiO_{4/2}F]^-$ and $SiO_{4/2}$ units, due to the incomplete occupancy of the fluoride ions in the form of either static or dynamic disorder (Figure 5.1).[12,17] This disorder often leads to the reporting of an average F-Si bond distance, which is much longer (between 1.84 – 1.99 Å) than the real distance in the five coordinate species.
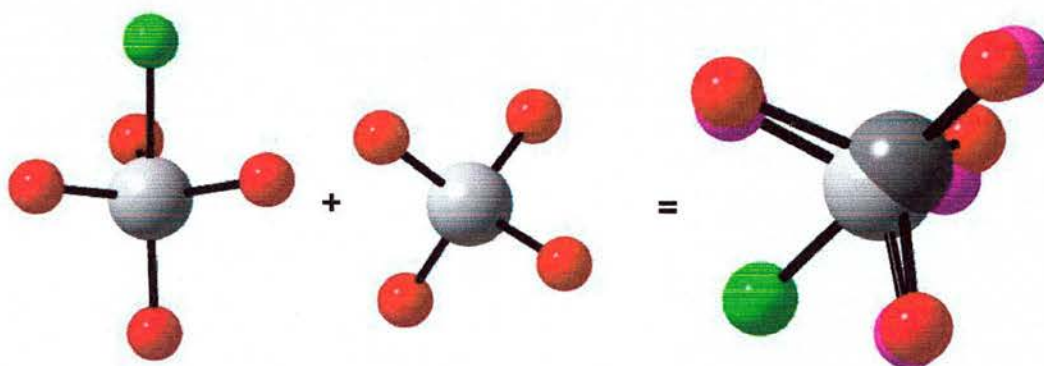

Figure 5.1 Diagrammatic representation of the five coordinate $[SiO_{4/2}F]^-$ unit, a standard tetrahedral SiO_4 unit and the combined average structure, as 'seen' by X-ray diffraction.

Attfield *et al.* recognised that the F-Si bond distances reported by X-ray diffraction were longer than expected.[26] They performed density functional theory calculations on fluoride ions in both SOD and FER frameworks. This showed that the $[SiO_{4/2}F]^-$ units are very close to trigonal bipyramidal with F-Si bond distances (1.71 Å and 1.76 Å) much shorter than those obtained from X-ray diffraction.

Fyfe *et al.* have used a variety of solid state NMR techniques to locate and measure the F-Si distance in octadecasil (AST),[27] silicalite-1 (MFI)[18,28] and ITQ-9 (STF).[12] Solid state NMR is an excellent probe of the local ordering within a material and can be used to accurately determine the F-Si distance in the $[SiO_{4/2}F]^-$ units, and will not

be affected by the averaging problems of either incomplete occupancy or disorder that often effect XRD.[12]

Solid state NMR and X-ray diffraction can be highly complementary techniques for the study of disordered systems, such as fluoride containing zeolites.[12,18]

5.1.1 Measuring F-Si Internuclear Distances Using MAS NMR

MAS NMR is well established as a useful and accurate method of determining internuclear distances within a material. Several methods have been employed, taking advantage of both the dipolar interactions and the *J*-coupling between atoms.[29,30] Much of the work in determining the F-Si internuclear distances in zeolites has been performed by Fyfe *et al.* although many other groups have performed similar measurements in a wide range of materials. Cross polarization,[31-33] Rotational Echo Double Resonance (REDOR)[34] and Transferred Echo Double Resonance (TEDOR)[35,36] experiments have all been used to probe the heteronuclear dipolar couplings between isolated $^{19}F/^{29}Si$ spin pairs in octadecasil,[27,37] silicalite-1[18] and ITQ-9,[12] The work in this chapter involves the use of cross polarization to measure the F-Si internuclear distances in pure silica zeolites.

5.1.1.1 Cross Polarization

As described in Chapter 2, the cross polarization experiment was originally developed to overcome the problems of the low sensitivity of rare spins (S), which have low gyromagnetic ratios.[31,32,38] This can be achieved in materials that contain

abundant spins (I) such as ^{1}H or ^{19}F, where the polarization is transferred from the I spins to the S spins via the dipolar interactions.

Efficient polarization transfer for a sample containing strongly homonuclear coupled I spins occurs when the Hartmann-Hahn matching condition, $\omega_{1I}=\omega_{1S}$, is satisfied and the CP matching profile consists of a very broad peak centred at $\omega_{1I}=\omega_{1S}$.[31] In a spin system in which the homonuclear dipolar coupling between the I spins is reduced, the CP matching profile splits into a series of sideband matching conditions, where the peaks are separated by the spinning frequency.[33,38,39] In a system containing isolated I-S spin pairs the polarization shuttles between the I and S nuclei and a plot of signal intensity as a function of contact time results in oscillations being observed in the CP curves. The CP matching profile for an isolated I-S spin pair consists of four peaks at $\Delta = \omega_{1I}-\omega_{1S} = n\omega_r$, where n = ±1 or ±2 and ω_r is the spinning rate.
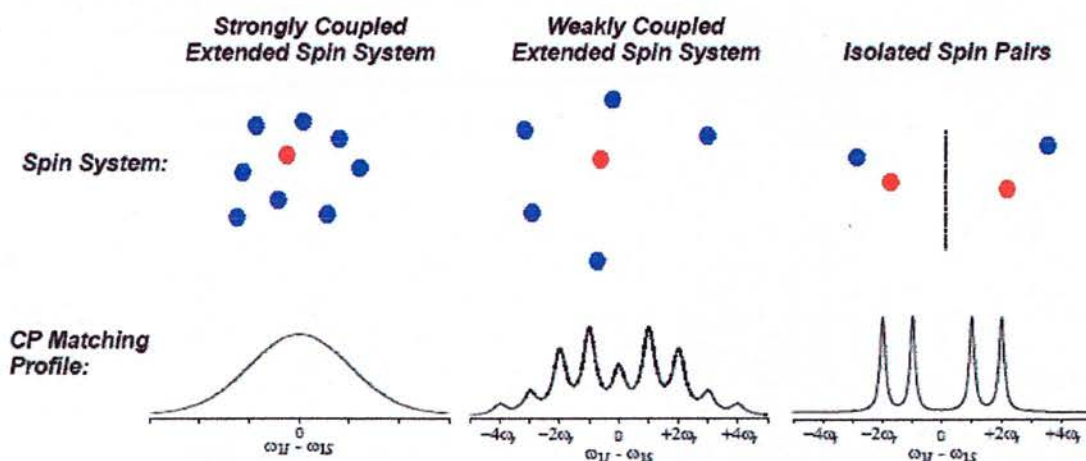

Figure 5.2 CP matching profiles for a strongly coupled extended spin system, a weakly coupled extended spin system and an isolated spin pair system. Redrawn from ref 24.

Oscillations in CP intensity for an isolated I-S spin system were first reported by Müller *et al.* on a non-spinning single crystal of ferrocene.[40] It has since been shown that the frequency of the oscillations is related to the dipolar coupling[41] and this can give valuable structural information. Since this original work, there have been many investigations in to the theoretical basis for heteronuclear distance determinations using CP MAS NMR.[33,39] The results of these have been employed several times for the analysis of internuclear distances, particularly for the F-Si distance in octadecasil.[27,37,42-44] The details of the theoretical basis of heteronuclear distance determinations by CP MAS NMR are beyond the scope of this thesis. For further details on this subject the reader is directed to the publications by Hediger *et al.*[33] and Marica *et al.*[45]

As previously mentioned, other MAS NMR experiments have been developed to allow the heteronuclear dipolar coupling to be determined. These include both REDOR and TEDOR experiments, which have previously been used to determine the F-Si distance in octadecasil. Fyfe *et al.* have performed a comparative study of REDOR, TEDOR and CP experiments on octadecasil in order to determine the best method for accurate distance determinations in zeolites.[30] Their work has revealed that all three of these techniques have both their advantages and disadvantages. They concluded that REDOR and TEDOR are affected by finite pulse lengths, r.f. field inhomogeneities and variations in the spinning speed, all of which lead to the measurement of a larger dipolar coupling. The CP experiments are, however, much harder to set up than either REDOR or TEDOR due to the excessive sensitivity of the CP matching condition especially at fast spinning rates. As CP leads not only to recoupling but also to polarization transfer, there is no need for normalisation as there

is for REDOR. Hence, unwanted signals from uncoupled I and S spins are eliminated in CP and TEDOR experiments.[42]

An alternate CP based experiment has recently been reported by Fyfe *et al.* for the determination of the heteronuclear dipolar coupling.[12] This method involves the extraction of the isotropic peaks and the spinning sidebands of the five coordinate $[SiO_{4/2}F]^-$ species from a $^{29}Si\{^1H\}$ CP MAS experiment collected at a relatively slow spinning speed (typically < 3 kHz). The experiment is easier to set-up and optimise than a $^{29}Si\{^{19}F\}$ CP MAS experiment, as the CP match condition is significantly broader. To accurately determine a distance using any of the other MAS NMR experiments requires the presence of an isolated I-S spin pair. This is, however, not necessary for the slow spinning CP MAS NMR experiment, since the dipolar coupling is measured through the *J*-coupling interactions. Therefore, slow spinning CP MAS NMR will mainly be used for the determination of F-Si internuclear distances in this chapter.

5.1.2 [DECDMP,F]-SFF (SSZ-44)

5.1.2.1 Description of the SFF Framework

The SFF framework topology was first described by Wagner *et al.* in 1999 using powder X-ray diffraction data of a sample produced using the hydroxide method.[46] The structure contains one-dimensional channels that alternate in size from a 10 MR to a contorted 18 MR, which run along the [001] direction. The periodic building unit of the frameworks is a layer like unit, which is composed of sixteen tetrahedral atoms and is formed from two fused $[4^35^26^1]$ cages as seen in Figure 5.3b. The SFF structure

(Figure 5.3a) can be seen as stacked layers of these units each related through a mirror plane. Recently Villaescusa *et al.* reported a zeolite with SFF topology, synthesised using fluoride ions as the mineralising agent and DECDMP cations as a SDA.[47,48] The structure of the as-made version of this material could not be determined as the sample consisted of very small (15 x 8 x 5 μm) crystals, and was too complicated to be solved by powder diffraction methods.

5.1.2.2 Microcrystal X-ray Diffraction Study of SSZ-44

The crystals of the as-synthesised [DECDMP,F]-SFF sample, which were synthesised as reported in Chapter 3.2.2.5, were too small (20 x 30 x 20 μm) for analysis on a standard laboratory diffractometer and were, therefore, analysed using synchrotron radiation at Station 9.8 of the Daresbury SRS.[49]

The structure of the as-made [DECDMP,F]-SFF sample was solved by direct methods (SHELXS-97)[50] and refined with a full-matrix least-squares technique (SHELXL-97)[51] using the WinGX[52] suite of programs.

The refinement of the model against the X-ray diffraction data for [DECDMP,F]-SFF suggested a monoclinic spacegroup $P2_1/m$, with unit cell parameters of $a=$ 7.3944(8) Å, b = 21.917(2) Å, $c=$ 11.3200(12) Å and $\beta=$ 94.498(2)°. Full details of the data collection and the refinement parameters can be seen in Table 5.2, and the details of the structure determination can be found on the attached CD as Crystallographic Information Files.

The crystals were not of the highest quality and were very small, even for a synchrotron microcrystal X-ray diffractometer, and this led to only the Si-O-Si framework and the fluoride ions being located and refined. Several attempts were

made to locate the template molecules, although none of these were successful. The Fourier peaks for the template molecules were removed from the refinement using the program SQUEEZE[53] and this significantly improved the overall refinement to give a final R-factor of 5.2% and a weighted R-factor of 0.13.

Identification code	[DECDMP,F]-SFF	
Empirical formula	$Si_8O_{16}F_{1.33}C_8H_{10}N$	
Formula weight	626.22	
Temperature	150(2) K	
Wavelength	0.69424 Å	
Crystal system	Monoclinic	
Space group	P21/m	
Unit cell dimensions	A = 7.3944(8) Å	alpha = 90°
	B = 21.917(2) Å	beta = 94.498(2)°
	C = 11.3200(12) Å	gamma = 90°
Volume	1828.9(3) Å^3	
Z, Calculated density	3, 1.706 Mg/m^3	
Absorption coefficient	0.433 mm^{-1}	
F(000)	951	
Crystal size	0.015 x 0.008 x 0.005 mm	
Theta range for data collection	1.76 to 20.31°	
Limiting indices	-7<=h<=7, -21<=k<=20, -11<=l<=11	
Reflections collected / unique	5729 / 1981 [R(int) = 0.0449]	
Completeness to theta = 20.31	100.0 %	
Absorption correction	None	
Refinement method	Full-matrix least-squares on F^2	
Data / restraints / parameters	1981 / 0 / 229	
Goodness-of-fit on F^2	0.984	
Final R indices [I>2sigma(I)]	R1 = 0.0526, wR2 = 0.1348	
R indices (all data)	R1 = 0.0673, wR2 = 0.1431	
Largest diff. Peak and hole	0.652 and -0.535 e.Å^{-3}	

Table 5.2 Crystal data and structure refinement for [DECDMP,F]-SFF.

The Si-O-Si framework of [DECDMP,F]-SFF is in excellent agreement with that described by Wagner *et al.* and consists of 8 crystallographically distinct silicon sites. The fluoride ions were found to be disordered over two equivalent sites in the fused $[4^1 5^2 6^2]$ cages. The local environment around one of the fluoride ions is shown in Figure 5.3b, giving rise to 16 tetrahedral sites (T-sites) and not the eight T-sites seen in the asymmetric unit due to the fluoride disorder. This disorder of the fluoride ions gives a F-Si bond distance of 1.89(2) Å, which is greater than the true bond distance.
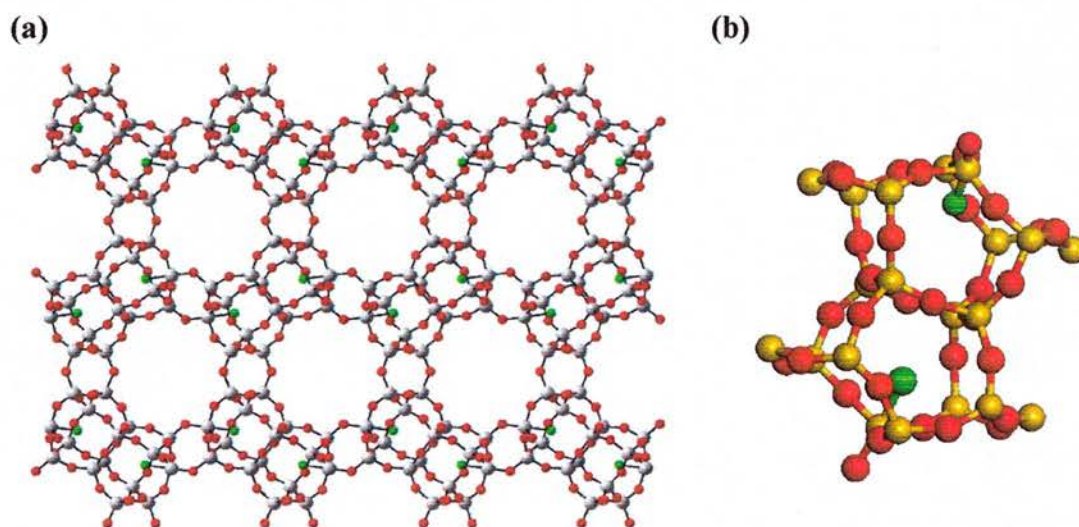
(a)   **(b)**

Figure 5.3 (a) [DECDMP,F]-SFF structure, showing the location of the fluoride ions but not the template molecules. (b) The two fused $[4^1 5^2 6^2]$ cages, which are the periodic building unit of SFF.

5.1.2.3 $^{29}Si\{^1H\}$ CP MAS NMR

The fast spinning (12 kHz) $^{29}Si\{^1H\}$ CP MAS spectrum of [DECDMP,F]-SFF is shown in Figure 5.4a. Although the sample was not of the highest quality, it is still possible to resolve many of the peaks by eye, and the spectrum can be deconvoluted in

to sixteen peaks of equal intensity. The sixteen peaks observed in the $^{29}Si\{^1H\}$ CP spectrum seem, initially, to be inconsistent with the eight crystallographically distinct silicon atoms determined from the XRD data. This is because X-ray diffraction probes the long-range order of a material and hence the results indicate the spatially averaged symmetry.[12] NMR probes the local structure of a material and, therefore, the true local symmetry of the $[4^15^26^2]$ cages is in fact lower than that determined from the crystal structure due to the fluoride disorder. The $^{29}Si\{^1H\}$ CP MAS NMR spectrum indicates that the fluoride ions are only in one of the $[4^15^26^2]$ cages of the fused pair and have full occupancy.

Although the spectrum shown in Figure 5.4a is a $^{29}Si\{^1H\}$ CP spectrum it is expected to be close to quantitative, as there are many ^1H nuclei well distributed throughout the structure, and each silicon site is on the surface of the SDA-containing channel. The short $^1H\ T_1$ relaxation time (~1.2 s) makes the CP experiment much more efficient than a ^{29}Si MAS NMR experiment, which although would be completely quantitative would take a long time to perform due to $^{29}Si\ T_1$ being ~80 s. An important detail in the $^{29}Si\{^1H\}$ CP MAS spectrum is the two peaks centred at – 147 ppm. These two peaks are in fact doublet produced by the $^{19}F/^{29}Si$ *J*-coupling (160 Hz) through the F-Si bond. This gives clear evidence of the presence of a covalent bond between the fluoride ion and the silicon framework, and shows that the fluoride disorder is static and not dynamic as seen for ITQ-4 and MFI.[17,18]
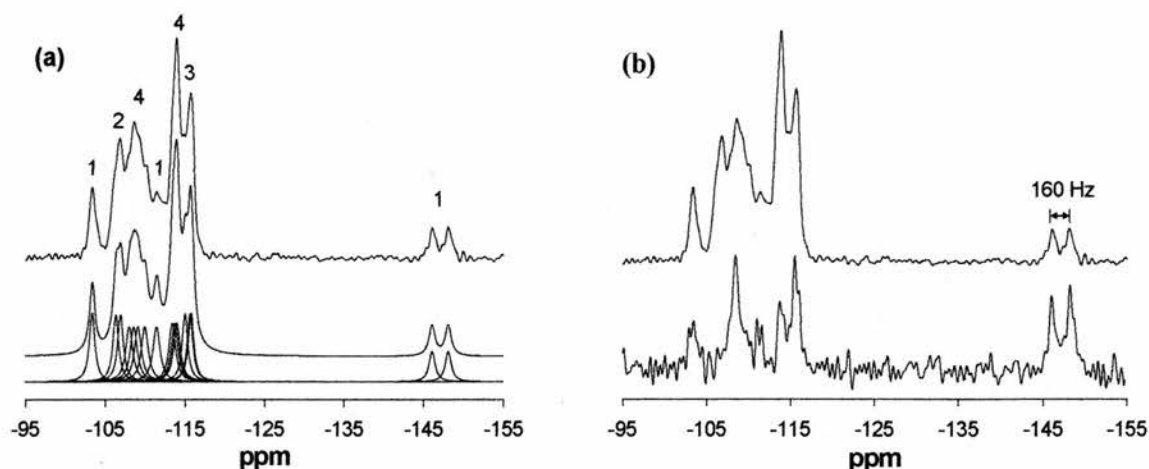
Figure 5.4 (a) Deconvolution of the ^{29}Si{^{1}H} CP MAS spectrum (12 kHz spin rate) of [F,DECDMP]-SFF with 16 peaks of equal area. (b) Comparison of the ^{29}Si{^{1}H} CP MAS spectrum (upper) and ^{29}Si{^{19}F} CP MAS spectrum (lower) collected at 12 kHz spin rate. The ^{29}Si{^{19}F} contact time was 1 ms.

5.1.2.4 Measurement of the F-Si Distance by MAS NMR

The ^{19}F/^{29}Si dipolar coupling and hence the F-Si internuclear distance in [DECDMP,F]-SFF were measured using two techniques. The first of these involved collecting a series of ^{29}Si{^{19}F} CP MAS experiments at variable contact times, whilst spinning at 12 kHz. The peak area for the five-coordinate silicon species (the *J*-coupled doublet) was then plotted as a function of contact time, as shown in Figure 5.5. Fyfe *et al.* and Bertani *et al.* have shown that in the case of isolated spin pairs, the CP curves will show an oscillation at a frequency that is proportional to the ^{19}F/^{29}Si dipolar coupling.[27,37]

$$< S_n > (t) = I_0 \{(x) S_{isolated} + (1-x) S_{network}\} \qquad \text{Equation 5.1}$$

$$= I_0 \{(x) \tfrac{1}{2}(e^{-k_I t} - e^{k_s t} g_n(t)) + (1-x) \frac{k_{IS}}{k_{IS}+k_I}(e^{-k_I t} - e^{k_{IS} t})\}$$

Fitting the oscillations of the contact time curve, using Equation5.1, gave an effective dipolar coupling constant of 4.30 ± 0.15 kHz. The effective dipolar coupling is related to the dipolar coupling by D' = D - $\Delta J/3$, but assuming the anisotropy in *J* is small ($\Delta J \approx 0$), a F-Si internuclear distance of 1.74 ± 0.02 Å can be calculated using:

$$D = \frac{\mu_0 \gamma_{Si} \gamma_F h}{16\pi^3 r_{F-Si}^3}$$

Equation 5.2

Five periods of oscillation were observed and fit for the ^{29}Si{^{19}F} variable contact time experiments and it is believed that the errors in the determined ^{19}F/^{29}Si dipolar coupling and the F-Si internuclear distance are quite small.
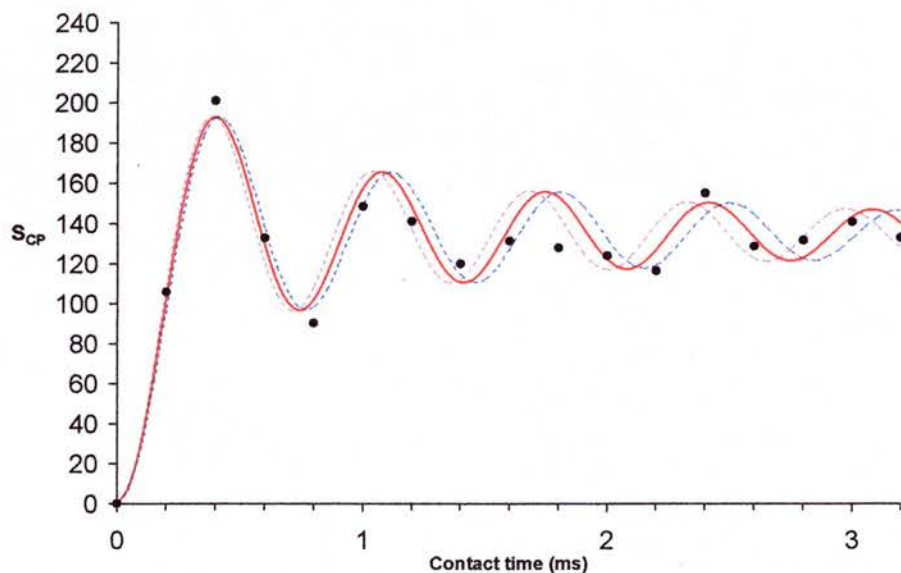

Figure 5.5 Experimental and simulated ^{29}Si{^{19}F} CP curves for the five-coordinate Si of [F,DECDMP]-SFF at the +1 spinning sideband matching condition with a 12 kHz spin rate (80 scans per spectrum, 15 s recycle time). The data were fitted with a dipolar coupling of 4.30 ± 0.15 kHz, corresponding to a F–Si internuclear distance of 1.74 ± 0.02 Å. The solid line (red) is the best fit and the dashed lines represent estimates of the error limits.

The second method of measuring the $^{19}F/^{29}Si$ dipolar coupling and the F-Si internuclear distance was obtained by fitting the spinning sideband profiles in a slow-spinning (1.9 kHz) $^{29}Si\{^1H\}$ CP MAS spectrum. At relatively slow spin rates (<3.0 kHz) the peaks of *J*-coupled doublet centred at −147.0 ppm no longer have equal intensities. This observation was first made by Koller *et al.* for the pure silica zeolites [DMABO,F]-ITE, and [tPABr,F]-MFI at low temperature.[17] Figure 5.6a shows the $^{29}Si\{^1H\}$ CP MAS spectrum collected at spin rate of 1.9 kHz. Extraction of all the spinning sidebands for each of the peaks of the doublet are shown in Figure 5.6b, and as expected, the total intensities are equal. The two isotropic peaks have different intensities because the effective chemical shift anisotropy (CSA) tensors are quite different. The spinning sideband manifolds can be simulated well assuming an axially symmetric CSA tensor ($\eta=0$) with effective shielding anisotropy values of 9.8 ± 0.2 kHz and 2.0 ± 0.2 kHz for the isotropic peaks with the chemical shifts of −146.0 and −148.1 ppm respectively (Figure 5.6c). The errors reported for these values are estimates and were determined by comparing CSA patterns simulated with different δ'_{aniso} values to the experimental spectrum.
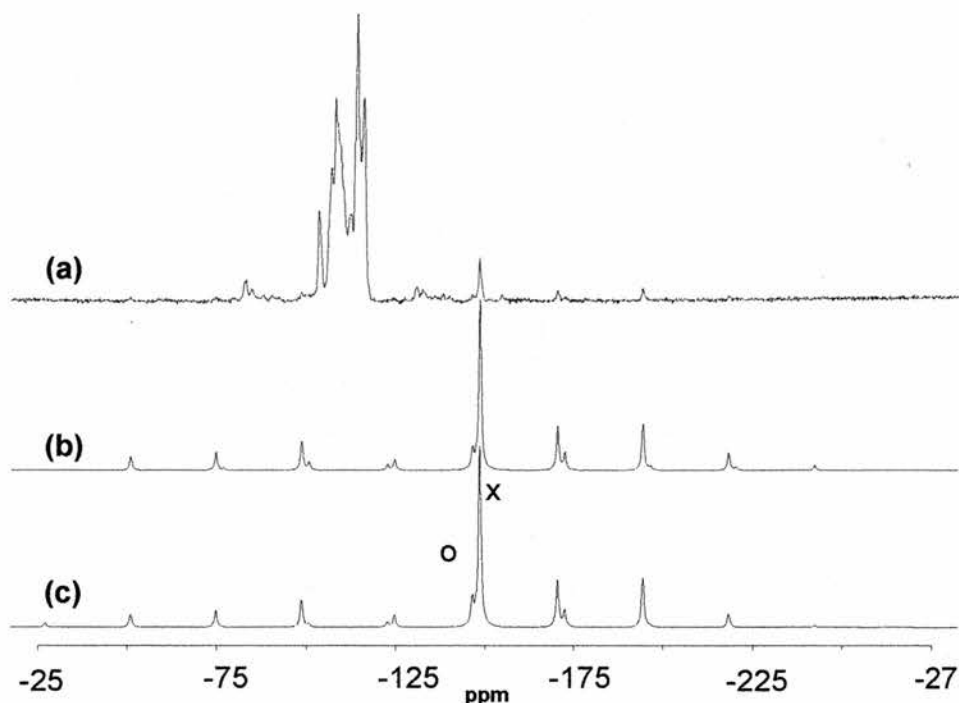
Figure 5.6 Slow spinning (1.9 kHz) ^{29}Si{^{1}H} CP MAS spectra of [F,DECDMP]-SFF. (a) ^{29}Si{^{1}H} CP MAS spectrum with 3 ms contact time (48000 scans, 3 s recycle time). (b) Isotropic and spinning sidebands of the five-coordinate peak extracted from the ^{29}Si{^{1}H} CP MAS spectrum; intensity scaled by a factor of 4 relative to spectrum a. (d) Simulated effective CSA patterns of the doublets of the five-coordinate peak: (x) δ_{iso} = -148.1 ppm, δ'_{aniso} = 2.0 kHz, η = 0; (o) δ_{iso} = -146.0 ppm, δ'_{aniso} = 9.8 kHz, η = 0.

The difference in δ'_{aniso} values for each of the peaks of the doublet is due to the interplay between the chemical shift anisotropy, dipolar coupling and the *J*-coupling tensors.[54-56] Assuming the tensors are collinear along the F-Si bond and that the CSA tensor is axially symmetric, the effective chemical shift anisotropy (δ'_{aniso}) depends on the actual shielding anisotropy (δ_{aniso}), dipolar coupling, anisotropy in J ($\Delta J = J_{\parallel} - J_{\perp}$), and the spin state of the nuclei (m = $\pm$ ½):

$$\delta'_{aniso} = \delta_{aniso} - 2mD' = \delta_{aniso} \pm D' \qquad\qquad \text{Equation 5.3}$$

where the effective dipolar coupling is D'= D-ΔJ/3.

Using the δ'_{aniso} values determined from the ^{29}Si{^{1}H} CP MAS spectrum, the δ_{aniso} can be calculated to be 5.9 ± 0.4 kHz and the effective dipolar coupling, D' = 3.9 kHz. Using Equation 5.2, D = $(\mu_0\gamma_{Si}\gamma_F h)/(16\pi^3 r_{F-Si}^3)$, and assuming that the anisotropy in *J* (ΔJ) ≈ 0, the F-Si internuclear distance can be calculated to be 1.79 ± 0.06 Å The errors in the F-Si internuclear distance determined by the slow spinning experiment are probably larger than those from the variable contact time CP experiments due to the difficulties in fitting the sidebands accurately. The slow spinning sideband analysis method is, however, much easier to set up and does not require the very precise CP matching conditions that the ^{29}Si{^{19}F} variable contact time CP experiments do.

The values for the F-Si internuclear distance determined for [DECDMP,F]-SFF are in excellent agreement with previous studies on the related zeolite [DECDMP,F]-STF (1.74 – 1.79 Å)[12] and on [tPABr,F]-MFI (1.77 Å)[18] at low temperature by Fyfe *et al.* and also with predictions made from DFT calculations on fluoride containing FER and SOD frameworks by Attfield *et al.*(1.72 & 1.77 Å).[26]

5.1.2.5 Re-examination of the XRD Refinement

Both of the MAS NMR experiments have enabled the accurate measurement of the F-Si internuclear distance and have shown it to be significantly smaller than the 1.89(2) Å determined from the X-ray diffraction structure. This has enabled the XRD refinement to be revisited in order to resolve the disorder of the silicon sites.

Refinement of the disordered model with two resolved silicon sites (Si5A and Si5B) was stable and gave a F-Si distance of 1.757(3) Å, which is in very good agreement with the two values (1.74 and 1.79 Å) calculated by MAS NMR. The splitting of the silicon sites also enabled the oxygen sites to be resolved to give four oxygen atoms in each of the coordination spheres of both Si5A and Si5B. This refinement resulted in a slightly distorted trigonal bipyramidal $[SiO_{4/2}F]^-$ unit and a similarly distorted tetrahedral $SiO_{4/2}$ unit. Attempts to restrain the geometry of the trigonal bipyramidal and tetrahedral units produced an unstable refinement, indicating that the XRD experiment is not of sufficient resolution to enable this disorder to be fully resolved. The bond lengths and angles for both the distorted trigonal bipyramidal and tetrahedral silica units are given in Table 5.3.
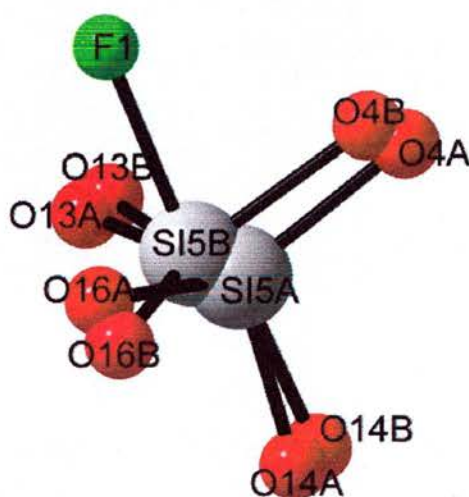

Figure 5.7 Local structure around the $[SiO_{4/2}F]^-$ and $SiO_{4/2}$ units in [DECDMP,F]-SFF

Si5B (5-coordinate [SiO$_{4/2}$F]$^-$		Si5A (Tetrahedral SiO$_{4/2}$)	
Si(5B)-F(1)	1.76(3)	Si(5A)-O(14A)	1.51(4)
Si(5B)-O(13B)	1.55(4)	Si(5A)-O(4A)	1.57(4)
Si(5B)-O(16B)	1.56(4)	Si(5A)-O(16A)	1.66(3)
Si(5B)-O(4B)	1.60(4)	Si(5A)-O(13A)	1.72(4)
Si(5B)-O(14B)	1.82(3)		
O(13B)-Si(5B)-O(4B)	107(2)	O(14A)-Si(5A)-O(4A)	114.0(14)
O(16B)-Si(5B)-O(4B)	114(2)	O(14A)-Si(5A)-O(16A)	106(2)
O(13B)-Si(5B)-O(16B)	136(2)	O(4A)-Si(5A)-O(16A)	115(2)
O(13B)-Si(5B)-O(14B)	96(2)	O(14A)-Si(5A)-O(13A)	104(2)
O(16B)-Si(5B)-O(14B)	97(2)	O(4A)-Si(5A)-O(13A)	116(2)
O(4B)-Si(5B)-O(14B)	96.7(13)	O(16A)-Si(5A)-O(13A)	100.7(14)
F(1)-Si(5B)-O(14B)	171(2)		
O(13B)-Si(5B)-F(1)	86.1(17)		
O(16B)-Si(5B)-F(1)	87.7(16)		
O(4B)-Si(5B)-F(1)	74.4(17)		

Table 5.3 Bond distances and angles for the 5-coordinate [SiO$_{4/2}$F]$^-$ species and the tetrahedral [SiO$_{4/2}$] species.

The value of the F-Si bond distance determined as a result of the isotropic refinement of [DECDMP,F]-SFF has confirmed that MAS NMR can be used to accurately determine internuclear distances, and the results from these experiments are in excellent agreement with the DFT calculations on FER and CHA by Attfield *et al.*[26] and the combined MAS NMR and XRD studies on [DECDMP,F]-STF by Fyfe *et al.*.[12]

5.1.3 [F,DMASD]-STF (Mu-26)

5.1.3.1 Description of the Structure

The synthesis and initial structural solution of [F,DMASD]-STF was reported by

Harbuzaru *et al.* in 2002.[13] The STF framework topology is related to the SFF

framework and was first solved from powder XRD data by Camblor *et al.*[57] and

independently confirmed by Wagner *et al.*[46] Like the SFF framework, STF contains

one-dimensional pores that run along the [001] direction with a 10-MR opening. The

periodic building unit for STF is the same as for SFF and consists of two-fused

$[4^15^26^2]$ cages. The main difference between the STF and SFF framework topologies

is how these periodic building units are stacked. In the STF type framework these

units are related to each other through inversion centres, whilst in SFF the layers are

related through mirror planes.

As with many zeolites, [DMASD,F]-STF does not seem to be able to be grown as

single crystals; instead the sample always consists of interpenetrating very fine

needles, which cannot be separated. Therefore, the framework structure of

[DMASD,F]-STF was solved using powder X-ray diffraction data, in the triclinic

spacegroup P1, and confirmed by the presence of sixteen peaks of equivalent intensity

in ^{29}Si MAS NMR.

As [DMASD,F]-STF cannot be grown as single crystals, any information that can

be gained about its structure from NMR will be advantageous, as will the opportunity

to confirm the F-Si distance in another pure silica zeolite thus confirming previous

results and experimental methods.

5.1.3.2 ^{29}Si{^{1}H} CP MAS NMR

The fast spinning (15 kHz) ^{29}Si{^{1}H} CP MAS NMR spectrum of [DMASD,F]-STF

is shown in Figure 5.8. The high resolution of the spectrum indicates the high quality

of the sample and the lack of structural defects. The spectrum can easily be resolved

in to 11 peaks, and deconvolution of the spectrum shows that there are 16 peaks of
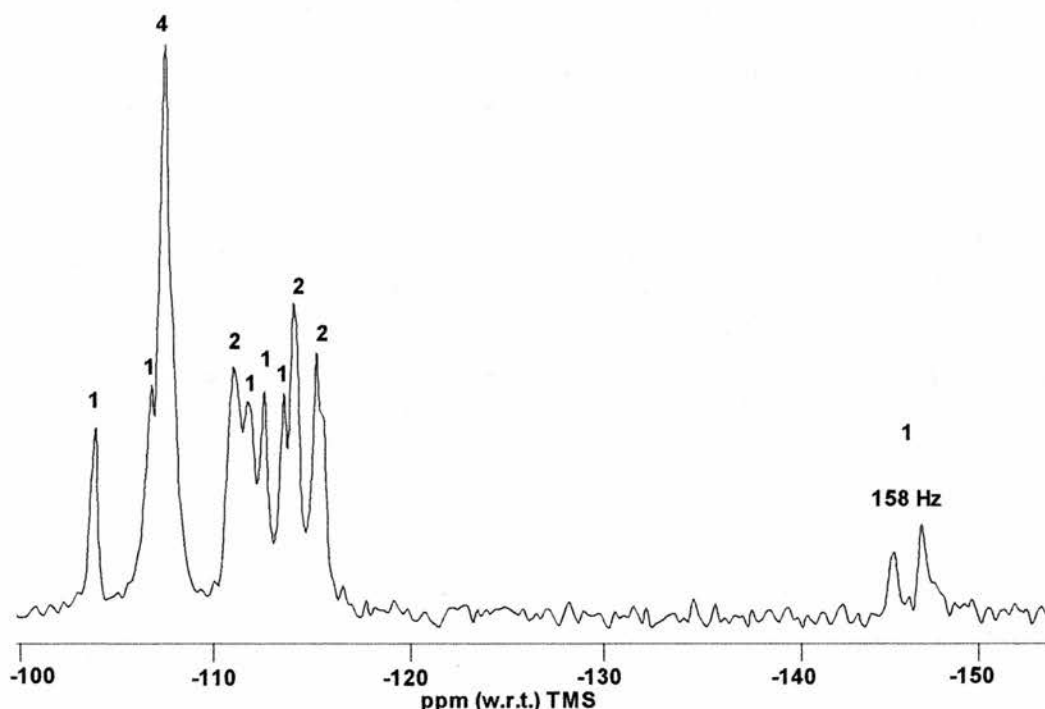
equal intensity.

Figure 5.8 ^{29}Si{^{1}H} CP MAS spectrum at 12 kHz spin rate and a contact time of 3 ms (512 scans, 3 s recycle time) of [F,DMASD]-STF. The numbers above the peaks correspond to the actual number of resonances determined from the deconvolution.

The spectrum shows the *J*-coupled doublet of the five coordinate silicon, [SiO$_{4/2}$F]$^-$,

centered at -147.6 ppm with the two peaks of the doublet having almost equal

intensity. In a similar way to the ^{29}Si{^{1}H} CP MAS spectrum of [DECDMP,F]-SFF

the ^{29}Si{^{1}H} CP spectrum of [DMASD,F]-STF can be treated as almost quantitative,

due to the presence of a large number of protons distributed throughout the structure. The ^{29}Si MAS NMR spectrum collected by Harbuzaru *et al.*[13] compares well to the CP spectrum, with both containing 16 resonances. Harbuzaru *et al.* interpreted these 16 peaks to correspond to the 16 crystallographically distinct silicon sites required for P1 symmetry and thus confirming their initial powder XRD refinement.

However, remembering that MAS NMR probes the local structure of a material and that XRD gives the spatially averaged symmetry, it is not believed that their proposed spacegroup for [DMASD,F]-STF is necessarily correct. The 16 resonances observed in the ^{29}Si spectra could correspond to the local structure of the double $[4^{1}5^{2}6^{2}]$ cages as seen previously in [DECDMP,F]-SFF, in which the disorder produced by the fluoride ions is not observed. In [DECDMP,F]-SFF and [DMABO,F]-STF[12] the fluoride ions only occupy one of the $[4^{1}5^{2}6^{2}]$ cages, but both cages appear to be occupied in the XRD crystal structure. This is because XRD is a time and space averaged technique and, therefore, the crystal structures have only eight crystallographically distinct silicon atoms. This disorder is believed be present in [DMASD,F]-STF as no second harmonic signal could be detected from NLO experiments, indicating that the spacegroup is probably not noncentrosymmetric P1. The more likely symmetry is monoclinic, the same as that reported for the related material [DMABO,F]-STF.[12,14]

5.1.3.3 Measurement of the F-Si Distance by MAS NMR

The F-Si internuclear distance in [DMASD,F]-STF was determined using the slow

spinning sideband analysis method in a similar manner as for [DECDMP,F]-SFF.

This experimental method was chosen over that of the ^{29}Si$\{^{19}$F$\}$ CP variable contact

time experiments mainly due to the difficulties that can be faced in trying to get the

exact CP match at either ±1 spinning sideband.[30] The slow spinning sideband analysis

experiments are much easier to set-up and analyse and it was believed that performing

several of these experiments at varying spin rates would provide a more accurate F-Si

distance.

Three ^{29}Si$\{^1$H$\}$ CP MAS NMR spectra were collected at 2.3, 2.5 and 2.6 kHz spin

rates and these are shown in Figures 5.9a, 5.10a and 5.11a respectively. All three of

these spectra show the effects of the interplay between the CSA, dipolar coupling and

the *J*-coupling for the doublet of the pentacoordinate silicon species.[54-56] The spinning

sideband profiles of the doublet were then extracted from the ^{29}Si$\{^1$H$\}$ CP spectra are
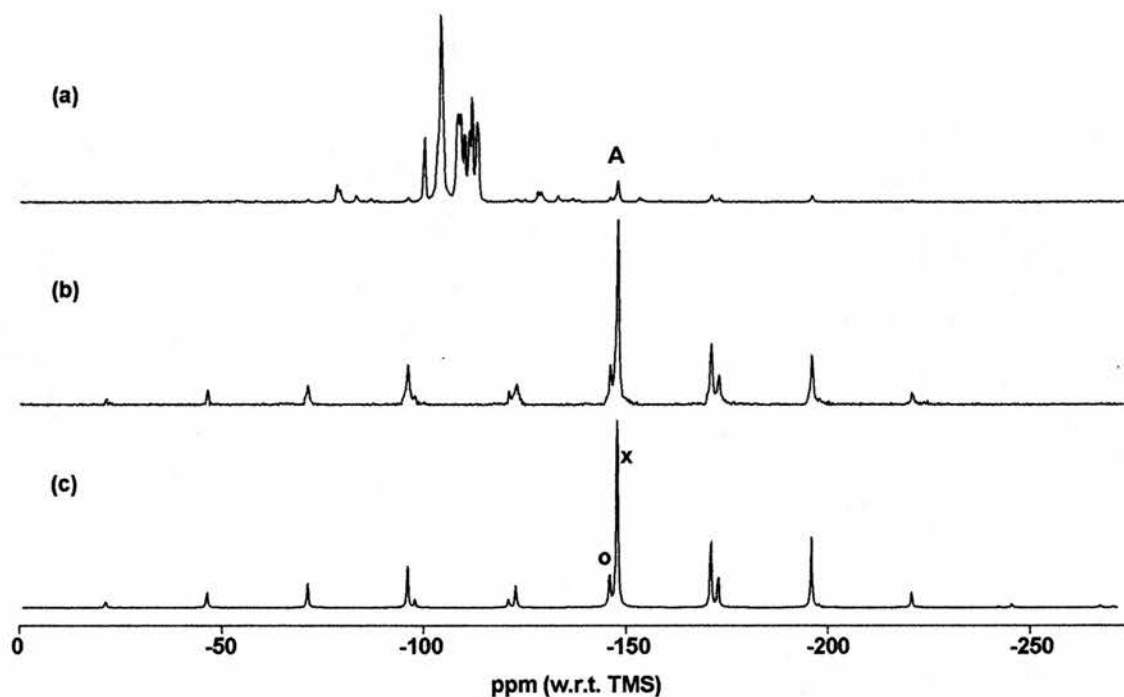
shown in Figure 5.9b - 5.11b.

Figure 5.9 Slow spinning (2.3 kHz) ^{29}Si{^{1}H} CP MAS spectra of [F,DMASD]-STF. (a) ^{29}Si{^{1}H} CP MAS spectrum with 5 ms contact time (38000 scans, 3 s recycle time). (b) Isotropic and spinning sidebands of peak A extracted from the ^{29}Si{^{1}H} CP MAS spectrum; intensity is scaled by a factor of 4 from spectrum a. (c) Simulated effective CSA patterns of the doublets of peak A: (x) δ_{iso} = -147.5 ppm, δ'_{aniso} = 3.0 ± 0.2 kHz, η = 0; (o) δ_{iso} = -145.6 ppm, δ'_{aniso} = 10.5 ± 0.2 kHz, η = 0.
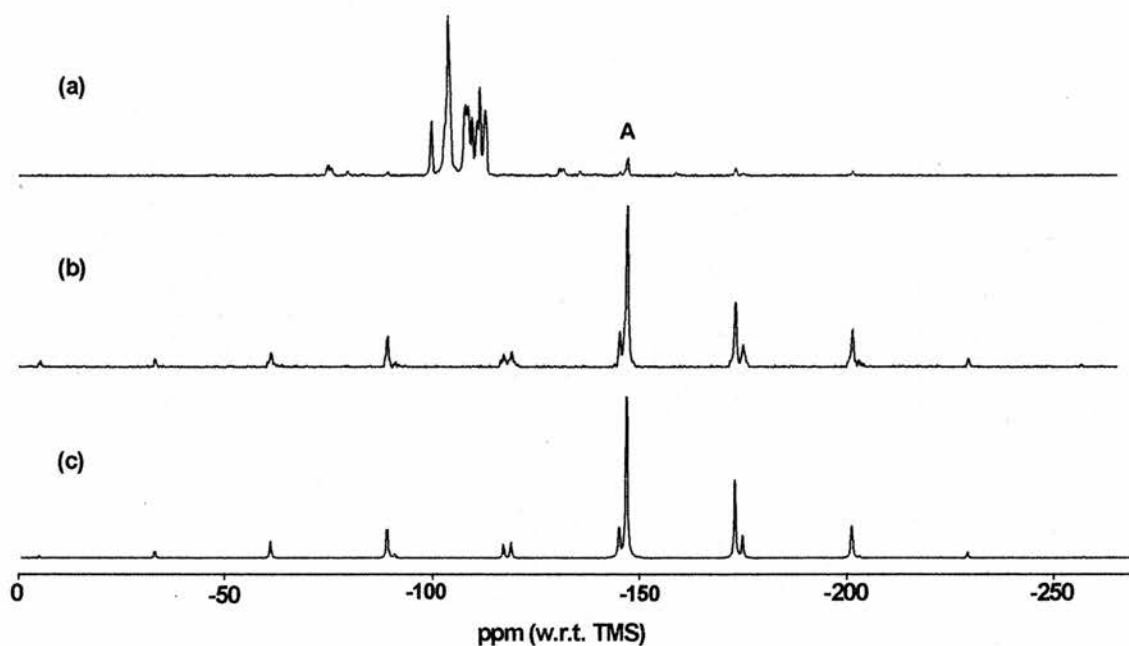
Figure 5.10 Slow spinning (2.5 kHz) ^{29}Si$\{^{1}$H$\}$ CP MAS spectra of [F,DMASD]-STF. (a) ^{29}Si$\{^{1}$H$\}$ CP MAS spectrum with 5 ms contact time (38000 scans, 3 s recycle time). (b) Isotropic and spinning sidebands of peak A extracted from the ^{29}Si$\{^{1}$H$\}$ CP MAS spectrum; intensity is scaled by a factor of 4 from spectrum a. (c) Simulated effective CSA patterns of the doublets of peak A: (x) δ_{iso} = -147.7 ppm, δ'_{aniso} = 3.2 $\pm$ 0.2 kHz, η = 0; (o) δ_{iso} = -145.9 ppm, δ'_{aniso} = 11.2 $\pm$ 0.2 kHz, η = 0.

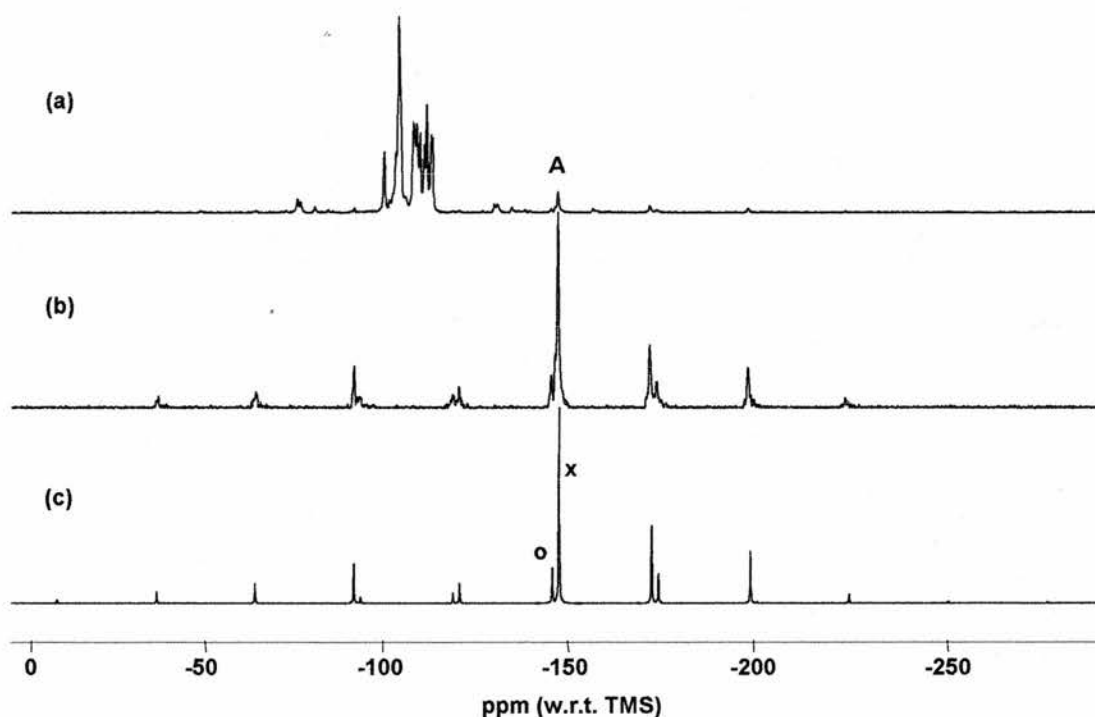Figure 5.11 Slow spinning (2.6 kHz) ^{29}Si{^{1}H}CP MAS spectra of [F,DMASD]-STF. (a) ^{29}Si{^{1}H} CP MAS spectrum with 5 ms contact time (38000 scans, 3 s recycle time). (b) Isotropic and spinning sidebands of peak A extracted from the ^{29}Si{^{1}H} CP MAS spectrum; intensity is scaled by a factor of 4 from spectrum a. (c) Simulated effective CSA patterns of the doublets of peak A: (x) δ_{iso} = -147.7 ppm, δ'_{aniso} = 3.0 ± 0.2 kHz, η = 0; (o) δ_{iso} = -146.1 ppm, δ'_{aniso} = 10.8 ± 0.2 kHz, η = 0

The spinning sideband manifolds can be simulated well assuming an axially symmetric CSA tensor (η=0) with the effective shielding anisotropy values showed in Table 5.4. Using these effective shielding anisotropy values and Equation 5.3 the effective dipolar couplings were calculated, and from these the F-Si internuclear distances were derived assuming ΔJ=0. The values for the effective dipolar couplings and the corresponding F-Si internuclear distances are also shown in Table 5.4.

Spin rate	δ'_{aniso} for peak o	δ'_{aniso} for peak x	δ_{aniso}	D'	F-Si distance
2.3 kHz	11.0 kHz	3.0 kHz	7.0 kHz	4.0 kHz	1.77 Å
2.5 kHz	11.2 kHz	3.2 kHz	7.2 kHz	4.0 kHz	1.77 Å
2.6 kHz	10.8 kHz	3.0 kHz	6.9 kHz	3.9 kHz	1.79 Å

Table 5.4 The effective shielding anisotropy values (δ_{aniso}), the effective dipolar couplings (D') and the F-Si internuclear distances for [DMASD,F]-STF at three different spin rates.

Taking the average of these F-Si distances for [DMASD,F]-STF gives a value of 1.78(2) Å, which is in excellent agreement with the values obtained for [DECDMP,F]-SFF and the previously published values for [DECDMP,F]-STF by Fyfe *et al.*[12]

5.1.4 Conclusions

The combination of MAS NMR and microcrystal X-ray diffraction has enabled the accurate location of the fluoride ions in as-synthesised zeolite [DECDMP,F]-SFF. The use of two MAS NMR experiments has resulted in two very similar values for the F-Si internuclear distance, both of which are significantly lower than the original results from the X-ray diffraction model. Re-examination of the crystal structure refinement incorporating terms to resolve the disorder has resulted in a F-Si distance of 1.757(3) Å, which is in almost perfect agreement with the values determined from MAS NMR. Unfortunately the XRD data was not of high-enough resolution to enable the refinement of the disordered template molecules or for the exact geometry of the fluoride containing silicon site to be determined. This will require the preparation of higher-quality single crystals, which may or may not be possible for this particular

zeolite. Without the use of MAS NMR to probe the local structure, the data from the XRD study could never be used alone, without some doubts about its accuracy.

The use of MAS NMR to study the local structure of the fluoride ions in [DMASD,F]-STF has resulted in a F-Si bond distance that is almost identical to those measured in a related STF sample and to those determined for [DECMP,F]-SFF. These results have shown that slow spinning sideband analysis is just as reliable as variable contact time CP, REDOR or TEDOR experiments for determining heteronuclear dipolar couplings in fluoride containing zeolites. The added advantages of the slow spinning sideband analysis method are the ease of experimental set up and optimisation and the short recycle times. The inability to grow single crystals of [DMASD,F]-STF and the inherent difficulties in solving structures purely from powder diffraction data means that diffraction techniques alone could not be relied upon to solve this structure accurately. The combination of MAS NMR and powder diffraction may, however, enable the structures of materials like [DMASD,F]-STF to be solved if sufficient dipolar couplings can be measured, as is discussed for silicalite-1 below.

5.2 Distance Determinations in Isotopically Labelled Silicalite-1

5.2.1 Introduction

The disorder of the fluoride ions within certain pure silica zeolites has just been discussed and it has been shown that the combination of microcrystal XRD and MAS NMR have enabled the structure of SSZ-44 to be more accurately determined. However, zeolite single crystals are notoriously hard to produce and in several cases it is impossible at present to produce single crystals, as seen for [F,DMASD]-STF (Mu-26).[13] This has previously meant that the only technique available for studying these structures has been powder diffraction. Solving a zeolite structure by powder diffraction methods is by no means trivial for materials that are as complex as some zeolites, even with state of the art structure solution programs.[58] Even when the structure of the framework can be determined, it is often impossible to accurately locate the guest molecules / SDAs within the zeolite channels.[59] The combination of the inability to synthesise high quality zeolite single crystals and then the difficulties faced solving structures from powder diffraction data has led to the consideration that MAS NMR could be used to solve zeolite crystal structures. It has already been shown that MAS NMR can be used to determine F-Si bond distances in intergrown samples such as Mu-26, and it is well established that 2-dimensional NMR techniques can be used to elucidate the connectivities in the silicate frameworks.[60] There are also an increasing number of reports of the complete structural determination of polypeptides and proteins using both solution state[61,62] and solid state NMR techniques[63] and, hence, it may be possible to perform similar experiments using MAS NMR to solve the structures of pure silica zeolites. To solve the structure of a zeolite

would require the determination of the framework connectivity using ^{29}Si Incredible Natural Abundance Double Quantum Transfer (INADEQUATE)[64,65] experiments and then the determination of internuclear distances between the framework, the fluoride ions and the templates (SDAs). These internuclear distances can be determined by measuring the dipolar coupling between isolated spins using cross polarization, TEDOR[66] and REDOR experiments.[30] All of these types of experiments have been successfully employed by Fyfe *et al.* for the determination of the fluoride location in [tPABr,F]-MFI (silicalite-1).[18,28]

Pure silica zeolites have a very well defined porous structure with few, if any, defects and this combined with the presence of isolated F-Si spin pairs makes them ideal candidates for structure solution using MAS NMR. There are, however, certain characteristics in a zeolite sample that need to be present to allow the collection of high resolution NMR spectra. The first, as already mentioned, is the need for incorporated fluoride ions, as ^{19}F is 100% abundant and has a high relative receptivity making it excellent for CP experiments. The second condition is the need for sharp resonances in the ^{29}Si NMR spectra, so that individual resonances can be determined. The final condition is that the SDA used to synthesise the zeolite needs to have a way of being isotopically labelled. This is because ^{13}C and ^{15}N both have low natural abundance and relative receptivities and therefore to effectively CP to either of these nuclei will require enrichment. Table 5.5 contains a list of all the known pure silica zeolites that satisfy all three of these conditions.
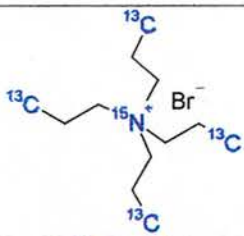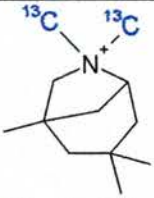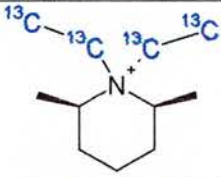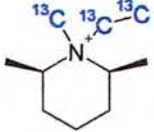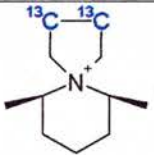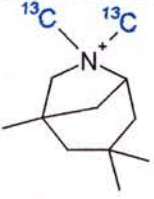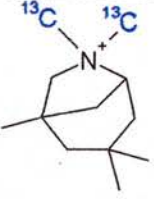
Zeolite	Template	
Silicalite-1[1]	Tetrapropylammonium Bromide (tPABr)	
ITQ-3[2]	1,3,3,6,6-pentamethyl-6-azonia-bicyclo[3.2.1]octane (DMABO)	
SSZ-44[47,48]	*N,N*-diethyl-2,6-dimethylpiperidinium (DECDMP)	
SSZ-35[14,48]	DECDMP or *N*-ethyl,*N*-methyl-2,6-dimethylpiperidinium	
Mu-26[13]	Cis-6,10-dimethyl-5-azonia-spiro[4.5]decane	
ITQ-9[57]	DMABO	
FER[15]	DMABO	

Table 5.5 Fluoride containing pure silica zeolites that show sharp resonances in their ^{29}Si MAS NMR and which are synthesised from SDAs that can be readily isotopically labelled, as shown in blue.

There have been several studies in to the structure of [tPABr,F]-MFI using both X-ray diffraction[67] and MAS NMR techniques.[18] Therefore, it was decided that [tPABr,F]-MFI (silicalite-1) would be the best zeolite to perform initial NMR structural determination experiments on, as a great deal more information is known about this material than any of the other potential zeolites. This would enable the NMR experimental results to be compared to the previously determined crystal structure for [tPABr,F]-MFI.

The aims of this work were to synthesise the pure silica zeolite silicalite-1 using an isotopically labelled SDA and then use MAS NMR to measure the internuclear distances between the fluoride ions and the labelled SDA and then also between the silicate framework and the SDA.

5.2.2 Results and Discussion

5.2.2.1 Synthesis

Two labelled [tPABr,F]-MFI samples were synthesised, one with 10% ^{15}N tPABr and the other with 100% ^{15}N tPABr. Both samples were synthesised using a similar method to that reported in Chapter 3.2.2.2. ^{15}N labelled tetrapropylammonium bromide was used, as this was commercially available from CDN Isotopes.

The 100% ^{15}N labelled sample of silicalite-1 was synthesised using ^{15}N isotopically enriched tetrapropylammonium bromide as a SDA, with a final gel composition of SiO_2: 0.08 tPABr: 0.5 NH_4F: 20 H_2O. In a typical synthesis tP(^{15}N)ABr (0.356 g, 1.33 mmol) and NH_4F (0.308 g, 8.32 mmol) were dissolved in distilled water (6 g, 0.33 mol). To this solution was added Cab-O-Sil (1 g, 16.65 mmol) and the mixture

thoroughly homogenised by hand. The resultant solution was then transferred to Teflon-lined steel autoclaves and heated at 190 °C under static conditions. The autoclaves were removed from the oven after 5 days and quenched in cold water. The product was then recovered by filtration and washed thoroughly with distilled water before being dried at 90 °C for 12 hours.

The same method was used to synthesise a 10% ^{15}N enriched sample by using 0.319 g of standard tPABr and 0.0356 g of ^{15}N tPABr.

5.2.2.2 ^{29}Si{^{1}H} CP MAS

The ^{29}Si{^{1}H} CP MAS spectrum of [tPABr,F]-MFI is shown in Figure 5.12, the majority of the resonances are narrow and at least 10 peaks can easily be resolved, indicating the quality of the sample and how well ordered the structure is, at least on a local scale. The resonance centred at −125 ppm is significantly broader than the rest, and this has been identified as corresponding to the dynamically disordered Si-F site. Koller *et al.* have performed variable temperature NMR studies on this material and have been able to 'freeze-out' the fluoride motion at approximately 140K, giving rise to the characteristic doublet at −148 ppm.[17]
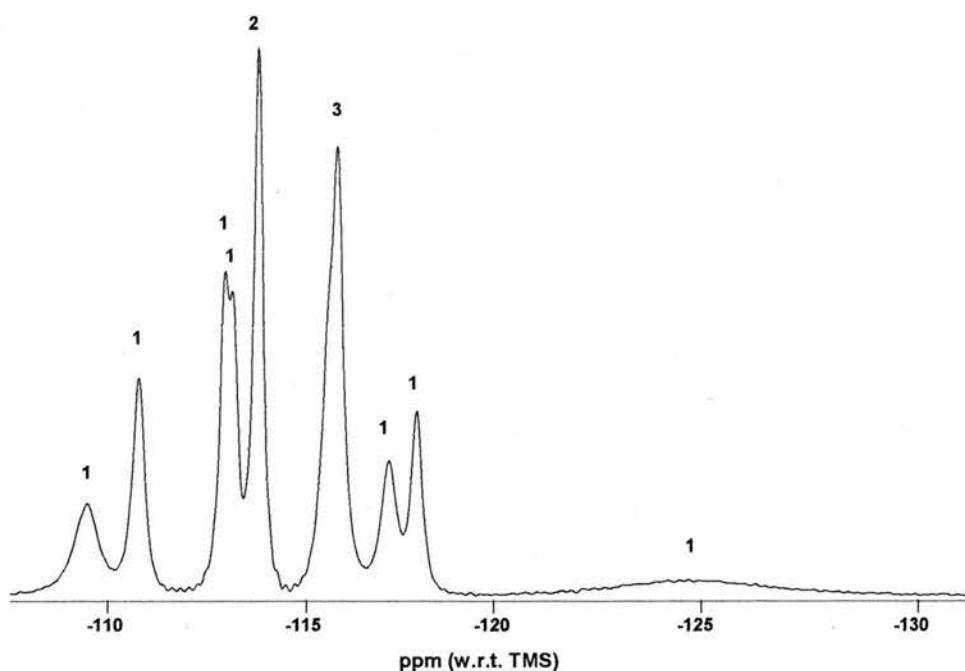
Figure 5.12 ^{29}Si{^{1}H} CP MAS spectrum of 100 % ^{15}N labelled [tPABr,F]-MFI, numbers above the peaks shows the deconvolution result.

Deconvolution of the ^{29}Si{^{1}H} CP MAS NMR spectrum reveals 12 resonances, which correspond to the 12 crystallographically distinct silicon atoms dictated by the Pnma spacegroup. The ^{29}Si{^{1}H} CP spectrum was collected with a 3 kHz spin rate, a 5 ms contact time, 512 acquisitions and a 2 s recycle time.

5.2.2.3 ^{15}N{^{1}H} CP MAS

The ^{15}N{^{1}H} CP spectrum of 100% ^{15}N labelled [tPABr,F]-MFI is shown in Figure 5.13 and consists of one peak with a chemical shift centred at 38.3 ppm. The single resonance corresponds to just one independent N atom, showing that the tPABr template is located at just one site within the zeolite framework.
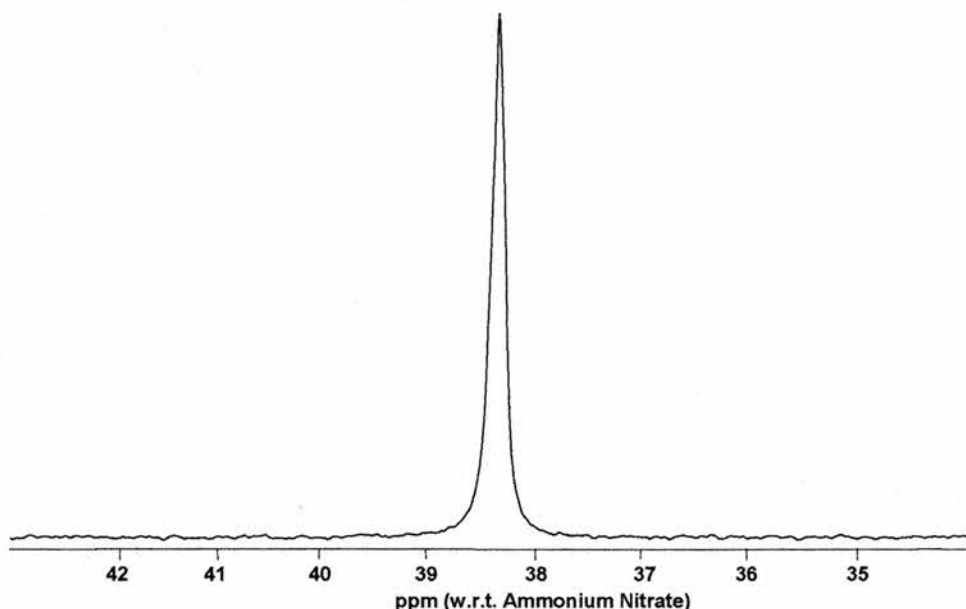
Figure 5.13 ^{15}N{^{1}H} CP MAS spectrum of 100% ^{15}N labelled [tPABr,F]-MFI.

5.2.2.4 MAS NMR Distance Determinations

Initial attempts to perform ^{15}N{^{19}F} CP MAS experiments on the isotopically

labelled sample of [tPABr,F]-MFI have been unsuccessful. These experiments were

designed to enable the ^{15}N-^{19}F internuclear distance to be measured, using the same

methods as applied for [DECDMP,F]-SFF and [DMASD,F]-STF and also by Fyfe *et*

al. for STF and MFI type zeolites.[12,18] There are several possible reasons why these

experiments have been unsuccessful. The first may be as simple as the distance

between the fluoride ions and the nitrogen atoms are too far apart. This would lead to

a very small dipolar coupling, as this is proportional to $1/r^3$, which may not be strong

enough to allow effective cross polarization. The distance between the fluoride ions

and nitrogen atoms has been estimated from previous diffraction studies, and is

thought to be in the region of 7 Å. Similar distances have been measured using MAS

NMR techniques, although these have often been restricted to REDOR experiments.[68,69] The second potential reason why these experiments were unsuccessful may have been due to problems with the high power amplifier, which were only identified a long time after this work was performed. The high power amplifier provides the strong r.f. pulses at the resonance frequency of the ^{19}F nuclei, and it is believed that the amplifier was giving significantly lower power at the time these experiments were performed. The final reason for the lack of cross polarization is thought to be due to the large quantity of ^{1}H atoms that surround the ^{15}N nuclei. The ^{1}H nuclei have a significant effect on the relaxation behaviour, particularly under CP conditions. The effect of the ^{1}H nuclei is to 'drain' away the polarization from the ^{15}N nuclei, so that it relaxes much quicker and, therefore, any signal becomes much weaker and broader. High-power decoupling at the ^{1}H resonance frequency would reduce this broadening and loss of signal. Unfortunately the spectrometer is only equipped with one high-power channel, which can be tuned to either ^{1}H or ^{19}F frequencies, and hence it is not possible to CP from ^{19}F and decouple ^{1}H at the same time. The combination of these factors may explain the lack of cross polarization between the ^{19}F and the ^{15}N nuclei in [tPABr,F]-MFI.

Given the problems with performing CP from ^{19}F to ^{15}N it was decided to attempt a triple resonance CP experiment between ^{1}H-^{15}N-^{29}Si. It was believed that this experiment could be performed as the spectrometer and probe had three channels H, X, Y, where X and Y are low frequency channels. However, although the probe was equipped for triple resonance work, the X and Y channels could not be tuned simultaneously for nuclei with frequencies as low as 50.68 MHz for ^{15}N and 99.35 MHz for ^{29}Si. Independently both the X and Y channels could be tuned for either of

the two frequencies; however, the tuning range of the X channel was significantly reduced (≥ 125 MHz) when the Y channel was set to 50.68 MHz. Although enquiries were made in to lower the tuning range, these could not have been implemented in sufficient time. Although it has not been possible to perform these experiments at the University of St Andrews, they are currently being attempted at the University of British Columbia in Prof. Colin Fyfe's group, using a specially adapted probe capable of tuning to both ^{29}Si and ^{15}N.

5.2.3 Conclusions and Further Work

Two samples of [tPABr,F]-MFI were successfully synthesised using both 10% and 100% ^{15}N enchriched tetrapropylammonium bromide. The quality and lack of disorder in the samples was determined from their ^{29}Si{^{1}H} CP MAS spectra, which showed 10 peaks and could be deconvoluted to give 12 individual silicon sites. Attempts to measure the dipolar coupling between the ^{19}F/^{15}N and ^{15}N/^{29}Si nuclei were unsuccessful and this is believed to be mainly due to technical problems with the high power amplifier and the probe.

Figure 5.14 illustrates some of the internuclear distances in [tPABr,F]-MFI that it is believed can be determined by MAS NMR. If sufficient distances from the F/SDA to the silicon atoms can be measured, then it should be possible to determine the three dimensional structure of [tPABr,F]-MFI using relatively simple trigonometry, as illustrated in Figure 5.15. This will of course become more difficult as the number of independent silicon atoms increases and is reliant on sufficient distances being measured. Any information / distances from such measurements could be used with

powder X-ray diffraction data in order to help discriminate between a correct and

incorrect structure, by incorporation of the distance measurements as constraints.
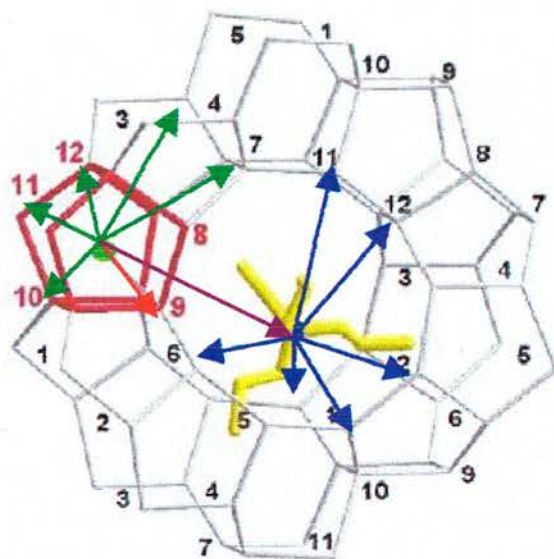
Figure 5.14 A pictorial illustration of the types of distances that can be measured using NMR in

[tPABr,F]-MFI (silicalite-1), where the tetrapropylammonium cation has been enriched with [15]N. Blue

arrows indicate ^{15}N to [29]Si distances that could be measured using [1]H-[15]N-[29]Si TEDOR, green arrows

and red arrow indicate distances between ^{19}F and [29]Si that have been previously measured by Fyfe et al.

indicated by the red cage, purple arrow indicates distance between ^{19}F and ^{15}N that could measured

using CP, REDOR or TEDOR. There are many other internuclear distances that could be determined,

including ^{13}C to [29]Si and ^{19}F, although these are not shown for clarity.
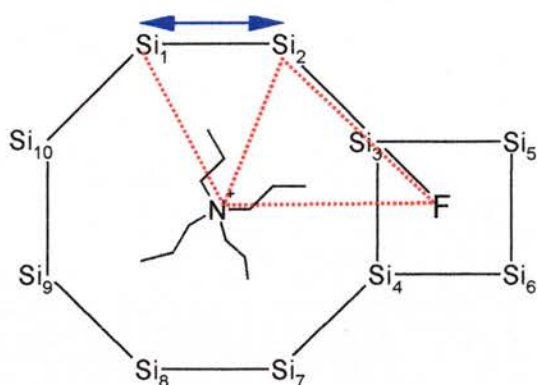
Figure 5.15 Representation of a zeolite structure showing the distances that can be measured (red dotted lines) and the Si – Si distances (blue arrow) that can be calculated using relatively simple trigonometry.

Although this initial work has not yet shown whether it is possible to determine the internuclear distances between the template and the fluoride ions / framework, attempts are still on going.

If these experiments on [tPABr,F]-MFI are successful, not only could this lead to the solving of unknown zeolite structures by NMR but also the methodology could be applied to other systems, where disorder or the inability to produce single crystals, makes the solving of structures by diffraction based techniques very difficult.

5.3 References for Chapter 5

1. E.M. Flanigen and R.L. Patton, *US* US 4 073 865, 1976, 1978.

2. M. A. Camblor, A. Corma, P. Lightfoot, L. A. Villaescusa and P. A. Wright, *Angew. Chem., Int. Ed. Engl.*, 1997, **36**, 2659.

3. A. S. Kuperman, S. Oliver, G. A. Ozin, J. M. Garces and M. M. Olken, *Nature*, 1993, **365**, 239.

4. J. M. Chezeau, L. Delmotte, J. L. Guth and Z. Gabelica, *Zeolites*, 1991, **11**, 598.

5. J. M. Chezeau, L. Delmotte, J. L. Guth and M. Soulard, *Zeolites*, 1989, **9**, 78.

6. I. Bull, L. A. Villaescusa, S. J. Teat, M. A. Camblor, P. A. Wright, P. Lightfoot and R. E. Morris, *J. Am. Chem. Soc.*, 2000, **122**, 7128.

7. M. A. Camblor, L. A. Villaescusa and M. J. Diaz-Cabanas, *Top. Catal.*, 1999, **9**, 59.

8. J. L. Guth, H. Kessler, P. Caullet, J. Hazm, A. Merrouche and J. Patarin, Proceedings From the 9th International Zeolite Conference, R. von Ballmoos, J. B. Higgins and M. M. J. Treacy, Butterworth-Heinemann, Stoneham, MA, 1993, p. p 215.

9. J. L. Guth, H. Kessler, J. M. Higel, J. M. Lamblin, J. Patarin, A. Seive, J. M. Chezeau and R. Wey, *Am. Chem. Soc. Symp. Ser.*, 1989, **389**, 176.

10. J. L. Guth, H. Kessler and R. Wey, New Developments in Zeolite Science and Technology, Proceedings of the 7th International Zeolite Conference, Y. Murakami, A. Ilijima and J. W. Ward, Elsevier, Amsterdam, 1986.

11. P. A. Barrett, M. J. Diaz-Cabanas, M. A. Camblor and R. H. Jones, *J. Chem. Soc., Faraday Trans.*, 1998, **94**, 2475.

12. C. A. Fyfe, D. H. Brouwer, A. R. Lewis, L. A. Villaescusa and R. E. Morris, *J. Am. Chem. Soc.*, 2002, **124**, 7770.

13. B. Harbuzaru, M. Roux, J. L. Paillaud, F. Porcher, C. Marichal, J. M. Chezeau and J. Patarin, *Chem. Lett.*, 2002, 616.

14. L. A. Villaescusa, P. S. Wheatley, I. Bull, P. Lightfoot and R. E. Morris, *J. Am. Chem. Soc.*, 2001, **123**, 8797.

15. L. A. Villaescusa, I. Bull, P. S. Wheatley, P. Lightfoot and R. E. Morris, *J. Mater. Chem.*, 2003, **13**, 1978.

16. H. Koller, A. Wolker, H. Eckert, C. Panz and P. Behrens, *Angew. Chem., Int. Ed. Engl.*, 1997, **36**, 2823.

17. H. Koller, A. Wolker, L. A. Villaescusa, M. J. Diaz-Cabanas, S. Valencia and M. A. Camblor, *J. Am. Chem. Soc.*, 1999, **121**, 3368.

18. C. A. Fyfe, D. H. Brouwer, A. R. Lewis and J. M. Chezeau, *J. Am. Chem. Soc.*, 2001, **123**, 6882.

19. P. S. Wheatley and R. E. Morris, *J. Solid State Chem.*, 2002, **167**, 267.

20. D. S. Wragg and R. E. Morris, *J. Phys. Chem. Solids*, 2001, **62**, 1493.

21. M. A. Camblor, M. J. Diaz-Cabanas, J. Perez-Pariente, S. J. Teat, W. Clegg, I. J. Shannon, P. Lightfoot, P. A. Wright and R. E. Morris, *Angewandte Chemie-International Edition*, 1998, **37**, 2122.

22. G. D. Price, J. J. Pluth, J. V. Smith, T. Araki and J. M. Bennett, *Nature*, 1981, **292**, 818.

23. B. F. Mentzen, M. Sacerdoteperonnet, J. L. Guth and H. Kessler, *Comptes Rendus De L Academie Des Sciences Serie Ii*, 1991, **313**, 177.

24. P. Caullet, J. L. Guth, J. Hazm, J. M. Lamblin and H. Gies, *Eur. J. Solid State Inorg. Chem.*, 1991, **28**, 345.

25. G. Vandegoor, C. C. Freyhardt and P. Behrens, *Zeitschrift Fur Anorganische Und Allgemeine Chemie*, 1995, **621**, 311.

26. M. P. Attfield, C. R. A. Catlow and A. A. Sokol, *Chem. Mater.*, 2001, **13**, 4708.

27. C. A. Fyfe, A. R. Lewis, J. M. Chezeau and H. Grondey, *J. Am. Chem. Soc.*, 1997, **119**, 12210.

28. D. H. Brouwer, The University of British Columbia, 2003.

29. C. A. Fyfe, K. C. Wongmoon, Y. Huang and H. Grondey, *J. Am. Chem. Soc.*, 1995, **117**, 10397.

30. C. A. Fyfe, A. R. Lewis and J. M. Chezeau, *Can. J. Chem.*, 1999, **77**, 1984.

31. S. R. Hartmann and E. L. Hahn, *Phys. Rev. A*, 1962, **128**, 2042.

32. A. Pines, G. Gibby and J. S. Waugh, *J. Chem. Phys.*, 1973, **59**, 569.

33. S. Heidger, Eidgenossiche Technishce Hochshule, 1997.

34. T. Gullion and J. Schaefer, *J. Magn. Reson.*, 1989, **81**, 196.

35. A. W. Hing, S. Vega and J. Schaefer, *Journal of Magnetic Resonance Series a*, 1993, **103**, 151.

36. A. W. Hing, S. Vega and J. Schaefer, *J. Magn. Reson.*, 1992, **96**, 205.

37. P. Bertani, J. Raya, P. Reinheimer, R. Gougeon, L. Delmotte and J. Hirschinger, *Solid State Nucl. Magn. Reson.*, 1999, **13**, 219.

38. E. O. Stejskal, J. Schaefer and J. S. Waugh, *Adv. Magn. Reson.*, 1977, **28**, 105.

39. J. Schaefer, E. O. Stejskal, J. R. Garbow and R. A. McKay, *J. Magn. Reson.*, 1984, **59**, 150.

40. L. Muller, A. Kumar, T. Baumann and R. Ernst, *Phys. Rev. Lett.*, 1974, **32**, 1402.

41. M. H. Levitt, D. Suter and R. Ernst, *J. Chem. Phys.*, 1986, **84**, 4243.

42. P. Bertani, J. Raya and M. Hirschinger, *Solid State Nucl. Magn. Reson.*, 2002, **22**, 188.

43. P. Bertani, K. Raya and K. Hirschinger, *Comptes Rendus Chimie*, 2004, **7**, 363.

44. A. R. George and C. R. A. Catlow, *Zeolites*, 1997, **18**, 67.

45. F. Marica and R. F. Snider, *Solid State Nucl. Magn. Reson.*, 2003, **23**, 28.

46. P. Wagner, S. I. Zones, M. E. Davis and R. C. Medrud, *Angew. Chem., Int. Ed. Engl.*, 1999, **38**, 1269.

47. L. A. Villaescusa, M. Puche and M. A. Camblor, International Symposium on Zeolites and Microporours Crystals, ZMPC 2000, Sendai, Japan, August, 2000, 2000, p. 2-P-015.

48. L. A. Villaescusa, W. Z. Zhou, R. E. Morris and P. A. Barrett, *J. Mater. Chem.*, 2004, **14**, 1982.

49. R. J. Cernik, W. Clegg, C. R. A. Catlow, G. Bushnell-Wye, J. V. Flaherty, G. N. Greaves, I. Burrows, D. J. Taylor, S. J. Teat and M. Hamichi, *J. Synchrotron Rad.*, 1997, **4**, 279.

50. G. M. Sheldrick, *Programs for Crystal Structure Analysis. Release 97-2*, 1997.

51. Siemens, *SHELXTL. Structure Determination Software*, Siemens Analytical X-ray Instruments Inc., Madison, Wisconsin, USA, 1995.

52. L. J. Farrugia, *J. Appl. Crystallogr.*, 1999, **32**, 837.

53. A. L. Spek, *PLATON. A Multipurpose Crystallographic Tool*, Utrecht University, Utrecht, The Netherlands , 1999.

54. H. P. Bai and R. K. Harris, *J. Magn. Reson.*, 1992, **96**, 24.

55. J. C. Cherryman and R. K. Harris, *J. Magn. Reson.*, 1997, **128**, 21.

56. R. K. Harris, K. J. Packer and A. M. Thayer, *J. Magn. Reson.*, 1985, **62**, 284.

57. L. A. Villaescusa, P. A. Barrett and M. A. Camblor, *Chem. Comm.*, 1998, 2663.

58. R. W. Grosse-Kunstleve, L. B. Mccusker and C. Baerlocher, *J. Appl. Crystallogr.*, 1999, **32**, 536.

59. P. A. Barrett, M. A. Camblor, A. Corma, R. H. Jones and L. A. Villaescusa, *J. Phys. Chem. B*, 1998, **102**, 4147.

60. C. A. Fyfe, H. Grondey, Y. Feng and G. T. Kokotailo, *Chem. Phys. Lett.*, 1990, **173**, 211.

61. A. R. Pickford and I. D. Campbell, *Chem. Rev.*, 2004, **104**, 3557.

62. C. M. Santiveri, J. M. Perez-Canadillas, M. K. Vadivelu, M. D. Allen, T. J. Rutherford, N. A. Watkins and M. Bycroft, *J. Biol. Chem.*, 2004, **279**, 34963.

63. D. S. Thiriot, A. A. Nevzorov, L. Zagyanskiy, C. H. Wu and S. J. Opella, *J. Mol. Biol.*, 2004, **341**, 869.

64. A. Bax, R. Freeman, T. A. Frienkel and M. H. Levitt, *J. Magn. Reson.*, 1981, **43**, 478.

65. A. Bax, R. Freeman and S. P. Kempsell, *J. Am. Chem. Soc.*, 1980, **102**, 4849.

66. A. W. Hing, S. Vega and J. Schaefer, *J. Magn. Reson.*, 1992, **96**, 205.

67. E. Aubert, F. Porcher, M. Souhassou, V. Petricek and C. Lecomte, *J. Phys. Chem. B*, 2002, **106**, 1110.

68. M. P. Espe, B. R. Mattes and J. Schaefer, *Macromolecules*, 1997, **30**, 6307.

69. S. M. Holl, G. R. Marshall, D. D. Beusen, K. Kociolek, A. S. Redlinski, M. T. Leplawy, R. A. Mckay, S. Vega and J. Schaefer, *J. Am. Chem. Soc.*, 1992, **114**, 4830.

6.0 Structural Studies of Ferrierite

6.1 Background and Structure

Ferrierite is an aluminosilicate zeolite mineral that was first discovered by R.

Graham near Kamloops Lake, British Columbia, Canada.[1] The name ferrierite comes

from Dr Walter Ferrier, a geologist and mining engineer with the Canadian Geological

Society. The mineral has the idealised formula of $Na_2Mg_2[Al_6Si_{30}O_{72}]$. $18H_2O$ and its

structure was first solved by Staples[2] and then independently confirmed by Vaughan[3]

and by Wise and Tschernich[4,5] in the orthorhombic spacegroup I*mmm*. The natural

mineral also has a rare monoclinic form, which was originally reported by Gramlich-

Meier *et al.*[6] in the spacegroup P2$_1$/*n*, but has since been solved in the spacegroup

I222 by Yokomori *et al.*[7]

The synthetic aluminosilicate form of ferrierite has been widely used in the

petrochemical industry as a shape selective catalyst for the production of isobutene,

which is an important feedstock for the synthesis of methyl t-butyl ether (MTBE).[8,9]

MTBE has been used for many years as an anti-knocking agent in unleaded petrol, but

is now being phased out due to fears of carcinogenic effects.

The structure of ferrierite consists of five corner shared TO_4 tetrahedra, which are

linked together to form five-membered rings (5-MR). These 5-MR are connected to

form chains that run parallel to each other in the a and c axes and which are linked by

bridging oxygen atoms to create 6, 8 and 10-MR channels, as can be seen in Figure

6.1.[10] The 8-MR channels run parallel to the b axis and intersect both the 6-MR

channels and the larger 10-MR channels at 90°. At the intersection of the 6 and 8-MR

channels there is an increase in cross section leading to a more cavity like void, which

is often referred to as the 'ferrierite cage' and is a $[8^2 6^2 6^4 5^8]$ cage.
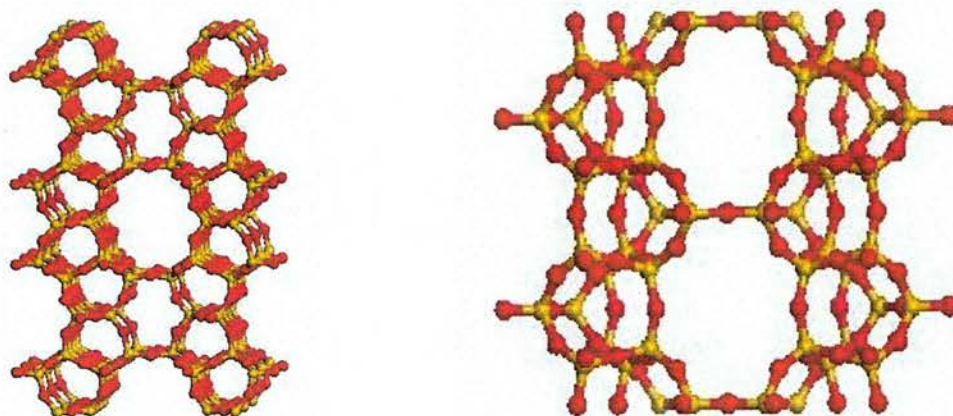

Figure 6.1 Ferrierite structure viewed parallel to the a axis (left) and the b axis (right).

A purely siliceous form of ferrierite can be synthesised and this has been achieved

using both an aqueous[11] and a non-aqueous route.[12] The structure of the calcined

purely siliceous form was first studied by Kuperman *et al.* in 1993 who suggested the

structure was best described in the spacegroup *Immm*.[12] Subsequent crystallographic

studies by Morris *et al.*[10] using combined X-ray and neutron powder diffraction as

well single crystal studies by Lewis and Weigel[13] have shown that the structure is

better described in the spacegroup P*nnm*. A deconvolution of the ^{29}Si spectrum of the

earliest structural study by MAS NMR was, however, only possible by fitting the

resonances with different line-widths.[10] This is unusual for a sample of high

crystallinity and purity and led the authors to conclude, "the real symmetry of the

material may be lower than Pnnm".[10] The *Pnnm* symmetry of ferrierite was, however,

confirmed a few years later by further ^{29}Si and ^{17}O MAS NMR experiments.[14] This

work also reported five resonances in the ^{29}Si spectrum and ten resonances in the ^{17}O

MAS NMR spectra. These corresponded to the five and ten crystallographically distinct Si and O sites described by the P*nnm* spacegroup respectively.

The structure of the as-synthesised form using single crystal X-ray diffraction showed that pyridine molecules were incorporated into the intersections between the 6 and 8-MR channels and the 8 and10-MR channels, as well as partial occupancy by the n-propylamine groups.[13]

Many pure silica zeolites such as ITQ-3, faujasite and MFI have been shown to contract when heated, a property known as negative thermal expansion (NTE).[15-17] The mechanism of this NTE is thought to be due to the transverse vibrations of two connected silicon oxygen atoms. These vibrations of a Si-O-Si bond would reduce the distance between the Si atoms assuming the Si-O bond lengths remained approximately the same. More recently, Bull *et al.* have used microcrystal and powder XRD to show that pure silica ferrierite undergoes a phase transition at about 400 K and that the high temperature form also shows strong NTE.[18]

Phase transitions have been reported for several zeolites including ZSM-5[19-21] and ZSM-11,[22] and both diffraction methods and solid state NMR have been used to study these. High resolution solid state NMR was first used to study phase transitions in minerals by Lippmaa and co-workers in 1980.[23] Since then its use has grown rapidly mainly due to the sensitivity of NMR spectroscopy towards small structural or dynamical changes, which occur near phase transitions. Many phase transitions in minerals have been investigated using NMR including the α -β phase transitions in quartz and cristobalite[24] and the cubic to orthorhombic transition seen in melanophlogite.[25] The ability of MAS NMR to probe local environments makes it

more appealing than X-ray diffraction for studying phase transitions in solids, as XRD can only give a time and space average picture of the structure.[26]

The previous study of the reversible phase transition in siliceous ferrierite revealed that the low temperature form of ferrierite could be best described in the orthorhombic spacegroup P*nnm* but when heated to temperatures above 410 K the structure was better described in the monoclinic spacegroup I*mmm*. During this study Bull *et al.* collected variable temperature ^{29}Si MAS NMR spectra over a relatively narrow range. This work showed that unlike some siliceous zeolites, the chemical shifts of the silicon nuclei were dependent on the temperature and they were able to use geometric correlations to predict the form of the ^{29}Si NMR spectrum outside the temperature range of the experiments. These correlations were first put forward separately by Fyfe *et al.*[27] and Dupree *et al.*[28] in the early 1990s, and connected certain geometrical features of a zeolite structure with the ^{29}Si chemical shifts. For example, in silicalite-1 the chemical shifts of the individual silicon sites correlate extremely well with a simple function of the cosine of the average of the four Si-O-Si bond angles around the particular silicon atom in question. Bull's correlation for ferrierite agreed well with other previous ones on ferrierite and the assignments reached matched those made during a previous INADEQUATE experiment.[10] The prediction made from the correlation was that the high temperature form would consist of four resonances in three groups or envelopes, however, they where unable to verify this experimentally due to temperature limitations of the NMR probe.

It was this lack of high temperature spectra for the purely siliceous ferrierite that provided the initial reasoning for carrying out further MAS NMR studies of this material.

The aims of this work were; firstly, to confirm the predictions made from the diffraction data, by performing further ^{29}Si MAS NMR experiments. Secondly, to investigate the aluminosilicate form of ferrierite for the presence of a displacive phase transition. This, however, firstly required the synthesis of a high quality aluminosilicate ferrierite sample that would give a high resolution [29]Si spectrum and not just a broad featureless peak, which is often characteristic of aluminosilicates.

6.2 Results and Discussions

6.2.1 Synthesis of Pure Silica Ferrierite (Si-FER)

The siliceous ferrierite sample was synthesised hydrothermally in a 23 ml Teflon-lined acid digestion bomb using a modified version of the method by Kuperman *et al.*[12] In a typical synthesis distilled water (6.40 g, 0.356 mol) was mixed with *N*-propylamine (10.5 g, 0.178 moles), pyridine (56 g, 0.708 mol) and HF / Pyridine (70 %) (1.8 g, 0.128 mol). Cab-O-Sil (4 g, 66.58 mmol) was then added over a period of 5 minutes during constant stirring by hand. The resultant solution was transferred to the Teflon liner and had a final gel composition of SiO_2: 10.67 pyridine: 1.33 HF/pyridine: 2.67 *N*-propylamine: 5.33 H_2O. The autoclaves were then heated to 170 °C and left for 5 days to crystallise. After 5 days the autoclaves were removed from the oven and quenched in cold water. The resulting zeolite was recovered by vacuum filtration, washed thoroughly with distilled water and acetone and then dried at 90 °C for 15 hours.

The pyridine and propylamine molecules within the ferrierite channels were then carefully removed by calcining under an atmosphere of oxygen in a tube furnace that

was ramped at 1 °C min^{-1} up to 650 °C and held for 20 hours. The careful calcination conditions ensured that there was no evidence of any occluded carbon and the powder XRD showed no signs of crystal degradation or structural collapse.
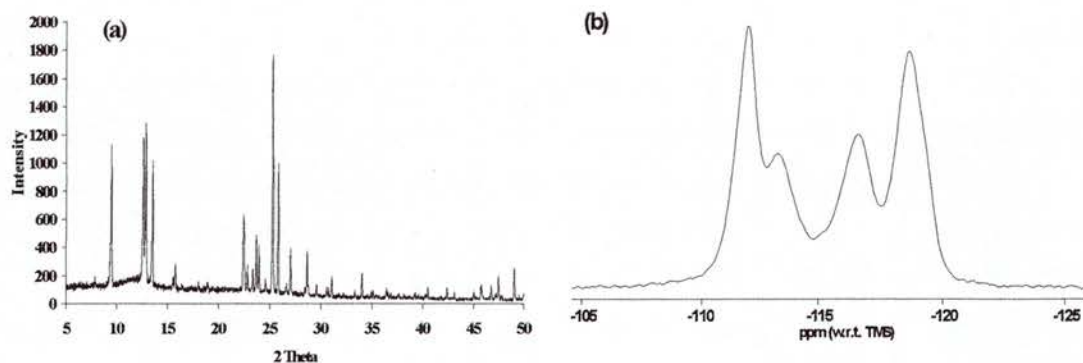

Figure 6.2 (a) XRD powder pattern of calcined siliceous ferrierite, (b) ^{29}Si MAS NMR of as-made siliceous ferrierite.

The product was identified as ferrierite by comparing the powder X-ray diffraction pattern and the ^{29}Si NMR spectrum with those previously published.[29] The purely siliceous ferrierite sample was successfully synthesised using a modification of the non-aqueous method by Kuperman *et al.*[12] The non-aqueous method is known to give large crystals of ferrierite, which after a slight modification of the synthesis ratios also gave high quality ferrierite crystals.
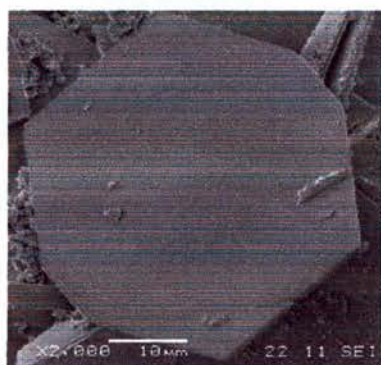

Figure 6.3 SEM image of an octagonal purely siliceous ferrierite crystal.

The careful calcination conditions also meant that there were no signs of any crystal degradation and in particular, no structural collapse, as had previously been reported for purely siliceous ferrierite.[10] This procedure produced very good quality octagonal crystals (Figure 6.3) of calcined purely siliceous ferrierite for further structural investigation by ^{29}Si MAS NMR and microcrystal XRD.

6.2.2 Synthesis of Aluminosilicate Ferrierite (Al-FER)

Initial attempts to synthesise an aluminosilicate form of ferrierite were done using the method by Jacobs *et al.*,[30] which involved the use of sodium hydroxide as a mineralising agent and ethylene diamine as a SDA. In a typical synthesis of composition 1.85 Na_2O: Al_2O_3: 15.2 SiO_2: 592 H_2O: 19.7 C_2DN, sodium hydroxide (0.9 g, 22.5 mmol) was fully dissolved in distilled water (129 ml, 7.16 mol). Sodium aluminate (3.3 g, 53% Al_2O_3) was then added to the solution and the mixture stirred until all the solids had dissolved. Silica sol (46.47 g, Ludox AS-30) was then added to ethylene diamine (18.3 g, 0.304 mol) and this mixture was added to the aluminate solution and thoroughly stirred. The resulting clear solution was then loaded in to Teflon-lined stainless steel autoclaves and heated at 170 °C. After 15 days the autoclaves were removed from the oven and quenched in cold water to give a white crystalline product that was recovered by vacuum filtration. The product was then washed with distilled water followed by acetone and then dried at 100 °C for 16 hours. The zeolite sample was then calcined to remove any occluded organics using the same method as for the pure silica polymorph.

The Na, Al-ferrierite samples had low resolution in their ^{29}Si NMR spectra and very little structural information could be obtained, instead all that could be seen was one broad peak that showed little change with varying temperature.
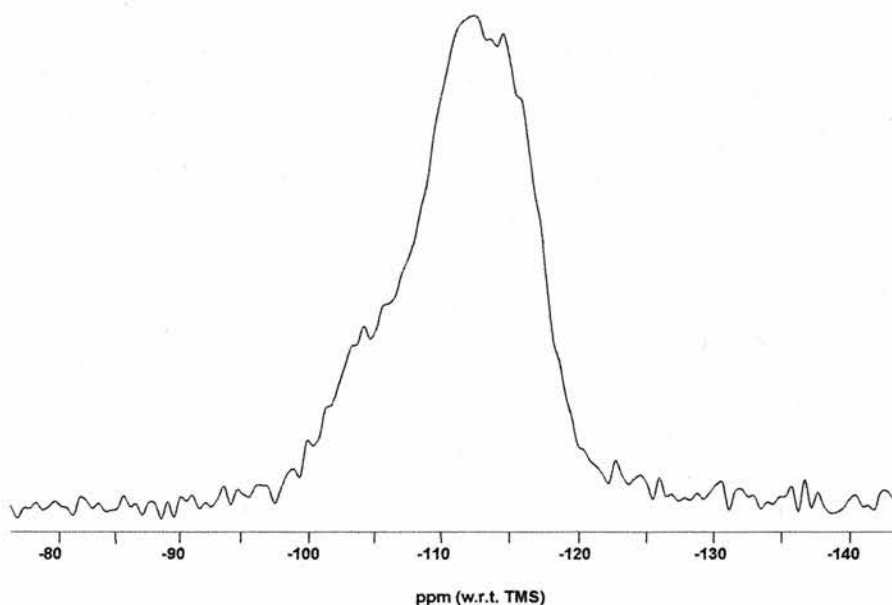

Figure 6.4 ^{29}Si MAS NMR spectrum of Na,Al-FER

To try to improve the peak resolution in the ^{29}Si NMR spectra a new synthesis method based on that for the pure silica polymorph was devised. This method involved replacing some of the Cab-O-Sil with aluminium hydroxide. Three samples were synthesised with varying aluminium contents as listed in Table 6.1.

Aluminosilicate ferrierite sample	Synthesis gel ratios	Si / Al
Low aluminium ferrierite (LAl-FER)	1 SiO_2: 0.068 $Al(OH)_3$: 10.67 Pyr: 1.33 HF/Pyr: 2.67 $PrNH_2$: 5.33 H_2O	25.5
Aluminium ferrierite (Al-FER)	1 SiO_2: 0.144 $Al(OH)_3$: 10.67 Pyr: 1.33 HF/Pyr: 2.67 $PrNH_2$: 5.33 H_2O	12
High aluminium ferrierite (HAlFER)	1 SiO_2: 0.325 $Al(OH)_3$: 10.67 Pyr: 1.33 HF/Pyr: 2.67 $PrNH_2$: 5.33 H_2O	5.4

Table 6.1 Aluminosilicate ferrierite (F,Al-FER) syntheses

In a typical synthesis, distilled water (3.20 g, 0.178 mol) was mixed with aluminium hydroxide (0.13 g, 1.67 mmol), *N*-propylamine (5.25 g, 89 mmol), pyridine (28 g, 0.354 mol) and HF / Pyridine (70 %) (0.9 g, 64 mmol). Cab-O-Sil (0.9 g, 14.9 mmol) was then added over a period of 5 minutes during constant stirring by hand. The resultant solution was transferred to Teflon-lined stainless steel autoclaves, which were then heated to 170 °C and left for 5 days for the product to crystallise. After 5 days the autoclaves were removed from the oven and quenched in cold water. The resulting zeolite was recovered by vacuum filtration, washed thoroughly with distilled water and acetone and then dried at 90 °C for 15 hours.
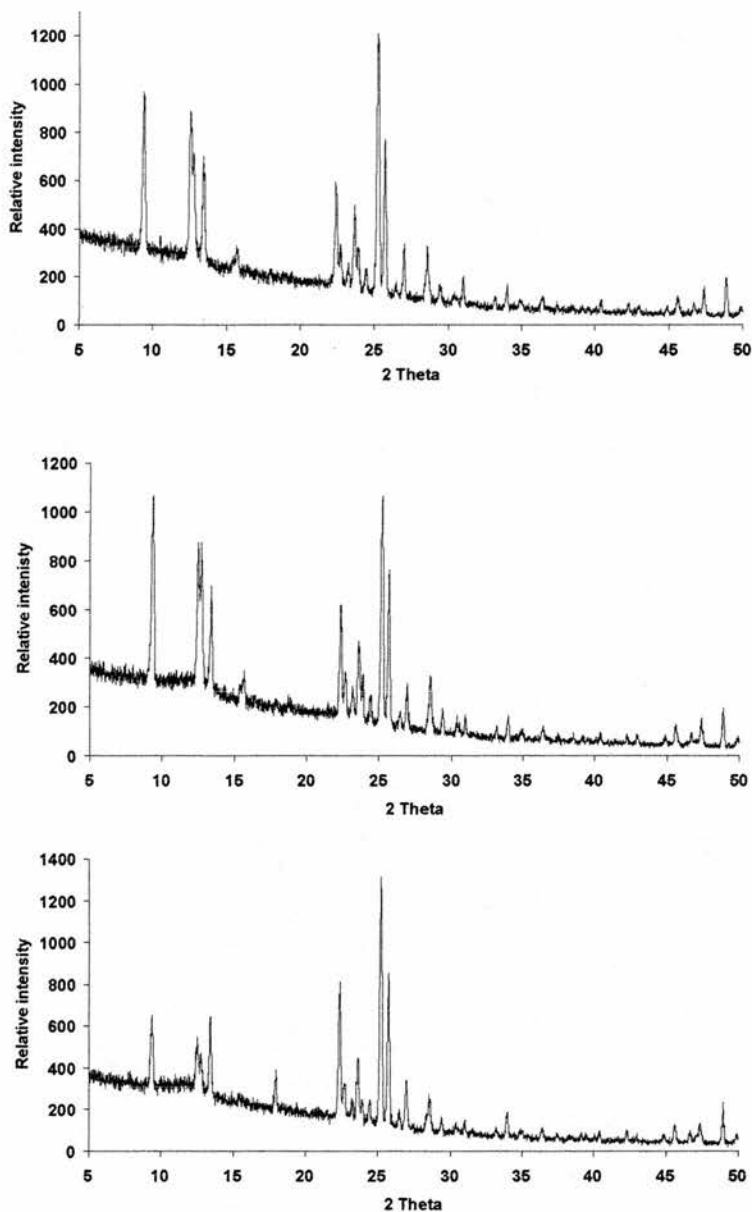
Figure 6.5 Powder XRD patterns for HAlFER (top), MAlFER (middle) and LAlFER (bottom).

Three samples of the aluminosilicate zeolite ferrierite (F,Al-FER) were successfully synthesised with varying quantities of aluminium. All three of the samples showed much higher resolution in their ^{29}Si MAS NMR spectra than the initial sodium containing aluminosilicate ferrierite. The increase in spectral resolution is thought to be related to the quality of the zeolite framework, with the Na,Al-FER

sample containing several Si-OH defects.[31] The number of these defects would be expected to be larger for a zeolite sample synthesised in hydroxide media than a sample produced by the fluoride route. This prediction seems to hold true, as all three of the samples produced by the fluoride route appear to have less structural defects. The presence of less defects in the F,Al-FER is not just apparent in the ^{29}Si spectra, examination of the crystals under an optical microscope revealed high quality hexagonal plate-like crystals, unlike the Na,Al-FER crystals, which were poorly formed and intergrown.

6.2.3 Variable Temperature MAS NMR Study of Purely Siliceous Ferrierite

As mentioned in the introduction to this chapter, X-ray diffraction data from a previous study on purely siliceous ferrierite showed that the low temperature phase was best indexed as orthorhombic with symmetry *Pnnm*.[18] This spacegroup requires that there are five crystallographically distinct silicon atoms, which was confirmed by their ^{29}Si MAS NMR experiments. The phase transition and the high temperature phase of siliceous ferrierite was not investigated during this previous study due to instrumental temperature restrictions.

^{29}Si MAS NMR spectra were collected between 133 K and 473 K (Figure 6.6). The lowest temperature (133 K) ^{29}Si spectrum collected on a very high quality sample of calcined siliceous ferrierite clearly shows that there are more than the 5 expected resonances needed for the P*nnm* spacegroup.
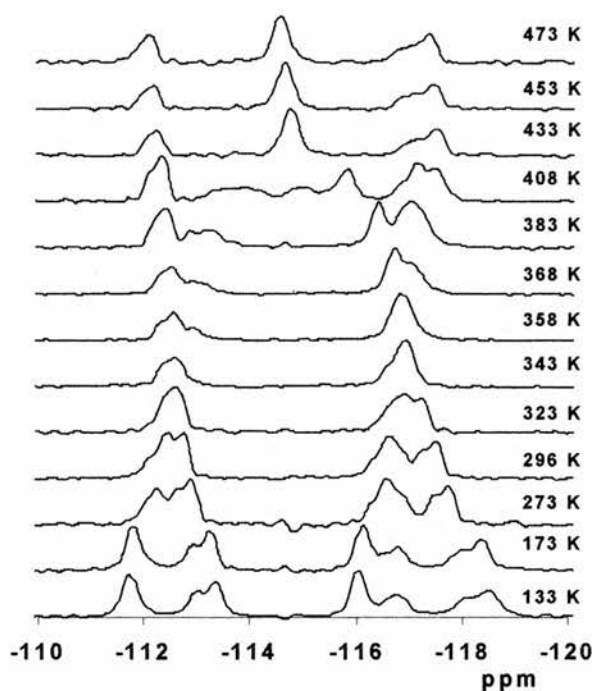
Figure 6.6 Variable temperature ^{29}Si MAS NMR spectra of siliceous ferrierite

The spectrum clearly shows a minimum of seven resonances and deconvolution (Figure 6.7) reveals at least nine or ten resonances, implying that the actual symmetry of this material is lower than *Pnnm*. The symmetry is, however, consistent with other orthorhombic or monoclinic subgroups of *Pnnm* such as $P2_12_12$, *Pnn2*, *P2/m*, *Pnm2$_1$*.
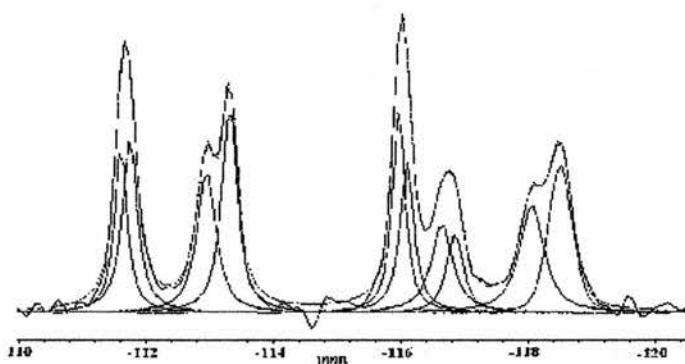

Figure 6.7 Deconvolution of the 133 K ^{29}Si MAS NMR spectrum of siliceous ferrierite, showing more than the five resonances expected for *Pnnm* symmetry.

However, this deconvolution does require the resonances to be of slightly different widths and, therefore, it is not possible from the NMR data alone to unambiguously determine the low temperature spacegroup.

As the temperature increases, the well-resolved peaks coalesce in to two groups at around 320 K. This coalescence of the resonances is not as it first may appear a phase transition; instead, it is simply due to the overlap of the peaks as the chemical shifts of the various nuclei change with temperature. This can be shown as there are still more than five resonances visible above 360 K and no evidence of a phase transition in this region was observed by XRD or differential scanning calorimetry experiments performed in the previous study.[18] As the temperature is increased above 360 K the resonances separate out again, however, this time the two original outer most resonances move towards the centre of the spectrum at −115 ppm having overlapped and crossed their neighbouring peaks. This can be seen more easily by comparing the original chemical shift predictions made by Bull *et al.* from the microcrystal X-ray diffraction data with this new variable temperature ^{29}Si MAS NMR data, as shown in Figure 6.8.
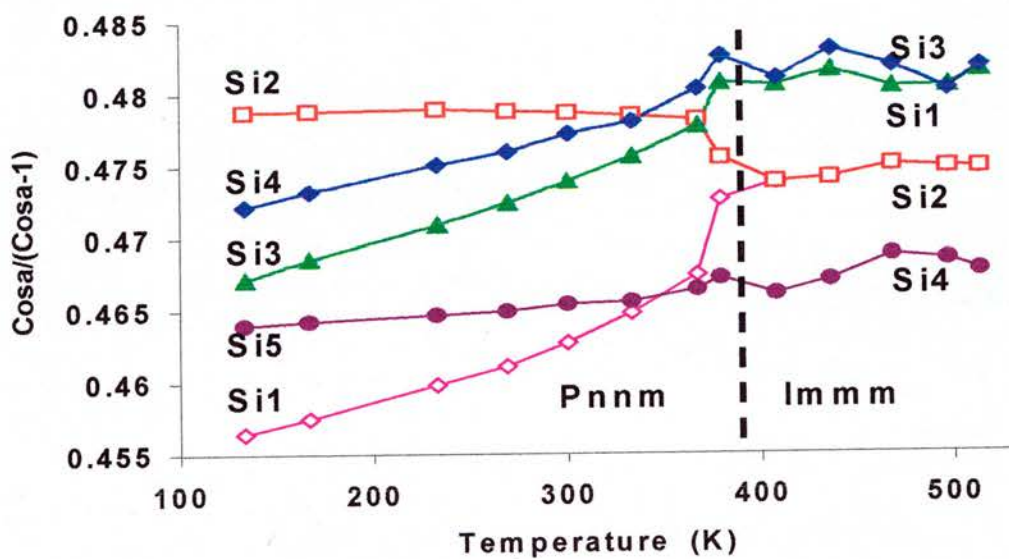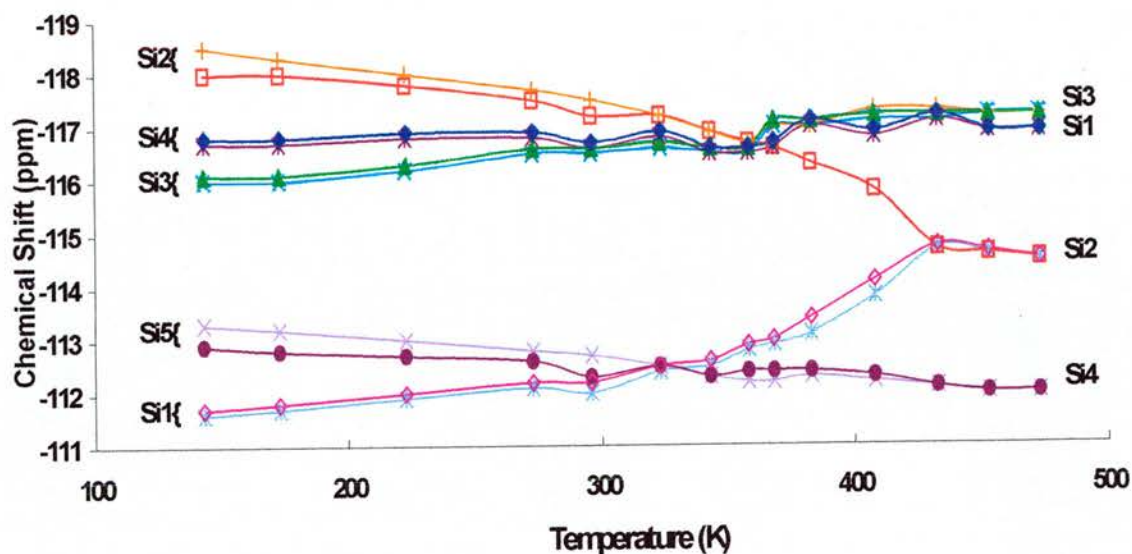
Figure 6.8 Comparison of the ^{29}Si chemical shifts (top, a ten-line deconvolution was used for the low temperature phase, four lines for the high temperature phase) with the average cos(a)/[cosa -1] for each of the silicon atoms obtained from microcrystal X-ray diffraction (five in low T phase, four for the high T phase).

The top graph in Figure 6.8 shows a plot of the chemical shifts against temperature for the ^{29}Si resonances seen in the ferrierite spectra. A ten-line deconvolution was used for the low temperature phase and four lines used for the high temperature phase. The lower graph shows a plot of cos(a)/[cos(a)-1] against temperature, where a is the Si-O-Si bond angle around each of the silicon sites, as measured from the previous diffraction data. A comparison of these two graphs shows that they have generally the same form over essentially the whole temperature range. The crossover of the peaks corresponding to Si1 and Si2 (according to the atom numbering scheme reported in the previous X-ray diffraction work) in the NMR plot can now easily be seen to occur at around 370 K. Above this temperature, at around 420 K, the structure undergoes a phase transition and adopts the high temperature form with four resonances clearly visible, exactly as predicted from the X-ray diffraction data for the spacegroup I*mmm*. These four resonances correspond to the four crystallographically inequivalent silicon atoms required for the I*mmm* spacegroup and can be seen to shift slightly towards the low field end of the spectrum with increasing temperature. However, only three spectra, clearly above the phase transition, were collected and further experiments would need to be performed to higher temperatures to accurately confirm this temperature dependence of the chemical shifts.

Comparison of the two graphs below 400 K, where ferrierite has its low temperature form, shows that the NMR and XRD results differ somewhat. As already mentioned, the low temperature spectra can easily be resolved in to at least seven resonances, and probably as many as ten. This is of course quite different from previous X-ray diffraction studies, which had all indicated that the symmetry of the material was *Pnnm*, which would give only five resonances in the ^{29}Si spectrum. The

lowest temperature ^{29}Si spectrum collected, clearly shows the greatest deviation from the *Pnnm* symmetry. The equivalent temperature data from the diffraction experiments was carefully re-examined along with new data (see Chapter 6.1.2) for evidence indicating lower symmetry. However, the systematic absences and merging of the equivalent data were completely consistent with the orthorhombic symmetry of *Pnnm*. Furthermore, the refinement of the structural model without symmetry (spacegroup P1) followed by the use of the computer program PLATON[32] to indicate the missing symmetry always yielded the spacegroup as *Pnnm*. This means that according to the accepted conventions of X-ray crystallography this structure is correctly described in symmetry *Pnnm*. The distortion from *Pnnm* symmetry observed by ^{29}Si MAS NMR must be too small to quantify from the X-ray diffraction experiments. This highlights the sensitivity of NMR towards the local structure of a material and must be an example of where X-ray diffraction, under normal experimental conditions, is not as sensitive as NMR to small deviations from a higher pseudosymmetry.

The MAS NMR results can, however, be grouped in to five resolved 'envelopes' and with each of these envelopes being resolved in to two peaks. As the temperature is increased, the behaviour of the $\cos(\alpha)/[\cos(\alpha)-1]$[27,28] curves resemble that of the chemical shift curves. In both graphs it can be seen that the silicon resonances are split in to two groups that eventually coalesce, although the X-ray diffraction does predict that the low field resonances should coalesce at a lower temperature than is actually the case.

Where the $\cos(\alpha)/[\cos(\alpha)-1]$ function can be seen not to hold well is in the prediction of the absolute changes in the chemical shifts. This is clearly shown with

the example of Si2, for which the X-ray diffraction derived function predicted would be invariant with temperature between 100 and 350 K while in fact the chemical shift changes markedly within this range. The function used in Figure 6.8 is a relatively crude and empirical one and hence it is not too surprising that it does not exactly predict the NMR chemical shift behaviour.

Around the phase transition from the low temperature form to the high temperature form the MAS NMR spectra become more complex (Figure 6.9). The X-ray diffraction data predicts that the chemical shifts for the four resonances due to the two pairs of silicon atoms, described in the P*nnm* diffraction study as Si1 and Si2, should change very rapidly with temperature. Figure 6.9 shows thirteen spectra collected over a narrow temperature range around the phase transition and it is clear that this rapid change for Si1 and Si2 does occur. The resonances in these spectra can also be seen to be considerably broader than those present well below or above the phase transition. This is consistent with dynamic averaging processes that may be occurring in the system. However, the chemical shifts in this region are so sensitive to temperature that any inhomogeneity due to slight temperature gradients or unequal heating of the structure could also lead to broadening of the peaks. Calibration of the temperature using the ^{207}Pb spectra of lead nitrate did indicate the presence of small temperature gradients; however, these were probably insufficient to account for all the broadening seen in the ferrierite spectra.[33]
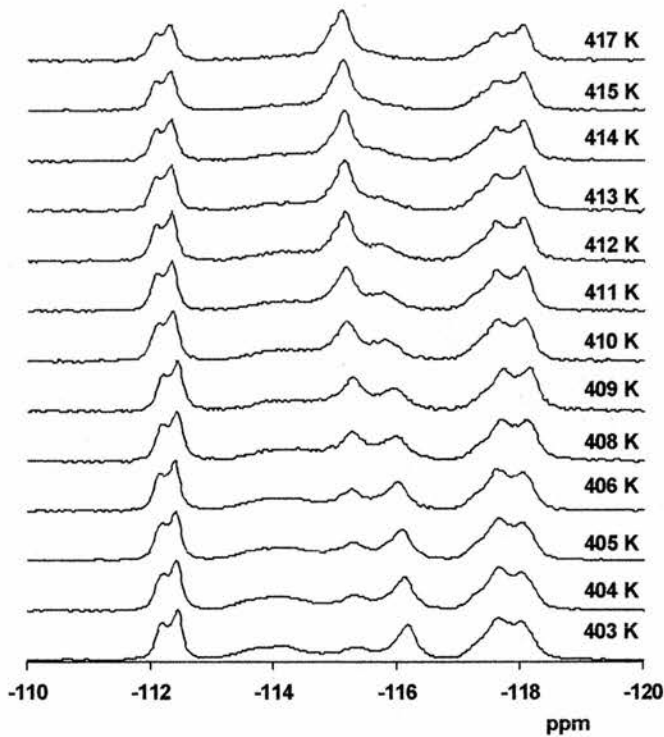
Figure 6.9 Variable temperature ^{29}Si NMR spectra around the phase transition.

There are several different types of phase transition found in minerals and these include displacive phase transitions, cation ordering transitions and orientational order-disorder phase transitions.[34] The type of phase transition observed for ferrierite is believed to be a displacive phase transition, which involves only small translations and rotations of the SiO_4 tetrahedra.[35] Phase transitions can be described as being either first or second order; a first order transition is characterised by a discontinuous change in the structure, whereas in a second order transition the structure of the low temperature phase merges continuously with that of the high temperature phase at the phase transition. In the case of ferrierite the ^{29}Si MAS NMR spectra and previous DSC results show that the structure undergoes a second order transition, with a continuous change in the structure from the low temperature to the high temperature form.

The theory of phase transitions can be illustrated well by using a simple model as illustrated in Figure 6.10.[34,36]
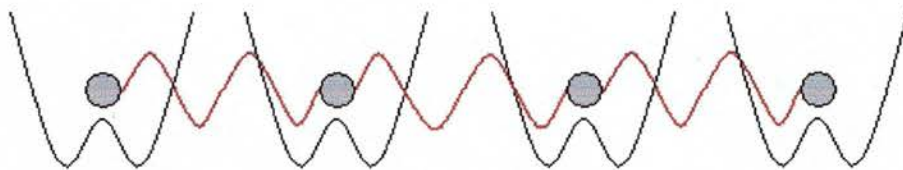

Figure 6.10 Representation of a simple model that undergoes a phase transition. The atoms vibrate in double well potentials and interact with their neighbours by harmonic forces, represented by red springs. Redrawn from ref. 34.

The model shown in Figure 6.10 consists of an array of atoms, which are linked by harmonic forces. Each of these atoms "sees" a local double well potential, which is assumed to represent the rest of the crystal that is not included in the model. The driving force for the phase transition is these double well potentials. At low temperatures the equilibrium structure consists of all the atoms displaced to one side or the other of their origin. A phase transition occurs on heating the structure to higher temperatures with each of the atoms now vibrating about its origin. In particular for a displacive phase transition at high temperatures, the effects of the double well potential are quite insignificant with the atoms just vibrating about the zero position with large amounts of vibrational energy (Figure 6.11).
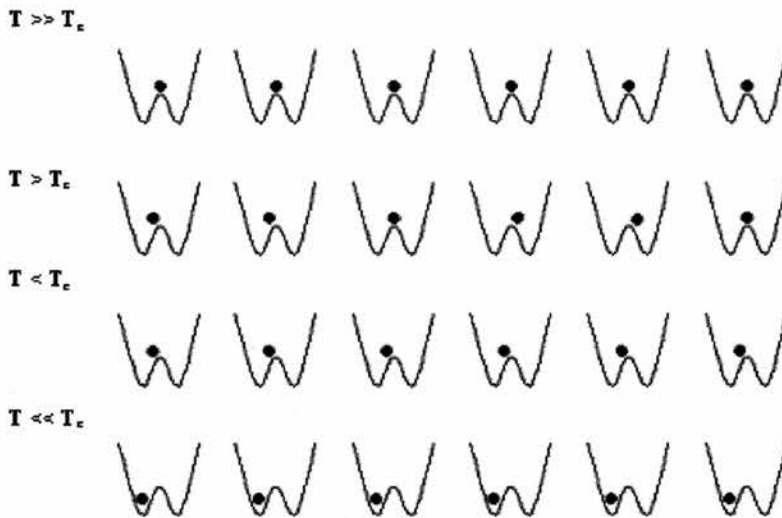
$T \gg T_c$

$T > T_c$

$T < T_c$

$T \ll T_c$

Figure 6.11 Sequence showing ordering of atoms during a displacive phase transition. At high temperatures $(T \gg T_c)$ the atoms vibrate about the zero position, and the effects of the double well potential are not significant. On cooling towards the transition temperature $(T > T_c)$ a degree of short-range order is established, where neighbouring groups of atoms are temporarily displaced from the zero position, as the effects of the double well potential become more significant. Below the transition temperature $(T < T_c)$ the atoms vibrate about positions that are shifted away from the zero position, and all the atoms vibrate about the same displaced point. At very low temperatures $(T \ll T_c)$ all the atoms occupy the same side of the double well potential. Redrawn from ref. 34.

As the temperature is reduced towards the phase transition the atoms have less vibrational energy and start to spend relatively more time on either side of the origin as the effects of the double well potential become greater. The effects of the double well potential are still less than the strength of the vibrational forces between neighbouring atoms and, therefore, neighbouring atoms are displaced by similar amounts from the origin. At temperatures below the phase transition the average positions of all the atoms are displaced by the same amount to just one side of the origin and the size of this displacement increases with further cooling.[34]

Dove *et al.* have attempted to take the theory of displacive phase transitions further by focussing on the rigidity of the SiO_4 and AlO_4 tetrahedra in silicates and aluminosilicates.[37] This new theory is called the rigid-unit mode (RUM) model; RUMs are normal modes of vibration that can propagate without any distortion of the SiO_4 tetrahedra, at least within the small amplitude limit.[37]

There are two main factors that influence the driving force for a displacive phase transition in silicates, the first is the coupling between neighbouring atoms that allows long-range ordering and leads to a local deformation propagating over large distances. The second is a longer-range force that drives the actual deformation and this is described by the double well potential. The double well potential has three contributions; the first being the effect of long-range interactions. Dove suggests that these are due to the dispersive interactions between highly polarizable O atoms, and that the long-range interactions are attractive and pull the structure in to the highest density possible.[38] The second contribution is the short-range attraction between an occluded cation and neighbouring O anions, this interaction can lead to the collapse of a framework about a cation, which will propagate over long distances. The final contribution is the most important for understanding the phase transition in ferrierite and arises from the energy associated with T-O-T bond angles. An ideal T-O-T unit (where T can be either Si and / or Al) will have a bond angle of approximately 145° and a unit that has a bond angle differing from this value will have a higher energy.[37] In materials like cristobalite[39] and ferrierite,[18] the high temperature phase appears to have a bond angle of 180°. In the actual structures, this leads to a degree of disorder due to neighbouring tetrahedra rotating to accommodate this bond angle via a

mechanism described by the RUM resulting in a displacive phase transition, as shown for ferrierite in Figure 6.12.
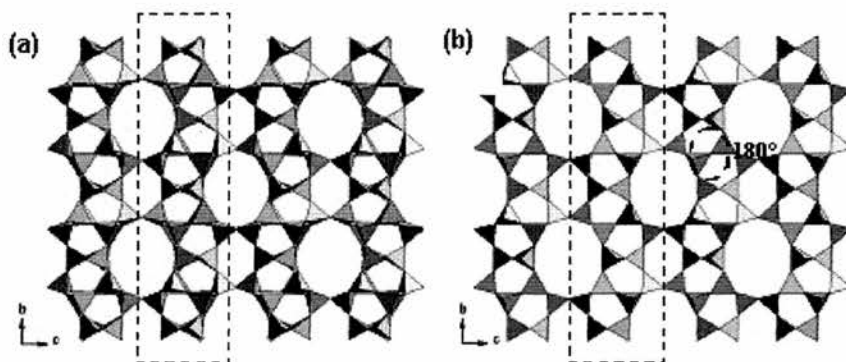

Figure 6.12 (a) The low temperature phase of ferrierite with symmetry Pnnm. (b) High temperature phase of ferrierite with symmetry I*mmm* and, therefore, a Si-O-Si bond angle of 180°. Dashed boxes highlight rotation of tetrahedra between P*nnm* and I*mmm* symmetry.

The high temperature phases of ferrierite and cristobalite are both constrained to have a 180° Si-O-Si bond angle by their spacegroups, Immm and $Fd\bar{3}m$ respectively.[18,40] In reality, however, a 180° bond angle is not chemically sensible although these have been "measured" during previous X-ray diffraction studies. Spearing *et al.* have concluded from detailed ^{29}Si and ^{17}O NMR studies on the α - β cristobalite transition that the high temperature β phase exists as a dynamical average of twin related configurations.[24] A similar model can be proposed for ferrierite and it seems likely that the high temperature phase in this material is also due to a dynamical average of related configurations. Spearing *et al.* reported that for the α -β phase transitions in quartz and cristobalite the lines in the ^{29}Si NMR spectra moved together and broadened as the temperature approached the phase transition. This broadening was seen to collapse to a single narrow line for both quartz and cristobalite above the phase transition temperature, and was in excellent agreement

with predictions made by Anderson on the effects of dynamic averaging.[41] This could

explain the broadening of the resonances seen in Figure 6.9 for ferrierite as the phase

transition temperature is approached. Swainson *et al.* have concluded that cristobalite

is a dynamically disordered system, in which the $Fd\bar{3}m$ symmetry is preserved and the

disorder originates from the action of a linear combination of RUMs of many different

symmetries.[42,43] This could well be the same for ferrierite with the mechanism for the

flipping between the related configurations being described by the oxygen atoms in

certain Si-O-Si linkages being dynamically disordered in an annulus around the Si-Si

axis. This explains the 180° Si-O-Si bond angle, constrained by symmetry in the

Immm phase and "measured" by X-ray diffraction as the average of such annular
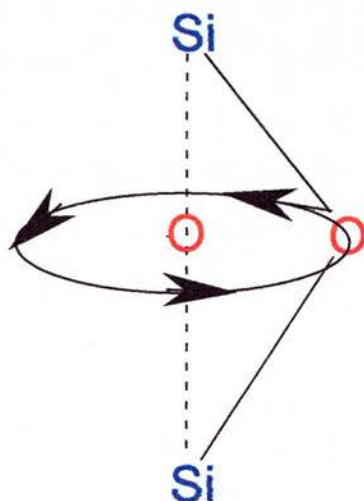
disorder (Figure 6.13).[41]

Figure 6.13 Annular disorder as seen in certain Si-O-Si bonds in ferrierite.

If the frequency of the flipping between the different configurations (i.e. the

frequency of rotation about the annulus) is similar or less than the frequency

separation of the resonances there will be a broadening and shifting of the peaks

toward one another. As the frequency of the flipping increases, so that it is significantly larger than the separation of the peaks they will be averaged in to the sharp, coalesced signal as is seen in the high temperature phase of ferrierite.[24] In their work, Spearing *et al.* identified two different possibilities for the dynamics model of cristobalite, one where there was significant flipping between structures below the transition temperature, and one where this only occurs above the transition. Molecular dynamics simulations by Swainson *et al.* showed that some of the Si-O-Si bonds in cristobalite were dynamically disordered in the form of an annulus.[42] However, they suggested that the annulus should not be thought of as a fixed radius annulus, but rather as a very broad probability distribution. They also concluded that the dynamic disorder mainly affected the O atoms and was much larger in the high temperature β phase than the low temperature α phase but that no evidence of distinct domains could be found. The prediction that some dynamic disorder is present in the low temperature phase is consistent with the first prediction of Spearing *et al.* and the same may be true for ferrierite. However, there is much less evidence from other techniques such as ^{17}O NMR, molecular dynamics studies or inelastic neutron spectroscopy about the phase transition or the high temperature structure of ferrierite.

These variable temperature studies have given a much greater insight in to the thermal behaviour of purely siliceous ferrierite. In particular, the high resolution low temperature spectra has indicated that the real symmetry of ferrierite is actually lower than that determined by previous X-ray diffraction studies.[2,3,10,13,14,18] However, new low temperature microcrystal X-ray diffraction data for siliceous ferrierite was collected during this study and the results are presented in Chapter 6.2.4. A comprehensive ^{29}Si MAS NMR study around the phase transition has shown that the

high temperature phase of ferrierite is likely to be a dynamic average. This dynamic averaging is thought to be due to Si-O-Si bond disorder in the form of an annulus around the Si-Si axis, as has been suggested for cristobalite.[24,42] However, it should be noted that a great deal more information from both experimental and theoretical methods is available for cristobalite than for ferrierite. Until a similar quantity of information exists for ferrierite and other siliceous zeolites, the exact details of the phase transition in ferrierite cannot be confirmed.

As ferrierite is used widely in industry as a catalyst,[8,9,44] often at elevated temperatures, it is important to fully understand the phase transition and the high temperature structure. A complete knowledge of the thermal behaviour of ferrierite may provide a further understanding of its role as a catalyst and enable new applications to be found.

6.2.4 Microcrystal XRD Study of Calcined Purely Siliceous Ferrierite

The crystals of the calcined purely siliceous ferrierite were too small (~ 60 x 60 x 5 μm) for analysis on a standard laboratory diffractometer and were, therefore, analysed using synchrotron radiation at Station 9.8 of the Daresbury SRS.[45]

The structure of calcined siliceous ferrierite was solved by direct methods (SHELXS-97)[46] and refined with a full-matrix least-squares technique (SHELXL-97)[47] using the WinGX suite of programs.[48] Low temperature ^{29}Si MAS NMR data showed that the structure was probably of lower symmetry than previously thought, and this led the structure to be refined with both Pnnm and Pnn2 symmetry. Refinements at 150 K in both symmetries gave R-factors of approximately 2.8 %, however, analysis of the Pnn2 refinement for missing symmetry using the PLATON[32]

software revealed that the spacegroup should be P*nnm*. The calcined structure of ferrierite was, therefore, refined fully in the orthorhombic spacegroup P*nnm*, with unit cell parameters of a= 7.4068(3) Å, b= 14.0713(7) Å, c= 18.6699(9) Å. Full details of the data collection and the refinement parameters can be seen in Table 6.2, and the details of the structure determination can be found on the attached CD as Crystallographic Information Files.

Identification code	Ferrierite	
Empirical formula	$Si_{32}O_{72}$	
Formula weight	2050.88	
Temperature	150(2) K	
Wavelength	0.69500 Å	
Crystal system	Orthorhombic	
Space group	*Pnnm*	
Unit cell dimensions	a = 7.4068(3) Å	alpha = 90°
	b = 14.0713(7) Å	beta = 90°
	c = 18.6699(9) Å	gamma = 90°
Volume	1945.84(16) Å^3	
Z, Calculated density	1, 1.750 Mg/m^3	
Absorption coefficient	0.519 mm^{-1}	
F(000)	1024	
Crystal size	0.06 x 0.06 x 0.005 mm	
Θ range for data collection	1.77 to 29.75 deg.	
Limiting indices	-10<=h<=10, -20<=k<=19, -26<=l<=26	
Reflections collected / unique	20439 / 3026 [R(int) = 0.0409]	
Completeness to theta = 29.75	98.9 %	
Absorption correction	None	
Refinement method	Full-matrix least-squares on F^2	
Data / restraints / parameters	3026 / 0 / 126	
Goodness-of-fit on F^2	1.062	
Final R indices [I>2sigma(I)]	R1 = 0.0276, wR2 = 0.0731	
R indices (all data)	R1 = 0.0385, wR2 = 0.0773	
Extinction coefficient	0.0023(9)	
Largest diff. peak and hole	0.341 and −0.350 e.A^{-3}	

Table 6.2 Crystal data and structure refinement for calcined pure silica ferrierite.

The structure of purely siliceous ferrierite can be seen in Figure 6.14, with views down both the a axis (left) and the b axis (right).
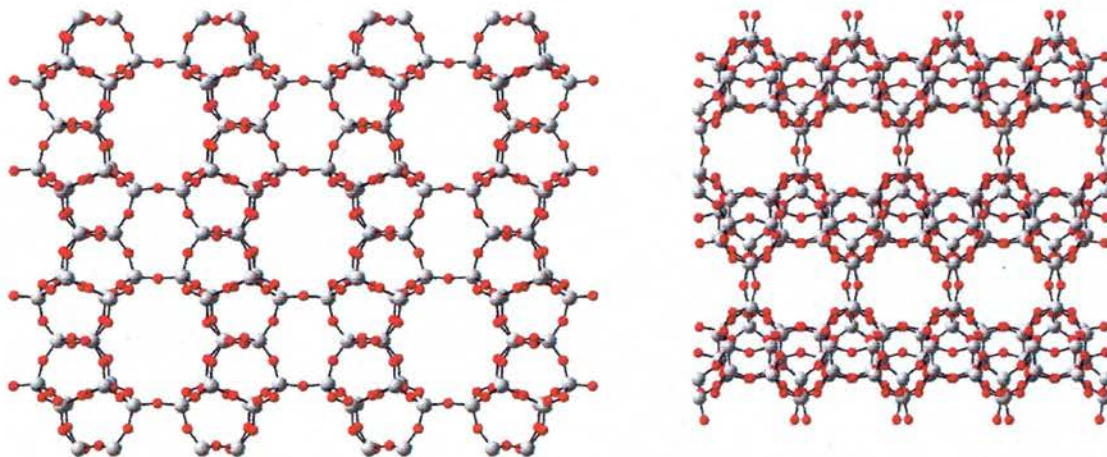

Figure 6.14 Structure of purely siliceous ferrierite as viewed down the a axis (left) and the b axis (right).

The results of this microcrystal X-ray diffraction experiment are in excellent agreement with the previous studies by Morris *et al.*[10] and Bull *et al.*,[18] all of which show that the low temperature structure of ferrierite is orthorhombic with P*nnm* symmetry. This symmetry implies five crystallographically distinct Si sites corresponding to five resonances in the ^{29}Si NMR spectrum. There are clearly more than five resonances in the low temperature ^{29}Si NMR spectrum, indicating a lower symmetry of perhaps P*nn*2. Although refinement of the data in the P*nn*2 spacegroup gave a slightly better fit according to the R-factor, analysis for missing symmetry showed that the structure was better described with P*nnm* symmetry. MAS NMR has long been known as a more sensitive technique for analysing the local structure of a material than a conventional X-ray diffraction experiment.[49] The P*nn*2 spacegroup is noncentrosymmetric and this enabled non-linear optical measurements to be made on

the calcined purely siliceous ferrierite sample in order to reinforce the MAS NMR result. The shining of the infrared laser light through the powdered sample yielded a weak green light (second harmonic generation), which was more than that produced from the blank sample due to structural defects and surface effects. This result may well indicate that the symmetry of the low temperature phase of ferrierite should be Pnn2 and not the currently accepted Pnnm. This could be confirmed by performing ^{17}O MAS NMR experiments on this sample of pure silica ferrierite to determine the number of distinct oxygen sites. If Pnn2 is the correct spacegroup, then 19 resonances would be observed in the ^{17}O NMR spectrum and not the ten resonances previously reported.[14]

6.2.5 Variable Temperature MAS NMR Study of Aluminosilicate Ferrierite

Nearly all the X-ray diffraction studies of the natural mineral ferrierite have described the structure as orthorhombic with Immm symmetry.[2-5] However, the synthetic purely siliceous polymorph of this mineral has been solved in both the Pnnm and Immm spacegroups and has already been shown in this chapter to undergo a second order displacive phase transition.[18] The synthetic aluminosilicate zeolite ferrierite is used in industry as a shape selective catalyst for the production of isobutene, usually at temperatures greater than 100 °C.[8,9] The structures of zeolites are well known to be dependent on their framework and extraframework composition. To further understand the thermal properties of ferrierite and its role as a catalyst, a range of aluminosilicate ferrierite samples have been studied using variable temperature MAS NMR.

Three aluminosilicate ferrierite samples with varying aluminium contents have been studied using both ^{29}Si and ^{27}Al MAS NMR. The silicon to aluminium ratios were 1: 25.5 for low aluminium ferrierite (LAlFER), 1: 12 for medium aluminium ferrierite (MAlFER) and 1: 5.4 for high aluminium ferrierite (HAlFER). The ^{29}Si NMR spectra showed that as the aluminium content increased the resolution of the spectrum decreased. This is thought to be due to broadening of the resonances caused by an increased number of defects within the structure.
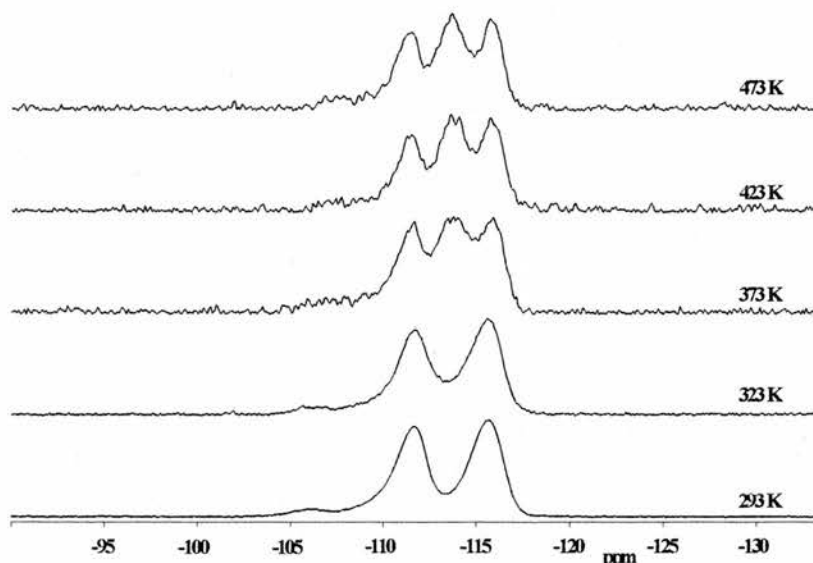

Figure 6.15 Variable temperature ^{29}Si MAS NMR spectra of a low aluminium containing ferrierite sample (LAlFER).

Figure 6.15. shows a collection of five spectra ranging from 293 K to 473 K for the LAlFER sample. The lowest temperature spectrum clearly shows the presence of Al(OSi$_3$) units as a broad peak centred around −105 ppm, and this broad peak does not seem to change as the temperature is increased.[50] The rest of the low temperature spectrum is dominated by two large resonances centred at approximately −111.5 ppm and −116 ppm. These two resonances are believed to be a combination of many

resonances and can be deconvoluted in to a 2: 3 ratio for the –111.5 and –116 ppm

peaks respectively. This compares well to the low temperature spectrum for the

purely siliceous ferrierite sample (10 peaks, split in to two envelopes in a 2: 3 ratio)

and also for the chemical shifts predictions made from the X-ray diffraction data (5

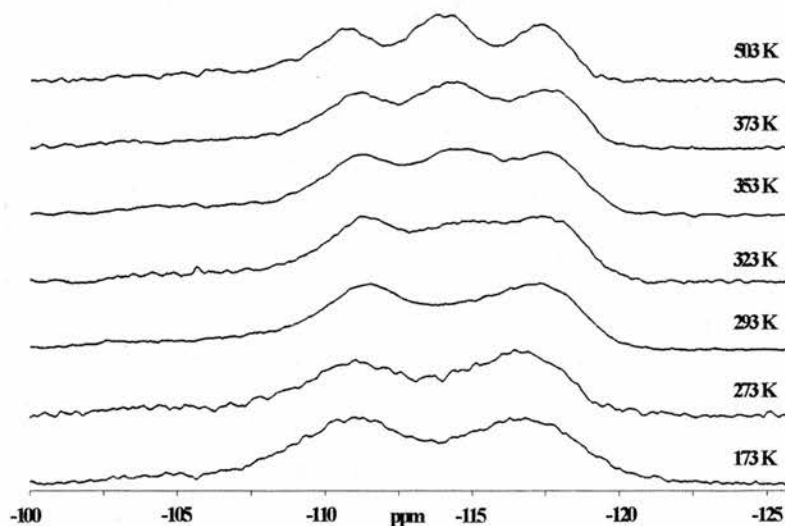peaks, split in to two envelopes in a 2: 3 ratio).

Figure 6.16 Variable temperature ^{29}Si MAS NMR spectra of a moderate aluminium containing ferrierite
sample (MAlFER).

As the temperature is increased to around 370 K a fourth resonance appears centred

at –113 ppm, indicative of a phase transition. This new peak increases slightly in

intensity as the temperature is raised, but its chemical shift does not change indicating

that the appearance of the new peak is not just due to accidental overlap of the

resonances as a function of temperature. Similar trends can be seen for both the

MAlFER and the HAlFER samples as shown in Figures 6.16 and 6.17 respectively,

however, as already mentioned the resolution is much poorer. Both of the samples

also have a broad peak at around –105 ppm corresponding to the $Al(OSi_3)$ units. The

relative intensity of the $Al(OSi_3)$ peak, compared to the intensity of the SiO_4 peak, in

all three of the [29]Si spectra shows that the actual quantity of aluminium incorporated in to the samples is significantly lower than the initial quantities included in the synthesis mixtures. The chemical shift of the $Al(OSi_3)$ peak did not change with increasing temperature in any of the three of the aluminium ferrierite samples, either indicating that the aluminium atoms are located in positions that are not greatly affected by the phase transition or that the peak is so broad that any movement is unnoticeable. The use of ^{27}Al MAS NMR to try to resolve this question was not very successful. The behaviour of the two peaks seen in the [27]Al spectra for all three of the samples was the same. Increasing the temperature revealed no peak movement and the only effect seen was that the broadening increased significantly at high temperatures, this can be seen for the MAlFER sample in Figure 6.18. The temperature at which the broadening becomes significant shows no correlation with the temperature of the phase transition, as determined by ^{29}Si MAS NMR.
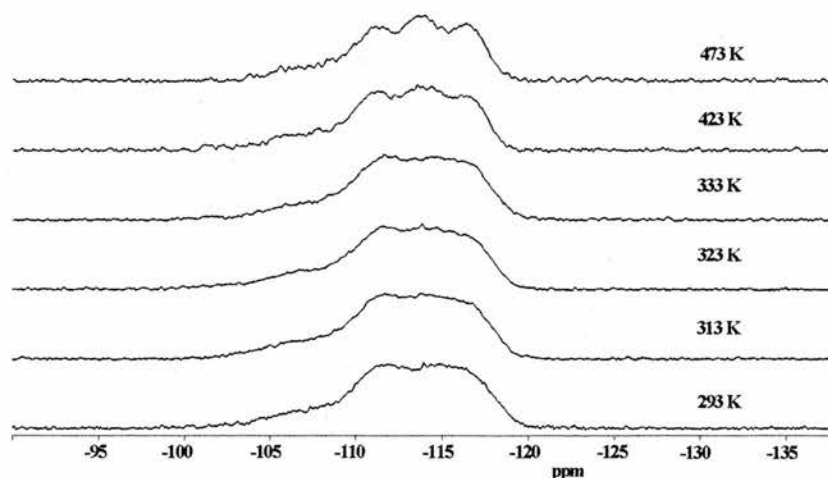

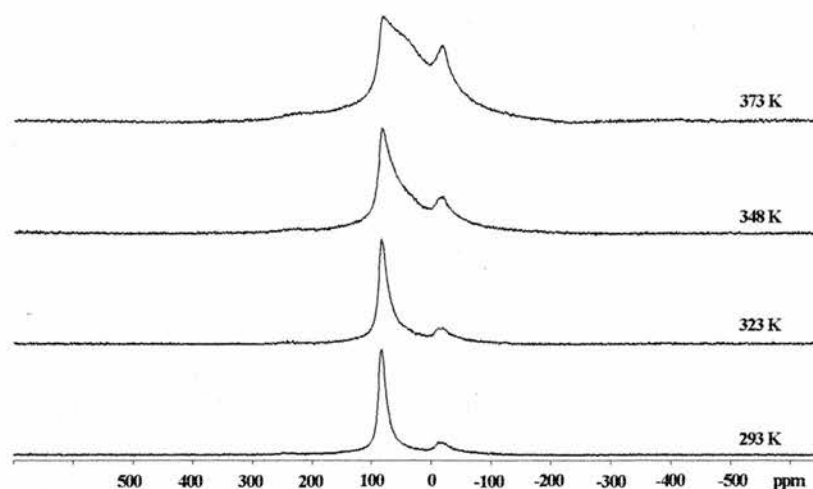Figure 6.17 Variable temperature ^{29}Si MAS NMR spectra of a high aluminium containing ferrierite sample (HAlFER).

Figure 6.18 Variable temperature ^{27}Al MAS NMR spectra for MAlFER

The temperature at which the phase transition is believed to occur for each of these three samples is shown in Table 6.3. It can clearly be seen that as the aluminium content of the ferrierite sample increases the temperature at which the phase transition occurs decreases. This is in good agreement with ^{29}Si MAS NMR studies on the zeolites ZSM-5[51] and ZSM-11[52] by Fyfe *et al.*, and also from X-ray diffraction data for ZSM-5 by Hay *et al.*[53,54] These two methods have shown that increasing both the aluminium content and the quantity of organic sorbate molecules within the zeolite, lowers the temperature of the phase transition.[55,56] It has been proposed that the effect of framework aluminium and adsorbed organics in silicalite is to symmetrize the system by increasing its total entropy.[19] The overall effect of this is to reduce the temperature at which a lower symmetry phase is transformed to a higher symmetry one. This also seems to be the case for ferrierite and it can be concluded that for even higher aluminium contents, the structures will be in the *Immm* phase at room temperature. This of course has important consequences when using ferrierite as a catalyst, as the actual structure will vary depending on the temperature, aluminium

content and probably the quantity of adsorbed organics. These factors may also explain why the natural zeolite ferrierite has been continuously solved in the I*mmm* spacegroup[2-5] and not P*nnm* or a related spacegroup. The low Si/Al ratio and the presence of adsorbed ions could lower the phase transition temperature of natural ferrierite well below room temperature, leaving the structure to be solved in the higher symmetry spacegroup.

Sample	Si: Al ratio	~ Phase transition temperature (K)
Siliceous ferrierite	>1: 2000	400
LAlFER	1: 25.5	370
MAlFER	1: 12	330
HAlFER	1: 5.4	300

Table 6.3 Variation of the phase transition temperature with Si: Al ratio.

6.3 Conclusions

Subtle variations of the known non-aqueous synthesis method for pure silica ferrierite has led to the preparation of a highly crystalline sample, which has enabled further studies in to the materials thermal behaviour to be undertaken. In particular, the collection of high resolution low temperature spectra has indicated that the real symmetry of ferrierite is actually lower than that proposed from earlier X-ray diffraction and MAS NMR studies.[10,12-14,18] A microcrystal X-ray diffraction study of the ferrierite sample, was in full agreement with previous diffraction experiments and showed no signs for lowering of the symmetry. Non-linear optical measurements may have confirmed the NMR data, however, by generation of a second harmonic signal

indicating a noncentrosymmetric spacegroup such as P*nn*2. This clearly shows that MAS NMR is much more sensitive to subtle structural deviations from high symmetry on a local scale than a conventional X-ray diffraction experiment. The large temperature range of the NMR probe has allowed a full comparison of the ^{29}Si chemical shift data with the predictions made from the Si-O-Si bond angles obtained by Bull *et al.* from X-ray diffraction experiments. The simple correlation between bond angle and chemical shift has been shown to be reasonably good for ferrierite and could probably be improved by further refinement.[27,28] The main cause of difference between the predictions and the actual chemical shifts can be attributed to the averaging effect of X-ray diffraction. The bond angles 'measured' from X-ray diffraction data are not always the real angles but are the average of any disorder in the structure, often leading to incorrect values.[26] The variable temperature NMR data has confirmed that pure silica ferrierite undergoes a displacive phase transition, with a mechanism similar to that reported for cristobalite.[24,42] The high temperature phase of ferrierite is believed to be a dynamic average of low temperature structures and this is indicated by the variation of chemical shift and linewidths with temperature. There is, however, significantly more data available from a variety of techniques to support the hypotheses put forward for cristobalite. This quantity of data is not yet available for ferrierite, or any other pure or high silica zeolites, and so the subtle details of both the phase transition and the structure of the high temperature phase cannot be confirmed until these experiments are carried out.

The same variation of ^{29}Si chemical shift with temperature has been shown to occur for three aluminosilicate ferrierite samples. These were synthesised using the fluoride route and produced samples that were highly crystalline and showed signs of less

defects than a sample produced using hydroxide ions. This is believed to be the first report of the synthesis of aluminosilicate ferrierite samples using fluoride ions as a mineralising agent. The ^{29}Si MAS NMR spectra of these samples show much higher resolution than has been previously seen for other samples of aluminosilicate ferrierite. It is, however, believed that this is mainly due to a much smaller quantity of aluminium being incorporated in to the ferrierite structures than was initially calculated from the synthesis ratios, as indicated by the relative intensities of the $Al(OSi_3)$ and SiO_4 peaks in the ^{29}Si spectra.[10] Variable temperature ^{29}Si NMR shows that all three samples undergo a displacive phase transition, although the transition temperature has been observed to vary with aluminium content.

To determine the real structure of ferrierite will require a more rigorous structural investigation using a combination of techniques. This work should include a new ^{17}O MAS NMR study to confirm the number of crystallographically distinct sites in the low temperature phase of ferrierite and transmission electron microscopy of the high temperature phase to look for the presence or absence of domains.

6.4 References for Chapter 6

1. R. P. D. Graham, *Trans. Royal Soc. Canada*, 1919, **12**, 185.

2. L. W. Staples, *Am. Mineral.*, 1955, **40**, 1095.

3. P. A. Vaughan, *Acta Crystallogr., Sect. A: Found. Crystallogr.*, 1966, **21**, 983.

4. W. S. Wise, W. J. Nokleberg and M. Kokinos, *Am. Mineral.*, 1969, **54**, 887.

5. W. S. Wise and R. W. Tschernich, *Am. Mineral.*, 1976, **61**, 60.

6. R. Gramlich-Meier, V. Gramlich and W. H. Meier, *Am. Mineral.*, 1985, **70**, 619.

7. Y. Yokomori, J. Wachsmuth and K. Nishi, *Microporous Mater.*, 2001, **50**, 137.

8. K. Yamahara, K. Okazaki and K. Kawamura, *Catal. Today*, 1995, **23**, 397.

9. J. Haggin, *Chem. Eng. News*, 1993, **25**, 30.

10. R. E. Morris, S. J. Weigel, N. J. Henson, L. M. Bull, M. T. Janicke, B. F. Chmelka and A. K. Cheetham, *J. Am. Chem. Soc.*, 1994, **116**, 11849.

11. H. Gies and R. P. Gunawardane, *Zeolites*, 1987, **7**, 442.

12. A. S. Kuperman, S. Oliver, G. A. Ozin, J. M. Garces and M. M. Olken, *Nature*, 1993, **365**, 239.

13. J. E. Lewis, C. C. Freyhardt and M. E. Davis, *J. Phys. Chem.*, 1996, **100**, 5039.

14. L. M. Bull, B. Bussemer, T. Anupold, A. Reinhold, A. Samoson, J. Sauer, A. K. Cheetham and R. Dupree, *J. Am. Chem. Soc.*, 2000, **122**, 4948.

15. P. Lightfoot, D. A. Woodcock, M. J. Maple, L. A. Villaescusa and P. A. Wright, *J. Mater. Chem.*, 2001, **11**, 212.

16. D. A. Woodcock, P. Lightfoot, L. A. Villaescusa, M. J. Diaz-Cabanas, M. A. Camblor and D. Engberg, *Chem. Mater.*, 1999, **11**, 2508.

17. D. A. Woodcock, P. Lightfoot, P. A. Wright, L. A. Villaescusa, M. J. Diaz-Cabanas and M. A. Camblor, *J. Mater. Chem.*, 1999, **9**, 349.

18. I. Bull, P. Lightfoot, L. A. Villaescusa, L. M. Bull, R. K. B. Gover, J. S. O. Evans and R. E. Morris, *J. Am. Chem. Soc.*, 2003, **125**, 4342.

19. J. M. Chezeau, L. Delmotte, T. Hasebe and N. B. Chanh, *Zeolites*, 1991, **11**, 729.

20. B. F. Mentzen, J. M. Letoffe and P. Claudy, *Thermochim. Acta*, 1996, **288**, 1.

21. S. H. Park, R. W. G. Kunstleve, H. Graetsch and H. Gies, *Stud. Surf. Sci. Catal.*, 1997, **105**, 1989.

22. M. Hochgrafe, B. Marler, H. Gies, C. A. Fyfe, Y. Feng, H. Grondey and G. T. Kokotailo, *Zeitschrift Fur Kristallographie*, 1996, **211**, 221.

23. B. L. Phillips, *Transformation Processes in Minerals*, 2000, **39**, 203.

24. D. R. Spearing, I. Farnan and J. F. Stebbins, *Phys. Chem. Minerals*, 1992, **19**, 307.

25. S. X. Liu, M. D. Welch and J. Klinowski, *J. Phys. Chem. B*, 1997, **101**, 2811.

26. C. A. Fyfe, D. H. Brouwer, A. R. Lewis, L. A. Villaescusa and R. E. Morris, *J. Am. Chem. Soc.*, 2002, **124**, 7770.

27. C. A. Fyfe, Y. Feng and H. Grondey, *Microporous Mater.*, 1993, **1**, 393.

28. R. Dupree, S. C. Kohn, C. M. B. Henderson and A. M. T. Bell, Nuclear Magnetic Shielding and Molecular Structure, J. A. Tossell, Kluwer Academic, Dordrecht, The Netherlands, 1992, p. p 421.

29. M. M. J. Treacy, J. B. Higgins and R. Vonballmoos, *Zeolites*, 1996, **16**, 327-&.

30. H. Robson, *Verified Syntheses of Zeolitic Materials; 2nd Ed.;* Elsevier, Amsterdam, 2001.

31. H. Koller, R. F. Lobo, S. L. Burkett and M. E. Davis, *J. Phys. Chem.*, 1995, **99**, 12588.

32. A. L. Spek, *PLATON. A Multipurpose Crystallographic Tool*, Utrecht University, Utrecht, The Netherlands , 1999.

33. G. Neue and C. Dybowski, *Solid State Nucl. Magn. Reson.*, 1997, **7**, 333.

34. M. T. Dove, *Am. Mineral.*, 1997, **82**, 213.

35. K. D. Hammonds, M. T. Dove, A. P. Giddy, V. Heine and B. Winkler, *Am. Mineral.*, 1996, **81**, 1057.

36. M. T. Dove, M. Gambhir and V. Heine, *Phys. Chem. Minerals*, 1999, **26**, 344.

37. M. T. Dove, V. Heine and K. D. Hammonds, *Mineral. Mag.*, 1995, **59**, 629.

38. M. T. Dove, K. O. Trachenko, M. G. Tucker and D. A. Keen, *Transformation Processes in Minerals*, 2000, **39**, 1.

39. M. Gambhir, M. T. Dove and V. Heine, *Phys. Chem. Minerals*, 1999, **26**, 484.

40. B. L. Phillips, J. G. Thompson, Y. H. Xiao and R. J. Kirkpatrick, *Phys. Chem. Minerals*, 1993, **20**, 341.

41. P. W. Anderson, *J. Phys. Soc. Jpn.*, 1954, **9**, 316.

42. I. P. Swainson and M. T. Dove, *J. Phys.: Condens. Matter*, 1995, **7**, 1771.

43. I. P. Swainson and M. T. Dove, *Phys. Chem. Minerals*, 1995, **22**, 61.

44.   M. P. Attfield, S. J. Weigel and A. K. Cheetham, *J. Catal.*, 1997, **172**, 274.

45.   R. J. Cernik, W. Clegg, C. R. A. Catlow, G. Bushnell-Wye, J. V. Flaherty, G. N. Greaves, I. Burrows, D. J. Taylor, S. J. Teat and M. Hamichi, *J. Synchrotron Rad.*, 1997, **4**, 279.

46.   G. M. Sheldrick, *Programs for Crystal Structure Analysis. Release 97-2*, 1997.

47.   Siemens, *SHELXTL. Structure Determination Software*, Siemens Analytical X-ray Instruments Inc., Madison, Wisconsin, USA, 1995.

48.   L. J. Farrugia, *J. Appl. Crystallogr.*, 1999, **32**, 837.

49.   C. A. Fyfe, D. H. Brouwer, A. R. Lewis and J. M. Chezeau, *J. Am. Chem. Soc.*, 2001, **123**, 6882.

50.   J. Klinowski, *Chem. Rev.*, 1991, **91**, 1459.

51.   C. A. Fyfe, G. J. Kennedy, G. T. Kokotailo, J. R. Lyerla and W. W. Fleming, *Chem. Comm.*, 1985, 740.

52.   C. A. Fyfe, Y. Feng, H. Grondey, G. T. Kokotailo and A. Mar, *J. Phys. Chem.*, 1991, **95**, 3747.

53.   D. G. Hay, H. Jaeger and G. W. West, *J. Phys. Chem.*, 1985, **89**, 1070.

54.   D. G. Hay and H. Jaeger, *Chem. Comm.*, 1984, 1433.

55.   C. A. Fyfe, H. Strobl, G. T. Kokotailo, G. J. Kennedy and G. E. Barlow, *J. Am. Chem. Soc.*, 1988, **110**, 3373.

56.   J. Klinowski, T. A. Carpenter and L. F. Gladden, *Zeolites*, 1987, **7**, 73.

7.0 Conclusions and Further Work

7.1 Overall Conclusions

The combination of solid state NMR and microcrystal X-ray diffraction has enabled the structures of several pure and high silica zeolites to be determined. Although many of the structures of these zeolites have been determined before, these initial solutions have been shown to be incorrect, by the use of one or both of these powerful techniques. The ability to study both the local structure, with NMR, and the space averaged structure, with XRD, has provided a great deal of information on the fluoride location in SSZ-44 and the thermal behaviour of ferrierite.

The synthesis of an isotopically labelled sample of [tPABr,F]-MFI has provided an excellent test material for determining a zeolite structure using MAS NMR. Although initial attempts to measure the ^{19}F/^{15}N and the ^{15}N/^{29}Si dipolar couplings have been unsuccessful, it is still believed that the concept proposed will work and attempts to prove this are still under way.

Throughout the course of this work there have been many ideas, that for one reason or another, could not be attempted. A few of these are listed below as suggestions for future work in the area of structural determination of zeolites.

7.2 Further Work

The synthesis of an improved non-linear optical zeolite material should definitely be retried using ortho substituted benzylquinuclidines, and not the para functionalised ones as attempted during this work. These syntheses should be performed using both fluoride and hydroxide ions as the mineralising agent, in order to investigate further the mechanisms of template alignment in noncentrosymmetric zeolites.

In light of the results, on the thermal behaviour of ferrierite, it is suggested that the effect of organic guest molecules, such as isobutene, on the phase transition temperature should be investigated by ^{29}Si MAS NMR. This work should be combined with a high resolution ^{17}O NMR study of the low temperature phase of siliceous ferrierite, in order to help determine the precise crystal symmetry. It would also be interesting to study the natural form of ferrierite, in order to determine both the crystal symmetry and to see if the mineral undergoes a phase transition. Further work on ferrierite could also include a transmission electron microscopy study of both the low and high temperature phases, in order to confirm the proposed mechanism of the phase transition.